國立臺灣大學工學院土木工程學系

博士論文

Department of Civil Engineering
College of Engineering
National Taiwan University

Doctoral Dissertation

沖積扇之計算與實驗形貌動力學研究

Computational and Experimental Morphodynamics of Aggrading Fans

陳慈愔
Tzu-Yin Chen

指導教授：卡艾瑋 博士
Advisor: Hervé Capart, Ph.D.

中華民國 111 年 9 月
September, 2022

doi:10.6342/NTU202204140

摘要

沖積扇是地質學家和工程師感興趣的高地和低地過渡地帶常見的地貌。沖積扇可容納來自陡坡集水區的材料，並提供適宜居住的緩坡空間。然而，由於洪水或土石流引起的沖積扇演變也對沖積扇上或周圍的居民和基礎設施構成嚴重風險。 爲了研究沖積扇的堆積行爲和相關風險，本論文結合計算模擬和實驗及現地觀察。本論文提出了兩種計算模型，並根據實驗室實驗和現場數據評估它們的性能。第一個計算模型模擬受地形控制的靜態沖積扇形貌。該模型將三維形貌問題轉化爲一系列二維可視多邊形問題，由此藉由計算幾何學之工具進行計算模擬。而第二個計算模型模擬了沖積扇的動態堆積過程。該模型假設沖積扇局部之坡度受材料性質(摩擦角與凝聚性)限制，以此模擬出在實驗室與現地共同可觀察到的沖積扇特徵，如陡峭的鼻狀扇趾。這兩種模型都有其廣泛的應用，儘管它們被簡化並且無法描述沖積扇表面的一些詳細動態特徵。爲了研究這兩個模型中未包含的形貌動力特徵及其影響因素，本論文在實驗室進行了一系列持續土石流沖積扇實驗。我們將實驗結果與現地觀察的沖積扇資料一同分析討論，發現細顆粒含量和流動事件時間尺度會影響渠道化、撕脫動力學以及隨之而來的扇面複雜性。本論文的結果表明，沖積扇形態可以在不同的尺度上考慮：在較廣的尺度上，沖積扇可以通過旋轉表面進行模擬；在較近的尺度上，沖積扇表現出局部結構特徵，如鼻狀扇趾和土石流渠道。前者的形成可以通過材料之凝聚性進行模擬，後者的形成、大小和撕脫動力學與土石流之材料組成和流動時間尺度有關。論文提出的結果和方法適用於沖積扇演化預測、地形資料判釋、災害評估以及其他地景地貌的探討和研究。

關鍵字: 沖積扇形貌; 旋轉面； 計算形態動力學； 土石流； 組成律

doi:10.6342/NTU202204140

Abstract

Alluvial fans are common and often dense-populated landforms in the transitions of high and low lands. The evolution of alluvial fans due to floods or debris flows poses severe risks to residents and infrastructure on or around the fans. To assess and mitigate the hazards, it's important to have a better understanding of fan morphology and morphodynamics. The present thesis combines computations and observations to investigate how material properties affect the morphology of aggrading fans. On one hand, I propose hypothetical influencing material properties and develop two computational models to realize and examine them. On the other hand, I conduct a series of alluvial fan experiments and compare the results with field observations to generalize some process characteristics of fan morphodynamics. The results of this thesis implicate that alluvial fan morphologies can be considered on various scales: on a broader scale, alluvial fans can be simply modeled by surfaces of revolution; on a closer scale, alluvial fans exhibit local structure features, like snout-like toes, whose formation may be modeled by the cohesion effects in the flows, and channels, whose formation, size, and avulsion dynamics relate to flow composition and time scales. The results and methods proposed in the thesis are applicable to the alluvial fan evolution prediction, topography data interpretation, hazard assessments, and also the exploration and investigation of other geometric landscapes.

Keywords: *Alluvial fans; morphology; surface of revolution; computational morphodynamics; debris flows; granular-fluid flows; constitutive laws*

doi:10.6342/NTU202204140

Contents

doi:10.6342/NTU202204140

doi:10.6342/NTU202204140

doi:10.6342/NTU202204140

List of Figures

doi:10.6342/NTU202204140

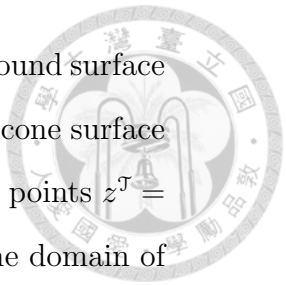

doi:10.6342/NTU202204140

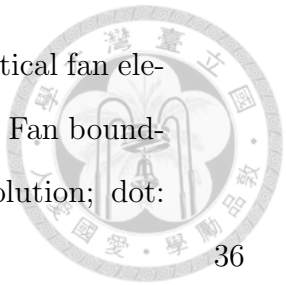

doi:10.6342/NTU202204140

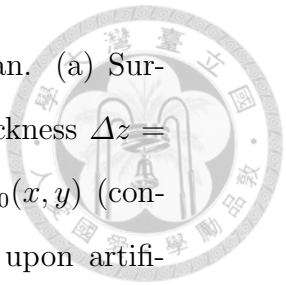

doi:10.6342/NTU202204140

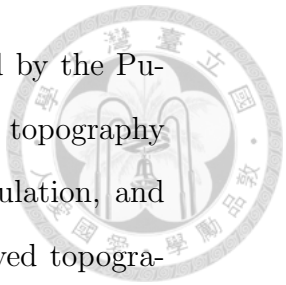

doi:10.6342/NTU202204140

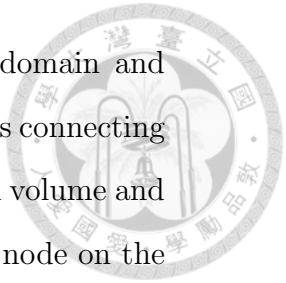

doi:10.6342/NTU202204140

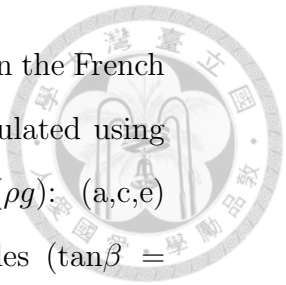

doi:10.6342/NTU202204140

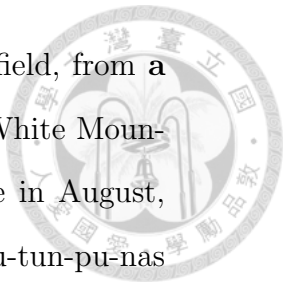

doi:10.6342/NTU202204140

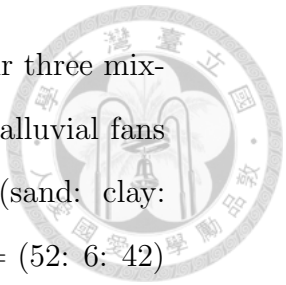

doi:10.6342/NTU202204140

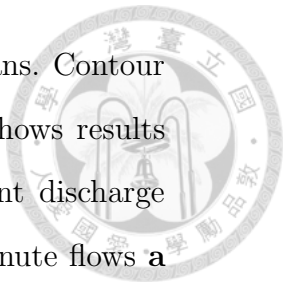

doi:10.6342/NTU202204140

List of Tables

doi:10.6342/NTU202204140

List of Algorithms

doi:10.6342/NTU202204140

Chapter 1

Introduction

1.1 Alluvial fans and related hazards

Alluvial fans are common landform in mountainous areas around the world (Drew, 1873; Kochel and Johnson, 1984; Harvey, 2002; Hsieh and Capart, 2013; de Haas et al., 2015b; Tomczyk, 2021). They accommodate the materials (soil and sediments) in the regions with sudden slope changes, such as foothills (de Haas, 2016) or tributary-trunk-river junctions(Gómez-Villar et al., 2006; Al-Farraj and Harvey, 2005; Stokes and Mather, 2015; Leenman and Tunnicliffe, 2020). They typically featured intermediate slopes (see Fig. 1.1 for example) between the steep slopes of the catchment areas and the mild slopes of the open areas, like basins, plains, and trunk rivers valleys.

The intermediate slopes of the alluvial fans make them great habitats for humanity. However, the events that form and evolve the alluvial fans, such as floods and debris flows, also pose significant threats to the inhabitant and infrastructures on the fan surfaces. The aggradation and expansion of the alluvial fans also threaten infrastructure in mild basins or valleys, such as roads, flood protectors, pipe networks, etc, and consequently the connection to crucial services, such as education, health care, and emergent treatment, to residents in mountainous areas. The severity of the threats even continuously grows with the increasing landscape exploitation and climate changes, such as extreme storms and frequent wildfires (DeGraff and Ochiai, 2009; Keiler et al., 2010).

For example, the tributary-junction fans along the Laonong River, southwest Taiwan (Fig. 1.1) aggraded and expanded significantly with strong episodes of debris flows and buried the highway along the Laonong River and formed dammed

doi:10.6342/NTU202204140

Figure 1.1: The Putunpunas debris flow fan along the Laonong River, Southwestern Taiwan.

lakes several times in recent years (Capart et al., 2010; Lo et al., 2018; Yang et al., 2022).

1.2 Alluvial fan morphologies

In this thesis, we focus on alluvial fans formed by fluvial or debris flow dominated processes. These alluvial fans typically have areas range in 0.02-100 km^2 and slopes range in 0.05-0.35 m/m (Chang et al., 1995; de Haas, 2016). They typically have conical shapes featured with convex transverse profiles and straight to concave longitudinal profiles (de Haas, 2016; de Haas et al., 2018; Williams et al., 2006). However, they may also exhibit complex shapes when interacting with irregular terrains or encountering episodes of incisions (e.g. Fig. 1.1). Besides, some debris flow fans may have steep snouts along the fan toes and therefore have convex or S-shaped longitudinal profiles (Coussot et al., 1996).

doi:10.6342/NTU202204140

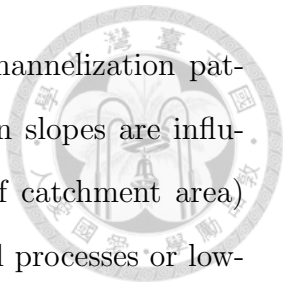

The morphologies of alluvial fans, like average slopes and channelization patterns, are influenced by many various factors. Mean average fan slopes are influenced by Melton's number (catchment relief over square root of catchment area) (Melton, 1965) and flow compositions. Fans dominated by fluvial processes or low-sediment-concentration debris flows tend to have smoother surfaces Whipple and Dunne (1992); Blair (1999). On the contrary, fans dominated by high-sediment-concentration debris flows may have many active and inactive channels on the fan surfaces, causing the bumpiness of the surfaces. The inactive channels are left on fan surfaces due to changes in channel directions, called "avulsions". In addition to causing bumpiness of fan surfaces, avulsion sequences may also lead to the varying of slope in different azimuthal directions in short term while these variations tend to compensate over several events (de Haas et al., 2018; Densmore et al., 2019). The occurrence frequency of avulsions may vary dramatically (Dühnforth et al., 2007). Beaty (1963) suggested that the existence of large boulders, which are related to catchment lithology, in the flows can cause additional sudden avulsions. de Haas et al. (2018) suggested that magnitude-frequency distribution of debris flows and the sequence of the flows entering fans also influence avulsions.

1.3 Landform monitoring and data interpretation

Monitoring the evolution of alluvial fans provides evidence for studying the factors that influence the morphology and morphodynamics of the alluvial fans. Besides, that can also help to investigate the history of trunk river valleys (see Hsieh and Chyi (2010); Hsieh and Capart (2013) and Chen et al. (2022)). In recent years, advances in field survey techniques have made it possible to monitor the evolution of landforms like alluvial fans at increasing spatial resolution and temporal frequency. These techniques include expensive approaches, like airborne Lidar, but also very affordable ones like airborne photogrammetry using Unmanned Aerial Vehicles (UAVs). Using the techniques, we have been able to acquire detailed repeat

doi:10.6342/NTU202204140

measurements of active landforms. To interpret these data and produce forecasts of future evolution, however, new modeling tools are needed that can take into account the complex boundary conditions associated with actual field sites.

1.4 Alluvial fan modeling

Currently, most computational models simulate alluvial fan morphologies by simulating the time-resolved flow and deposition of the flows with mass and momentum balance equations to flows over non-erodible (O'Brien et al., 1993; O'Brien, 2006; Liu and Huang, 2006; Murillo and García-Navarro, 2012; Pudasaini, 2012; Kowalski and McElwaine, 2013; Gregoretti et al., 2016; Meng and Wang, 2016; Tai et al., 2019; Pudasaini and Fischer, 2020) or erodible substrates (Armanini et al., 2009; Bartelt et al., 2017). However, it is desirable to model fan evolution over extended time scales to investigate past fan evolution and mitigate risks of natural hazards on the fan surfaces. For this purpose, the methods designed for simulations of single debris flow surges or flood events are too computationally expensive. They also typically require more detailed rheological information and influx histories than are typically available.

1.5 General objectives and specific aims

This thesis aims to combine computations and observations to investigate and improve understanding of the aggradation behavior of alluvial fans and associated risks. In general, the thesis has two main objectives:

1. To provide useful and efficient tools to model alluvial fan morphology and morphodynamics and assess associated risks.

2. To investigate features and influence factors of alluvial fan morphology and morphodynamics.

doi:10.6342/NTU202204140

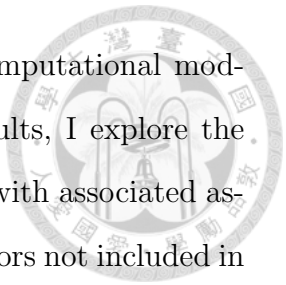

The thesis aims to develop novel geomorphic constrained computational models to achieve the first objective. Building on the modeling results, I explore the morphology features of alluvial fans on various irregular terrains with associated assumptions. To compare and investigate potentially influential factors not included in the computational models, I conduct experiments with variable flow compositions and compare experimental results to field observations. The thesis combines the computations and observations in two folds: (1) exploit the model results to help the quantitative analysis of the observation; and (2) use the experimental and field observations to evaluate the limitation of the computational models and identify paths for future improvements.

I subdivide the thesis objectives into the following specific aims:

1. To reconstruct past alluvial fan morphology and predict alluvial fan morphology and assess associated hazards on a long time scale.

2. To predict the qausi-static evolution of fan morphology including local snout-like features.

3. To investigate the influences of flow composition and time scale on the fan morphology and channelization.

To approach these aims, four types of alluvial fans are considered in this thesis as demonstrated in Fig. 1.2. Their geometry features, physical processes, material properties, and associated references are summarized in Table 1.1.

In Chapter 2, I consider fans whose elevation and slope are assumed to depend only on the distance from the apex, measured along straight (constant-slope fans, Fig 1.2a) or winding paths (concave fans, Fig 1.2b). Based on this assumption, I can reduce the three-dimensional fan morphology problem to a sequence of two-dimensional visibility polygon problems, which can be solved by standard tools of computational geometry. The resulting model can therefore be highly efficient,

doi:10.6342/NTU202204140

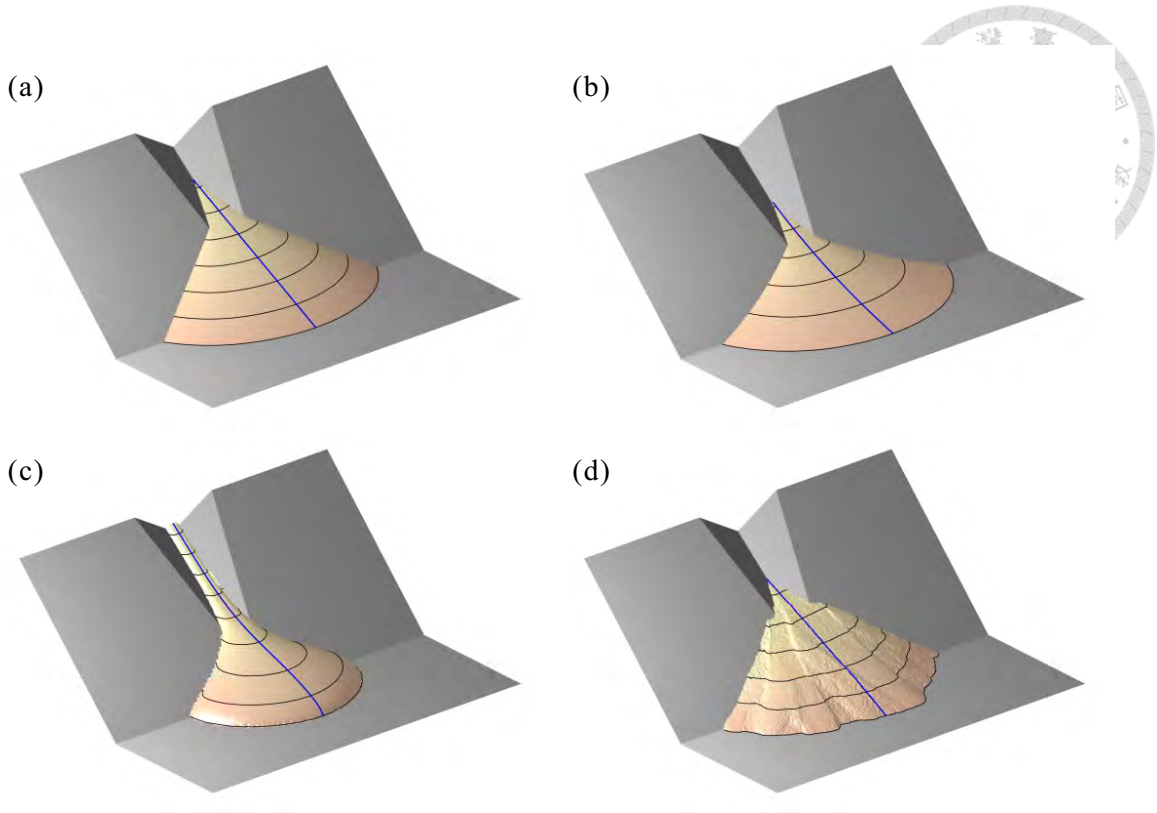

Figure 1.2: Types of alluvial fans discussed in this thesis. (a) Constant slope fan; (b) concave fan with a decreasing slope; (c) fan with steep snout-like toe; (d) fan with channels and lobes.

Table 1.1: Geometry features, physical processes, material properties, and associated references of the four types of alluvial fans discussed in this thesis.

Fan type	Constant slope fans	Concave fans	Fans with steep snout-like toes	Fans with channels and lobes
Elevation contours	equally spaced	spaces increase downfan	dense along the toes	irregular
Longitudinal profiles	straight	concave up	convex along the toes	irregular
Dominated physical processes or material properties	debris or bedload-transporting flows with equilibrium inclination	reduced sediment load and grain size fining	slope dominated by yield stress or cohesion and deposit thickness	channelization and avulsion
Associated references	Takahashi (1991), Whipple et al. (1998), Armanini et al. (2005), Williams et al. (2006), de Haas (2016)	Parker et al. (1998), Blissenbach (1952), Hooke (1968), Parker et al. (1998), Williams et al. (2006), Stock et al. (2008), de Haas (2016)	Coussot et al. (1996), Yuhi and Mei (2004), Li (2015)	Beaty (1963), Drew (1873), Whipple and Dunne (1992), Blair (1999), de Haas (2016), de Haas et al. (2018), Dühnforth et al. (2007)

doi:10.6342/NTU202204140

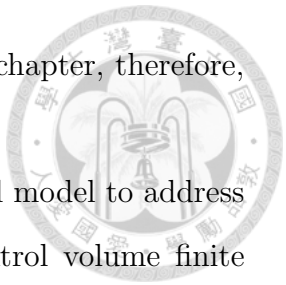

accurate, and robust for simulating static fan morphology. This chapter, therefore, addresses the first aim of the thesis.

In Chapter 3, I develop a pseudo-time-evolving computational model to address the second aim of the theses. The model is based on the control volume finite element method which can accommodate fans restricted to local slope assumptions, including constant-slope fans (Fig 1.2a) and fans with steep snout-like toes (Fig 1.2c).

In Chapter 4, I combine field and experiment studies with exploring the fans with channels and lobes (Fig 1.2d), which is beyond the range of the two models in previous chapters. For the field, I analyze data from two neighboring alluvial fans that exhibit dramatically different topographies features. For experiments, I conduct a series of laboratory experiments with systematically changed flow compositions and flow time scales. I compare the experimental results to field cases using the same quantitative analyzing method to study the effects of fine particle content and time scales on fan morphology and channelization/avulsion patterns.

Finally, in chapter 5, I conclude the thesis by comparing the findings in computational, experimental, and field works. Based on the observations from experiments and the field, I evaluate the advantage and disadvantages of the computational models and propose potential paths for future improvements.

doi:10.6342/NTU202204140

Chapter 2

Computational morphology of debris and alluvial fans on irregular terrain using the visibility polygon

A computational method is proposed to simulate the morphology of debris and alluvial fans formed on irregular terrain, where they may abut or bend around steeper valley sides or obstacles. Fan elevation and slope are assumed to depend only on the distance from the apex, measured along straight or winding paths. When there are no obstacles, the resulting fan morphologies are simply surfaces of revolution, with a straight (for constant slope fans) or curved generatrix (for concave fans). When obstacles are present, however, fan surfaces of great variety can be produced. To capture the resulting morphology, we exploit a powerful tool of computational geometry: the visibility polygon algorithm. Starting from one or more initial fan apexes, the proposed algorithm iteratively generates fan sectors with new apexes along their margins, until the fan complex has attained its maximal extent. To validate the method, we first apply it to several cases with analytical solutions, such as single fans on faceted topography, and multiple coalescing fans with weld lines. We then apply the method to real valleys, and check that it can reproduce observed fan morphologies even in complex cases involving diffluences and confluences.

Published as: Chen, T. Y. K., and Capart, H. (2022). Computational morphology of debris and alluvial fans on irregular terrain using the visibility polygon *Computers and Geosciences*, 105228. DOI:10.1016/j.cageo.2022.105228.

doi:10.6342/NTU202204140

2.1 Introduction

In mountainous areas, debris flows or torrential floods can dramatically alter the landscape by delivering large amounts of rocks and sediment from steep catchments down to areas of milder slope, where their deposits accumulate to form debris or alluvial fans. Such fans are of interest to quaternary geologists as records of past valley evolution (Hsieh and Chyi, 2010). They also matter greatly to civil engineers, due to the significant threats they pose to people and infrastructure (Keiler et al., 2010). To investigate past fan evolution and mitigate long term risk, it is therefore desirable to model fan evolution over extended time scales. For this purpose, the methods designed for time-resolved simulations of single debris flow surges or flood events (Murillo and García-Navarro, 2012; Tai et al., 2019) are too computationally expensive. They also typically require more detailed rheological information and influx histories than are typically available.

In the present work, we therefore adopt a simplified model of fan morphology, whereby the surface inclination is either assumed constant or taken to decrease with elevation according to a known function. This assumption is motivated both by mechanics and by observations. By mechanics, assuming a given ratio of water flux to granular transport rate, bed deposits underneath debris or bedload-transporting flows tend to adopt a particular equilibrium inclination (Takahashi, 1991; Armanini et al., 2005), which is supported by observations of debris and alluvial fans in the laboratory (Takahashi, 1991; Whipple et al., 1998). For large scale fluvial systems, the equilibrium inclination decreases downslope due to reduced sediment load (Drew, 1873; Parker et al., 1998) and grain size fining (Blissenbach, 1952; Hooke, 1968; Parker et al., 1998; Stock et al., 2008). The constant slope assumption has been used previously to model the shape of sand heaps in the presence of obstacles (Ahmed et al., 2004; Kuster and Gremaud, 2006), or over irregularly-shaped or vibrating base plates (Pauli and Gioia, 2007; van Gerner et al., 2015). It has also been adopted

doi:10.6342/NTU202204140

to model the prograding fronts of sedimentary deltas (Ke and Capart, 2015; Zhao et al., 2019). The decreasing slope assumption, likewise, has been used previously to model fluvial fans and deltas (Parker et al., 1998).

Different factors may influence the slopes of individual fans. For instance, fan inclination increases with the ratio of sediment supply to water discharge (Whipple et al., 1998), and decreases with the area of the contributing basin (Lin et al., 2009). In the field, alluvial fans are commonly characterized by concave longitudinal profiles (Drew, 1873; Denny, 1965; Williams et al., 2006; Stock et al., 2008; de Haas et al., 2015b). Among them, debris flow dominated fans tend to have smaller concavity than fluvial dominated fans. For the debris flow fans investigated by Staley et al. (2006), fan inclination was found to generally decrease downslope. Whereas such decreases were sharp in the upper and lower zones, they were much less pronounced in mid sections of the fan surfaces. Likewise, the debris fans examined by Williams et al. (2006); de Haas et al. (2015b) were found to have nearly linear profiles. Thus the slopes of many debris fans can be approximated as constant, at least in first approximation (Lin et al., 2009; Williams et al., 2006). For fluvial dominated fans, by contrast, the surface gradient typically varies significantly downslope, hence the decreasing slope assumption will be more appropriate.

On the surface of real fans, particularly at finer scales, flow paths may be curved or jagged, and may follow existing channels or avulse to new channels (Beaty, 1963; Hubert and Filipov, 1989; Whipple and Dunne, 1992; de Haas, 2016; de Haas et al., 2018; Leenman and Eaton, 2021). Downslope changes in elevation and slope may also vary in different azimuthal directions (Hooke and Rohrer, 1977; de Haas et al., 2018), but these variations tend to compensate over several events (de Haas et al., 2018; Densmore et al., 2019). Here, we neglect such local and azimuthal variations and assume that fans are formed from surfaces of revolution (Krivoshapko and Ivanov, 2015), for which the inclination is either constant or dependent only on elevation relative to the fan apex. In plan and absent any obstacle, the resulting

doi:10.6342/NTU202204140

paths of steepest descent will necessarily be straight lines, or rays (Kevorkian, 1990). When obstacles are present, however, the distance along which elevation and slope vary must be measured along winding paths.

The resulting surfaces may then be as simple as a truncated cone, but may also exhibit complex shapes when fan inclination varies, when multiple fans interact, or when obstacles are present. When the fan slope is constant, they belong to the broad class of developable surfaces (Pottmann and Wallner, 2001). Locally, neighboring rays generate ruled surface patches that are either sectors of upright cones, or tangent surfaces to curves of constant inclination (Pottmann and Wallner, 2001). These patches can connect with each other or with the constraining topography in two different ways. They may either connect tangentially, along rays, or intersect along creases (Pauli and Gioia, 2007; Ke and Capart, 2015; Jiang et al., 2019). When they are constrained by irregular topography, or produced from multiple apexes, the resulting fans may therefore adopt quite complicated morphologies.

To model the resulting surfaces, we propose in this chapter a new computational method based on a widely used tool of computational geometry: the visibility polygon. In two dimensions, the visibility polygon delineates the sub-domain that is visible from a given vantage point inside or along the boundary of an arbitrary polygonal region, possibly multi-connected (Lee, 1983; Asano, 1985; Ghosh, 2007). The shortest path from the vantage point to any point within the visibility polygon is therefore a straight line. Starting from new vantage points at any occluding corners that may occur along the boundary of a visibility polygon, the algorithm can then be applied iteratively. This makes it possible to determine the shortest path to any destination within the original region, avoiding obstacles along the way (Lee and Preparata, 1984; Asano et al., 1986).

For application to debris and alluvial fans, here we generalize this method to three dimensions, by considering surfaces of revolution intersecting a given terrain topography. A visibility polygon algorithm is then used to reduce the resulting

doi:10.6342/NTU202204140

region to only the sector that can be reached from the apex without encountering any obstacle. Starting from one or more initial fan apexes, the proposed method iteratively generates fan sectors with new apexes along their margins, until the fan complex has attained it maximal extent.

The chapter is organized as follows. In section 2, we describe the basis of the approach and the algorithms used for each step. In section 3, we validate the method on several cases with analytical solutions, such as fans on faceted and curved topographies and multiple interacting fans with weld lines. In section 4, we then test the approach using real topography data, and check that the model can reproduce observed fan morphologies. In Section 5, we discuss some implementation and performance issues. Finally conclusions and perspectives are proposed in section 6.

2.2 Methodology

2.2.1 Two-dimensional fan morphology algorithm

Depending on the assumption chosen, constant or decreasing slope, we first define an unobstructed fan surface of apex A, as illustrated in Fig. 2.1. For fans of constant slope (Fig. 2.1a), we consider a conical surface S having its apex at point A. The resulting elevation Z_{AP} at point P will therefore be given by

$$Z_{AP} = Z_A - H_{AP} = Z_A - S\|\vec{P} - \vec{A}\|, \tag{2.1}$$

where Z_A is the apex elevation, $H_{AP} = Z_A - Z_P$ is the height difference, and $\|\vec{P} - \vec{A}\|$ is the horizontal distance from the apex. For decreasing slope (Fig. 2.1b), we consider a more general surface of revolution (Krivoshapko and Ivanov, 2015), with a generatrix that decreases in slope as the elevation drops relative to the apex, or equivalently as the distance from the apex increases. For this dependence on distance, we adopt a negative exponential function, widely used to describe alluvial fans in the field (Moore and Howard, 2005; Williams et al., 2006; Kraal et al., 2008;

doi:10.6342/NTU202204140

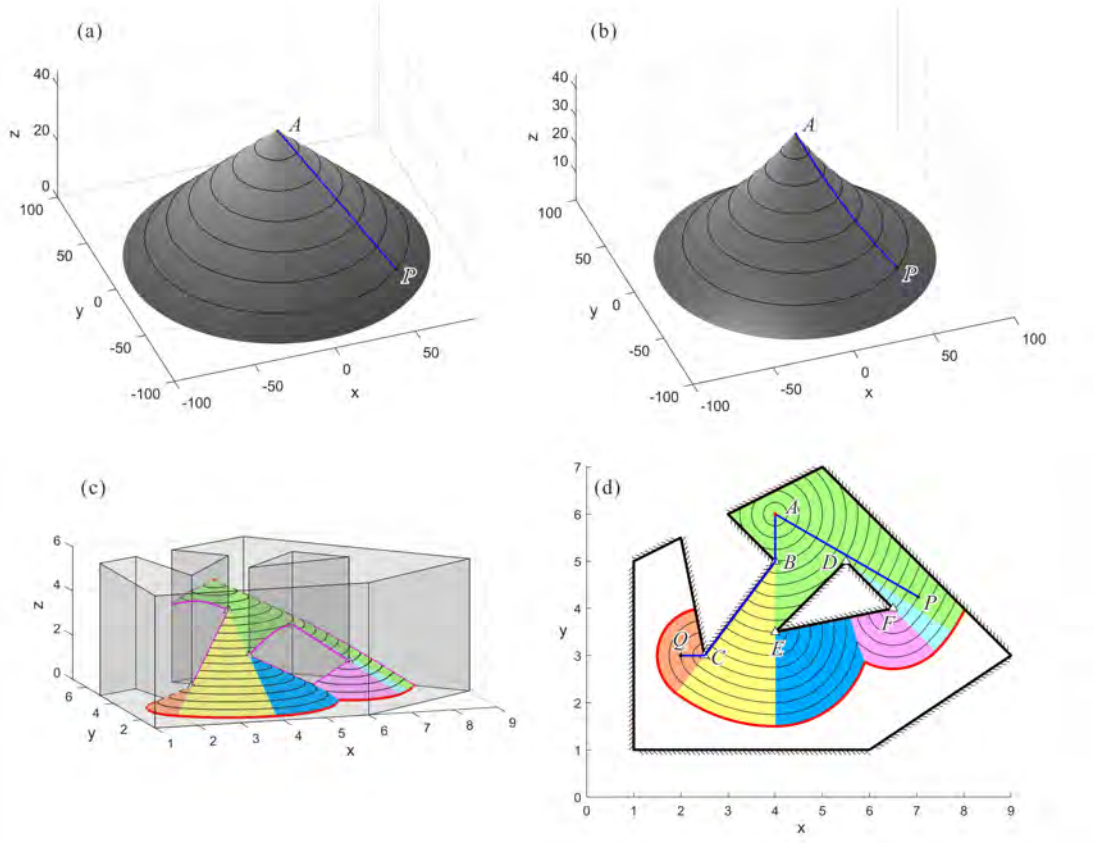

Figure 2.1: Idealized models of fan morphology. (a) Constant-slope cone; (b) concave surface of revolution; (c,d) constant-slope fan complex in a prismatic domain bounded by vertical walls and internal obstacles: (c) oblique view. (d) top view. Red point: initial fan apex; triangles: corner apexes; thin black lines: elevation contours; gray face/bold black line: boundary polygon; red line: fan toe; pink line: fan margin; colored polygons: visible sectors; blue lines: shortest paths from origin to destinations (black dots). Point Q is visible to apex C but invisible to apexes A and B. Point P is visible to apexes A, D, and F.

doi:10.6342/NTU202204140

Morgan et al., 2022). This can be written

$$Z_{AP} = Z_A - H_{AP} = Z_A - \frac{S_A}{K}\left(1 - \exp\left(-K\|\vec{P} - \vec{A}\|\right)\right), \tag{2.2}$$

where S_A is the surface slope at apex A, and K is the concavity. The surface inclination decreases linearly with the height difference H_{AP}. If desired, other functional forms could also be chosen. It can be seen that both the constant slope surface (Fig. 2.1a) and the concave surface (Fig. 2.1b) are azimuthally symmetric with respect to a vertical axis through the apex. Viewed from the top (in $x-y$ plan), all elevation contours will therefore be concentric and the path of steepest descent from the apex A to point P will be a straight line (blue line in 2.1a,b), called the eikonal ray (Kevorkian, 1990), perpendicular to the contours. The difference is that, in profile, the steepest descent path is also a straight line for the constant slope fan, but becomes a planar curve for the concave fan. These paths also coincide with the generatrix, straight or curved, of the corresponding surfaces of revolution (Krivoshapko and Ivanov, 2015).

In Fig. 2.1c,d, we consider a conical fan depositing over horizontal ground in a region confined by vertical walls. For this geometry, the three-dimensional problem (panel c) reduces to two dimensions when viewed from the top (panel d). In plan, the topographic contours (lines of equal elevation z) are analogous to wave fronts (lines of equal arrival time T) propagating outward from a source at point A. We can use Eq. (2.1) or (2.2) to calculate the elevation of P if and only if, in plan, A and P can be connected by a straight line without passing through any obstacle or boundary, namely A and P are *visible* to each other. The fan surface visible from apex A can be referred to as the *visible sector* of A.

In contrast, if a point Q is invisible to apex A, the shortest path to Q must consist of several straight-line segments that wind around the obstacles, where each *corner* of the path forms a new fan apex. Each new fan apex (child apex) is located at the boundary between the visible and invisible regions of its parent apex. The

doi:10.6342/NTU202204140

set of destinations reached via a given apex sequence is a visible sector, shown as a colored region in Fig. 2.1d. For instance point Q is in sector ABC ($Q \in ABC$). Q must be visible to the youngest apex C, and the elevation of Q can be calculated as the elevation at Q of an upright cone with apex C. For constant slope fans,

$$Z_{CQ} = Z_A - H_{AB} - H_{BC} - S\|\vec{Q} - \vec{C}\|. \tag{2.3}$$

For concave fans,

$$Z_{CQ} = Z_A - H_{AB} - H_{BC} - \frac{S_C}{K}\left(1 - \exp\Big(-K\|\vec{Q} - \vec{C}\|\Big)\right), \tag{2.4}$$

where $S_C = S_A - K(z_A - z_C)$. A point may be visible to multiple cone apexes. For instance, point P in Fig. 2.1c,d is visible to apexes A, D, and F. Since a higher cone will deposit over a lower one, the fan elevation must then be the highest elevation associated with all visible apexes. For point P, for example,

$$Z_P = \max(Z_{AP}, Z_{DP}, Z_{FP}). \tag{2.5}$$

We can therefore construct the fan morphology iteratively as follows: First, find the sector visible from any new apex, and update the fan elevation in this sector if its cone elevation is higher than the current elevation. Second, find child apexes, associated with any corners lying along the edges between visible and invisible areas, and determine their elevations. The two steps can then be repeated until no new child apex is born.

In the above procedure, the critical step is the determination of the region visible from an apex. In simple cases with vertical wall boundaries and prismatic obstacles, defined by the *boundary polygon*, the visibility between two points is independent from the elevations of the points. Therefore, the problem can be simplified into a two-dimensional one, in which the visible region of a point must be a simple polygon, called the *visibility polygon*, whose boundary only consists of one cycle of

doi:10.6342/NTU202204140

edges. In recent decades, many algorithms have been developed to compute visibility polygon in various situations, such as in general simple polygon (Lee, 1983), in polygon with sufficient windings (Joe and Simpson, 1987), in polygon with holes, in which the boundary polygon consists of multiple cycles of edges like the case in Fig. 2.1b, (Asano, 1985; Suri and O'Rourke, 1986; Ghosh, 2007), and in a line segment arrangement (Heffernan and Mitchell, 1995). These algorithms typically use the angular sweep method to compute the visibility polygon. They work well for generic configurations but may break down or require special exception-handling for special boundary configurations, for instance those featuring aligned vertices. In the next section, we present the algorithm adopted for the present purpose, designed to be robust for both generic and special cases like aligned vertices.

2.2.2 Visibility polygon algorithm

As in many previous works, we adopt a doubly linked list as data structure to encode the boundary and its decomposition into regions of visibility or non-visibility. We assume that a vector linked by two vertices represents an edge with a solid wall lying on its right-hand side. As demonstrated in Fig. 2.2a, a polygon is bounded by an outer boundary linked by vertices in counterclockwise order. In contrast, the interior boundaries of the polygon (boundaries of obstacles) are linked by vertices in clockwise order. The gray region is therefore defined as the interior of the polygon. If an apex A lies in the interior of the polygon, we can compute its visibility polygon (see Fig. 2.2c) by the following algorithms.

First, we initialize the doubly-linked list of vertices. We store the n vertices of the boundary polygon, including outer or interior boundaries, in an array B listing the coordinates of the vertices. If k represents the index of an arbitrary vertex in B, its next vertex is denoted by k_+ and its previous vertex by k_-, representing pointers to other indexes on the list. The following steps of the algorithm will gradually evolve this boundary polygon until it is decomposed into visible and non-visible

doi:10.6342/NTU202204140

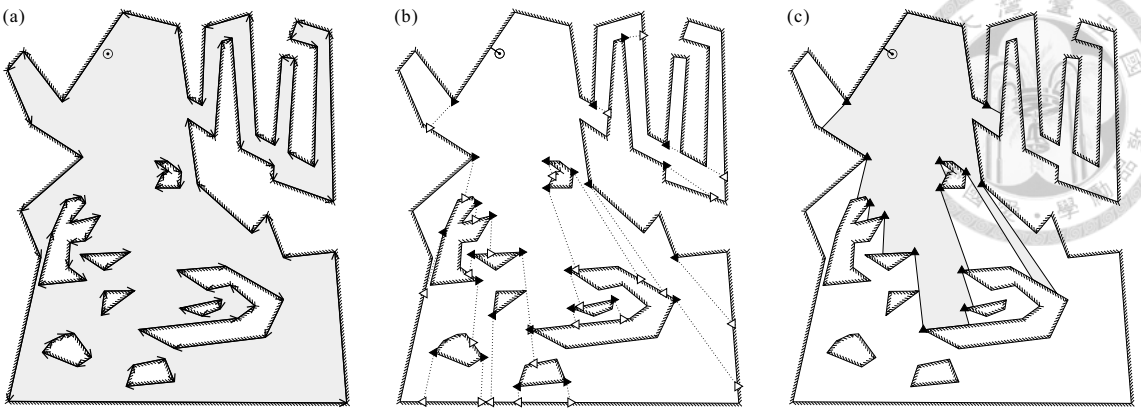

Figure 2.2: (a) A polygon bounded by directed edges. (b) Connecting left corners (black left-pointing triangle) to left intersection points (white left-pointing triangle) and right corners (black right-pointing triangle) to right intersection points (white right-pointing triangle). (c) The visibility polygon and child apex of A.

sub-polygons.

Second, we check if the apex A is on the boundary. If not, we modify the boundary to passing through A. We consider three major situations: First, A lies inside the polygon and not close to the boundary. Second, A lies inside the polygon and very close to the boundary. Third, A lies outside the polygon and close to the boundary. These situations happen when constructing fan morphology on meshed topography.

In the first situation, we find the edge which has the smallest distance to A and the perpendicular foot $A_\perp$ located on the edge to be the nearest edge, e.g. $\overrightarrow{B(i)B(i+1)}$, and the nearest vertex $B(j)$. If A is closer to the nearest edge $\overrightarrow{B(i)B(i+1)}$ than to the nearest vertex $B(j)$, we connect A and $A_\perp$ in two directions, $\overrightarrow{AA_\perp}$ and $\overrightarrow{A_\perp A}$, by updating the doubly-linked list as

$$\begin{gathered}
B(n+1) = A_\perp, B(n+2) = A, B(n+3) = A_\perp, \\
k_+(i) = n+1, k_+(n+1) = n+2, k_+(n+2) = n+3, k_+(n+3) = i+1, \\
k_-(n+1) = i, k_-(n+2) = n+1, k_-(n+3) = n+2, k_-(i+1) = n+3, \\
n = n+3.
\end{gathered} \tag{2.6}$$

doi:10.6342/NTU202204140

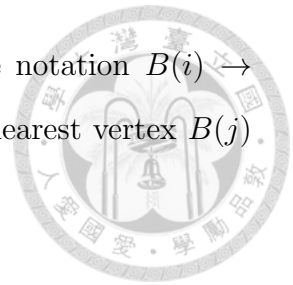

In shorthand, we can express this sequence of steps by the notation $B(i) \rightarrow A_\perp \rightarrow A \rightarrow A_\perp \rightarrow B(i+1)$. Otherwise, we connect A and the nearest vertex $B(j)$ in two directions by updating the doubly-linked list as

$$\begin{aligned} B(n+1) = A, B(n+2) = B(j), \\ k_+(n+2) = k_+(j), k_+(n+1) = n+2, k_+(j) = n+1, \\ k_-(k_+(j)) = n+2, k_-(n+2) = n+1, k_-(n+1) = j, \\ n = n+2. \end{aligned} \tag{2.7}$$

This sequence of step can be written in the shorthand: $B(j) \rightarrow A \rightarrow B(j)$. We will use such shorthand notation below to describe other steps of the algorithm without giving the detailed formulas.

In the second situation, apex A lying inside and very close to the boundary, if A is close enough to the nearest vertex $B(j)$, we modified the location of $B(j)$ to the location of A:

$$B(j) = A. \tag{2.8}$$

Otherwise, we connect the two endpoints of the nearest edge to the apex

$$B(i) \rightarrow A \rightarrow B(i+1). \tag{2.9}$$

In the third situation, apex A lying outside and close to the boundary, if A is close enough to the nearest vertex $B(j)$ and the line segment connecting A and $B(j)$ does not intersect with the nearest edge $\overrightarrow{B(i)B(i+1)}$, we modified the location of $B(j)$) to the location of A. Otherwise, we connects $B(i) \rightarrow A \rightarrow B(i+1)$.

The third step of the algorithm is to find the corners C that limit visibility from apex A. A corner C formed by edges $\overrightarrow{B(k_-(C))C)}$ and $\overrightarrow{CB(k_+(C))}$ must be an obtuse interior angle

doi:10.6342/NTU202204140

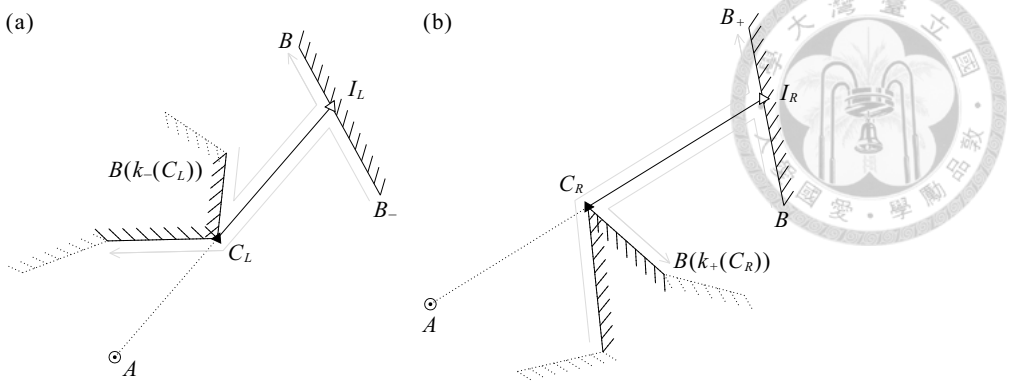

Figure 2.3: Connecting corners and intersection points in two directions to form edges in both visible and invisible regions. (a) Connections for a left corner. (b) Connections for a right corner.

$$\overrightarrow{B(k_-(C))C} \times \overrightarrow{CB(k_+(C))} < 0, \tag{2.10}$$

and either $\overrightarrow{B(k_-(C))C}$ or $\overrightarrow{CB(k_+(C))}$ must be visible to A while the other one must be invisible to A. Edge $\overrightarrow{CB(k_+(C))}$ is visible to A if and only if

$$\overrightarrow{AC} \times \overrightarrow{CB(k_+(C))} \geq 0. \tag{2.11}$$

We categorize all corners into two groups: the left corners and the right corners. A left corner C_L lies on the left-hand side of sight line $\overrightarrow{AC}$ with $\overrightarrow{B(k_-(C))C}$ invisible to A and $\overrightarrow{CB(k_+(C))}$ visible to A; in contrast, a right corner C_R lies on the right-hand side of sight line $\overrightarrow{AC}$ with $\overrightarrow{B(k_-(C))C}$ visible to A and $\overrightarrow{CB(k_+(C))}$ invisible to A. After finding all corners, we sort the corners by their distances to apex A.

The next step of the algorithm is to demarcate the visible and invisible region to apex A occluded by corner C. We find intersection points I with which $\overrightarrow{CI} \parallel \overrightarrow{AC}$ and $\overrightarrow{CI}$ does not intersect with other edges in the boundary as illustrated in Fig. 2.2b. We connect the corners to the intersection points in two directions ($\overrightarrow{CI}$ and $\overrightarrow{IC}$) to form edges in both visible and invisible regions. The connections for generic cases, where I is located on an edge linked by two vertices, are demonstrated in Fig. 2.3. In Fig. 2.3a, for a left corner C_L, if its intersection point $I_L \in \overrightarrow{B_-B}$, we add I_L

doi:10.6342/NTU202204140

into the doubly-linked list to connect the edges in the visible region:

$$B_- \to I_L \to C_L. \tag{2.12}$$

And we add duplicated CL and IL into the doubly-linked list to connect the edges in the invisible region:

$$B(k_-(C_L)) \to C_L \to I_L \to B. \tag{2.13}$$

On the other hand, in Fig. 2.3b, for a right corner C_R, if its intersection point $I_R \in \overrightarrow{BB_+}$, we add I_R into the doubly-linked list to connect the edges in the visible region:

$$C_R \to I_R \to B_+. \tag{2.14}$$

And we add duplicated C_R and I_R into the doubly-linked list to connect the edges in the invisible region:

$$B \to I_R \to C_R \to B(k_+(C_R)). \tag{2.15}$$

For special cases, where I is located right on a vertex B , there are three situations: First, vertex B is not a corner. Second, B is another corner and B and C lie on the opposite sides of the sight line from A. Third, B is another corner and B and C lie on the same side of the sight line from A. In the first and second situations, we modify the doubly-linked list in the similar way as we do in generic cases except we do not add I into the doubly-linked list again in equation (2.13) or (2.15) since I equals to B. In the third situation, B is not the real intersection point I that can form $\overrightarrow{CI}$ to divide the visible and invisible regions occluded by C. Therefore, we ignore B and find the next intersection point of the sight line and edges to be I. And we also remove B from the list of corners.

doi:10.6342/NTU202204140

After connecting all corners to their intersection points in two directions, the polygon is divided into numerous sub-polygons as illustrated in Fig. 2.2b, and the sub-polygon that contains A is the visibility polygon of A. We use a new list to store the vertices of the visibility polygon. We put A into the list first and use k_+ to find the next vertex to put into the list. We repeat the process until the next vertex returns to A to find all vertices of the visibility polygon.

The last step of the algorithm is to obtain the child apexes for apex A. There are two procedures, the first one is essential: remove the corners outside of the visibility polygon since they are not reachable by A and therefore cannot be child apexes of A. The visibility polygon and the effective corners (child apexes) of A are demonstrated in Fig. 2.2c. The second procedure is optional but useful for the polygons with ragged boundaries that we will meet when constructing fan morphology with meshed topography. Corners on a very ragged boundary may only occlude tiny regions from sights of A and can be regarded as ineffective corners since they have no influence on the fan morphology but will significantly decrease the efficiency of the fan morphology algorithm. To identify these ineffective corners, we adopt the same method for finding the vertices of the visibility polygon to find the vertices of the sub-polygon occluded by each corner from the visibility of A. Instead of finding the vertices starting from A, we find the vertices of the sub-polygons starting from the duplicated corners added into the doubly-linked list in equation (2.13) or (2.15). We remove the corners whose occluded sub-polygons are too small and only contain few vertices that initially belong to the same cycle of edges from the list of effective corners (child apexes). The algorithm is summarized as follows:

We conducted various numerical tests to check the above algorithm in generic and special configurations. For generic configurations, we have checked that we obtain the same results as the algorithm of (Ghosh, 2007). We have also tested a number of special configurations like the one illustrated in Fig. 2.2, in which vertices and

doi:10.6342/NTU202204140

Algorithm 1: Visibility polygon from a given boundary polygon and apex

1 Initialize a doubly-linked list, storing the vertices of the boundary polygon in an array B. Use k to represent the vertex index, and k_+ and k_- to be pointers indicating the indexes of the next and the previous vertices.
2 If the apex A is not on the boundary, modify the boundary polygon B to pass through A.
3 Find corners C and connect them to the intersection points I in two directions to divide the polygon into sub-polygons.
4 Obtain the vertices of the visibility polygon by looping around k_+ starting from A.
5 Keep the effective corners as the child apexes for A.
  (a) Remove corners outside of the visibility polygon.
  (b) Remove corners with small influence (optional).

edges were aligned on purpose to cause difficulty, or in which winding regions and multiple obstacles are included. Applied to the shortest path problem, the algorithm combined with equations (2.1)-(2.5) of the previous section were also checked to produce results in agreement with those obtained by (Zhao, 2007; Detrixhe et al., 2013; Valero-Gomez et al., 2013) using the Fast Marching Method or Fast Sweeping Method.

2.2.3 Three-dimensional fan morphology algorithm

In this section, we present the three-dimensional algorithm developed to construct constant-slope fans over an irregular ground surface $\mathcal{G}$. Whereas the method of section 2 was restricted to a horizontal base and vertical walls, here the ground can have arbitrary topography $z(x, y)$, with inclinations that can be milder or steeper than the fan slope S, but excluding overhangs. For illustration, Fig. 2.4a shows one such ground surface, composed of a steep faceted valley upstream of a flat plain. For computational purposes, we assume that the ground surface $\mathcal{G}$ is defined by elevations $z_{ij}^{\mathcal{G}}$ at the nodes (x_j, y_i) of a Cartesian grid.

Upon choosing a primary fan apex A_1, located for example along the valley thalweg, our goal is to determine the resulting fan topography $\mathcal{F}$. We first initialize the fan surface $\mathcal{F}$ to the empty set $\mathcal{F} = \emptyset$. Then we define a cone surface $\mathcal{C}$ with

doi:10.6342/NTU202204140

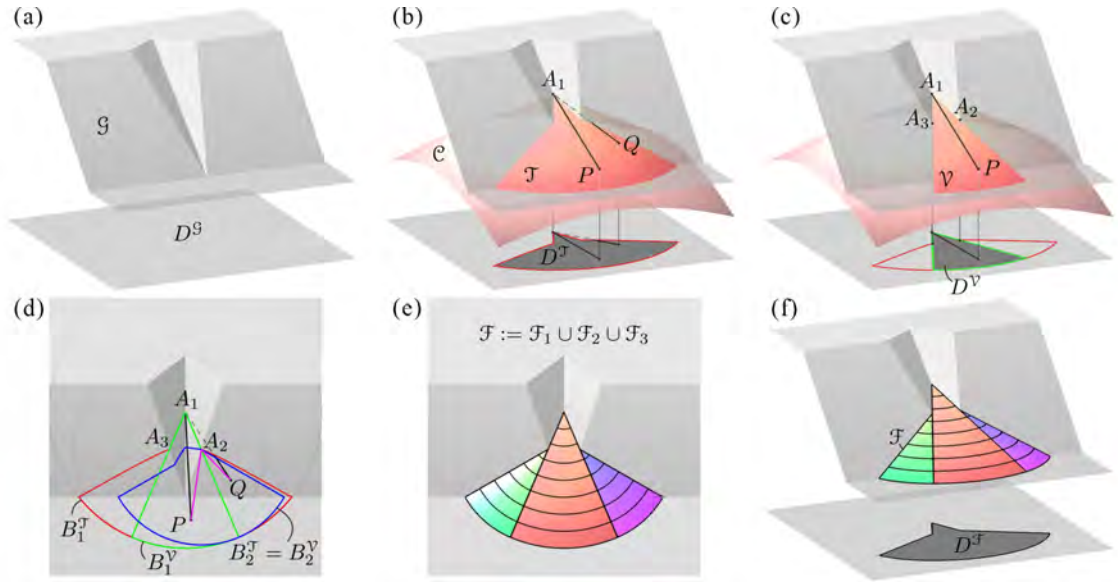

Figure 2.4: Three-dimensional fan morphology algorithm. (a) The ground surface $\mathcal{G}$ and its domain $D^{\mathcal{G}}$ for a simple faceted valley. (b) The cone surface $\mathcal{C}$ with apex A_1 and its truncated surface $\mathcal{T}$, restricted to points $z^{\mathcal{T}} = z^{\mathcal{C}} > z^{\mathcal{G}}$. Potential deposit points P and Q both lie in the domain of the truncated surface $D^{\mathcal{T}}$, but the steepest-descent path to Q hits the ground surface first so that Q is invisible to apex A_1. (c) Visibility surface $\mathcal{V}$ of apex A_1 and its domain $D^{\mathcal{V}}$. $P \in D^{\mathcal{V}}$ since it is visible to apex A_1. The child apexes of A_2 and A_2 lie on the corners diving the boundaries of the truncated surface and visibility surface. (d) Top view of the boundaries of the truncated and visibility surfaces of apex A_1: $B^{\mathcal{T}}_{A_1}$ (red line) and $B^{\mathcal{V}}_{A_1}$ (green line), those of apex A_2: $B^{\mathcal{T}}_{A_2} = B^{\mathcal{V}}_{A_2}$ (blue line), and steepest-descent straight paths to point P and Q from apex A_1 (black lines), and from apex A_2 (magenta lines). (e) Top view of the constant slope fan surface $\mathcal{F}$ consisting of three visible sectors. (f) Perspective view of the final fan complex $\mathcal{F}$.

doi:10.6342/NTU202204140

apex A_1 and slope $S = \tan\alpha$. Its elevation at mesh points is given by

$$z_{ij}^{\mathcal{C}} = Z_1 - S\sqrt{(x_j - X_1)^2 + (y_i - Y_1)^2}, \tag{2.16}$$

where (X_1, Y_1, Z_1) are the coordinates of apex A_1.

Next, we keep only the parts of the cone surface $\mathcal{C}$ that lie above the ground surface $\mathcal{G}$, i.e. such that $z^{\mathcal{C}} > z^{\mathcal{G}}$, yielding a truncated cone surface $\mathcal{T}$. This is done by seeking the zero level set of the difference

$$\Delta z_{ij} = z_{ij}^{\mathcal{C}} - z_{ij}^{\mathcal{G}}, \tag{2.17}$$

using a contouring algorithm. We thus obtain the boundary $B^{\mathcal{T}}$ of the truncated cone domain $D^{\mathcal{T}}$. By adding high walls along the perimeter of the domain $D^{\mathcal{G}}$, we can ensure if needed that the boundary $B^{\mathcal{T}}$ will be formed of closed curves only, possibly more than one.

As illustrated in Fig. 2.4b, we must then further restrict the truncated cone surface $\mathcal{T}$ to remove the parts that are occluded by the ground. We wish to retain only those points P for which the ground $\mathcal{G}$ does not obstruct the path of steepest descent A_1P, and exclude points Q for which obstruction occurs. Although this problem originates in a three-dimensional setting, its solution can be obtained in the two-dimensional plane. Starting from the boundary $B^{\mathcal{T}}$, the unobstructed domain reachable from apex A_1 can be obtained as its visibility polygon. Using Algorithm 1, we therefore compute the visibility polygon $B^{\mathcal{V}}$ and child apexes C of apex A_1. Note that we use Algorithm A.1 to compute the horizontal coordinates of child apexes, and Eq. (2.1) to compute their elevations. The visible domain satisfies the nesting condition $D^{\mathcal{V}} \subseteq D^{\mathcal{T}}$. Restricted to this domain, the visibility surface $\mathcal{V}$ forms part of the desired fan surface $\mathcal{F}$. We can therefore update the fan surface $\mathcal{F}$ to $\mathcal{F} := \mathcal{F} \cup \mathcal{V}$. All mesh points within the unobstructed sector can be identified using a point-in-polygon algorithm, and their elevations set to $z_{ij}^{\mathcal{V}} = z_{ij}^{\mathcal{C}},\ (x_j, y_i) \in D^{\mathcal{V}}$. The above

doi:10.6342/NTU202204140

procedure is shown in perspective in Fig. 2.4c and in plan in Fig. 2.4d. In addition to the visibility polygon, the algorithm may yield child apexes along the sector sides, here apexes A_2 and A_3 located along the canyon ridges. Such apexes must be added to the apex list $\{A\}$, and the procedure repeated starting from the next apex, A_2.

Starting from this new apex A_2, we again define a cone surface $\mathcal{C}$ and obtain its truncated surface $\mathcal{T}$, bounded by boundary $B_2^{\mathcal{T}}$. Using the visibility polygon algorithm, we again restrict $B_2^{\mathcal{T}}$ to the boundary $B_2^{\mathcal{V}}$ of the visible domain $D_2^{\mathcal{V}}$, producing if needed new child apexes. For the example of Fig. 2.4, no obstruction by the ground occurs, hence the two boundaries coincide, $B_2^{\mathcal{V}} = B_2^{\mathcal{T}}$. Accordingly apex A_2 does not give birth to any new child apexes. In general, however, new apexes may need to be generated. Within the restricted region $D_2^{\mathcal{V}}$, we then update the fan surface $\mathcal{F}$ using the statement

$$\begin{cases} z_{ij}^{\mathcal{F}} = \max(z_{ij}^{\mathcal{F}}, z_{ij}^{\mathcal{C}}) & \text{where } z_{ij}^{\mathcal{F}} \text{ exists,} \\ z_{ij}^{\mathcal{F}} = z_{ij}^{\mathcal{C}} & \text{elsewhere,} \end{cases} \tag{2.18}$$

where $z_{ij}^{\mathcal{C}}$ is the cone elevation deduced from apex A_2 at location (x_j, y_i). At the same time, we also record the apex index k associated with each mesh point, which gradually produces a provenance map k_{ij} complementary to the elevation map $z_{ij}^{\mathcal{F}}$.

By the triangle inequality, the fan sector produced by a child apex can never deposit over the sector produced by its mother apex. The maximum operation in Eq. (2.18) is therefore not needed in that case. It is however needed to blend sectors obtained from multiple starting apexes, or from multiple child apexes or their descendants. Consider for instance apex A_3 in Fig. 2.4. After processing apex A_2, we apply the same method to apex A_3 to obtain its cone elevation $z_{ij}^{\mathcal{C}}$ and its visible domain $D_3^{\mathcal{V}}$. Applied within this visible domain, the maximum operation in Eq. (2.18) is needed to update the elevation produced by apex A_2 to the elevation produced by apex A_3, when the latter is higher. For those points, the provenance index $k_{ij} = 2$ is likewise modified to provenance index $k_{ij} = 3$.

doi:10.6342/NTU202204140

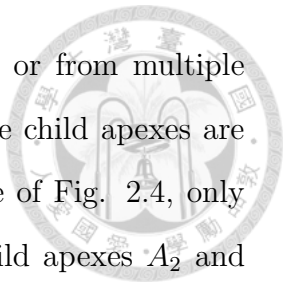

Starting from a single apex, as in the example of Fig. 2.4, or from multiple initial apexes, the above procedure can be iterated until no more child apexes are produced. The fan surface $\mathcal{F}$ is then complete. For the example of Fig. 2.4, only three apexes occur: the single starting apex A_1, and its two child apexes A_2 and A_3. The complete fan surface is then composed of only three fan sectors $\mathcal{F}_1, \mathcal{F}_2$ and $\mathcal{F}_3$, as illustrated in plan in Fig. 2.4e, and in perspective in Fig. 2.4f. As expected from the geometrical properties of constant slope surfaces (Pottmann and Wallner, 2001), the three sectors connect with each other along eikonal rays, across which constant elevation contours share a common tangent. Because for distinct sectors the distances to the corresponding apexes are different, however, the radii of curvature of these contours undergo jumps along the sector boundaries. These features are generic and will be observed also in more complex examples. In this example, boundaries between the fan and the ground are rather simple, coinciding with eikonal rays along the faceted valley slopes, and with circular arcs where the fan intersects the horizontal plain. For more general or irregular topography, such boundaries will become more complex, but exhibit similar features. Segments or arcs of eikonal paths will occur where the fan wraps around steep topography, forming fan margins. Intersection curves, on the other hand, will occur where the fan laps onto the topography, mild or steep, forming fan toe lines.

For more complex topography, or for simple topography represented on a Cartesian grid, the algorithm will generate many more child apexes than those shown on Fig. 2.4. To keep track, a list of apexes $\{A\}$ is updated at each step, starting from the list of initial apexes. Because fan sectors associated with lower apexes cannot bury higher apexes, the list is sorted by elevation and processed in order of decreasing elevation. Each time the visibility algorithm is applied to one of these apexes, a new list of child apexes $\{C\}$ is generated. To avoid burdening the algorithm, two checks are performed before adding these new child apexes to the apex list $\{A\}$. First, it is checked that the new child apexes do not duplicate existing apexes on

doi:10.6342/NTU202204140

the list. Secondly, it is checked that the new child apexes lie sufficiently close to the boundary of their associated fan sector $\mathcal{F}_k$. We then add to the apex list $\{A\}$ only the child apexes $\{C\}$ which satisfy these two conditions, keeping the list $\{A\}$ in order of decreasing elevation. When processing apex A_k, any apex in $\{A\}$ that is yet to be processed and gets buried by the fan sector $\mathcal{F}_k$ is also removed from the list. During the procedure, the apex list $\{A\}$ grows at first, but does not grow indefinitely. Because new child apexes have lower elevations than the apex from which they derive, the procedure is guaranteed to terminate. The result is the desired fan morphology $\mathcal{F}$, and its subdivision as a collection of fan sectors $\mathcal{F}_k$ associated with each of the processed apexes A_k. This completes the algorithm, summarized below in pseudo-code form as Algorithm 2.

The same algorithm also applies to concave fans. The only two steps that require modifications are the calculation of the cone surface $\mathcal{C}$ and the calculation of the elevations of the child apexes C. Instead of Eq. (2.16), we use the following concave profile formula to calculate a concave fan surface with apex A_k

$$z_{ij}^{\mathcal{C}} = Z_k - \frac{S_k}{K}\left(1 - \exp\left(-K\sqrt{(x_j - X_k)^2 + (y_i - Y_k)^2}\right)\right), \tag{2.19}$$

where $S_k = S_1 - K(z_1 - z_k)$. To seek the visible sector of fan surface $\mathcal{C}$, we identify regions connected to apex A_k by eikonal paths that are curved in profile, but straight in plan. We can therefore use Algorithm 2, truncate the concave surface $\mathcal{C}$ by the boundary surface $\mathcal{G}$, and use Algorithm A.1 to find the visible sector and child apexes. We then use the concave profile formula to get the child apex elevations and complete the other steps of Algorithm 2.

doi:10.6342/NTU202204140

Algorithm 2: Algorithm for computing fan morphology with given apex(es) and ground surface.

Initialize Cartesian grid (x_j, y_i) and define the ground surface $\mathcal{G}$ by elevation $z_{ij}^{\mathcal{G}}$. If needed, add a high wall around the boundary of $\mathcal{G}$.

Initialize the provenance k_{ij} to zero and fan surface $\mathcal{F}$ to empty. Store the initial fan apex(es) into the apex list $\{A\}$, sort the list by order of decreasing elevation, and initialize the current apex index k to 1.

while $k \leq$ number of apexes in $\{A\}$ **do**

Select the k-th apex A_k in apex list $\{A\}$ and calculate the cone surface $\mathcal{C}$ with A_k and the constant fan slope S. Truncate the cone surface by finding the zero level set of $\Delta Z_{ij} = Z_{ij}^{\mathcal{C}} - Z_{ij}^{\mathcal{G}}$ to be the truncated surface boundary $B^{\mathcal{T}}$.

Using algorithm 1, restrict $B^{\mathcal{T}}$ to the boundary $B^{\mathcal{V}}$ of its visibility domain, and obtain child apexes of apex A_k.

Find the mesh points within $B^{\mathcal{V}}$ using a point-in-polygon algorithm, and exclude the mesh points where the elevation $z_{ij}^{\mathcal{F}}$ exists and is larger than the elevation $z_{ij}^{\mathcal{V}}$.

Update fan surface elevation $z_{ij}^{\mathcal{F}}$ and record provenance $k_{ij} = k$. Store the child apexes close to the boundary of $\mathcal{F}_k$ in list $\{C\}$.

Check if each child apex in list $\{C\}$ duplicates any existing apexes in the apex list $\{A\}$. If not, add the child apex into list $\{A\}$, keeping the list sorted by order of decreasing elevation.

Check if the new fan sector $\mathcal{F}_k$ buries any of the lower apexes in list $\{A\}$, and remove those apexes from the list.

$k = k + 1$.

end

2.3 Validation with idealized cases

In this section, we validate the algorithm with simple cases that have analytical solutions. The cases including fans on faceted topographies and curved topographies, in which the substrates can be described by plane formulas or cone surface formulas. In the simplest case, whose substrate consists of two planes, we explain the analytical solutions of the fan surface, margins, and toes, whose relation to the substrate can be extended to the more complex cases. We then apply the relation to find the analytical solution of the previous case with faceted valley (Fig. 2.4), in which there are multiple apexes. We compare the analytical solutions to the computational results of the models to preliminarily evaluate the model performance.

doi:10.6342/NTU202204140

We then validate the algorithm on more complicated cases, such as fans on curved topographies, including a crater and a volcano. The two cases are very different: theoretically, there is only an apex in the former case while there are infinite apexes in the later case. Finally, we apply the algorithm to the cases in which there are multiple interacting fans, such as Bajadas. We validate the algorithm by comparing the computational and analytical weld lines between fans.

2.3.1 Faceted topographies

We consider first the simplest case shown in Fig. 2.5 a,c: a single sector constant slope fan on two planes. The ground substrate is composed of a steep inclined plane

$$z(x, y) = y \tan\beta \,, \tag{2.20}$$

of slope $\tan\beta$ steeper than the fan slope $\tan\alpha$, upstream of another plane, horizontal or inclined. We assume a single initial apex A having position $(X, Y) = (0, Y)$ and elevation

$$Z = Y \tan\beta. \tag{2.21}$$

The fan originating from this apex is then a sector of the upright cone

$$z(x, y) = Z - \tan\alpha \sqrt{x^2 + (y - Y)^2} \,, \tag{2.22}$$

The cone intersects the steep inclined plane along the locus

$$y \tan\beta = Y \tan\beta - \tan\alpha \sqrt{x^2 + (y - Y)^2} \,, \tag{2.23}$$

formed by two straight lines through the apex. The corresponding fan margins are given in parametric form by

doi:10.6342/NTU202204140

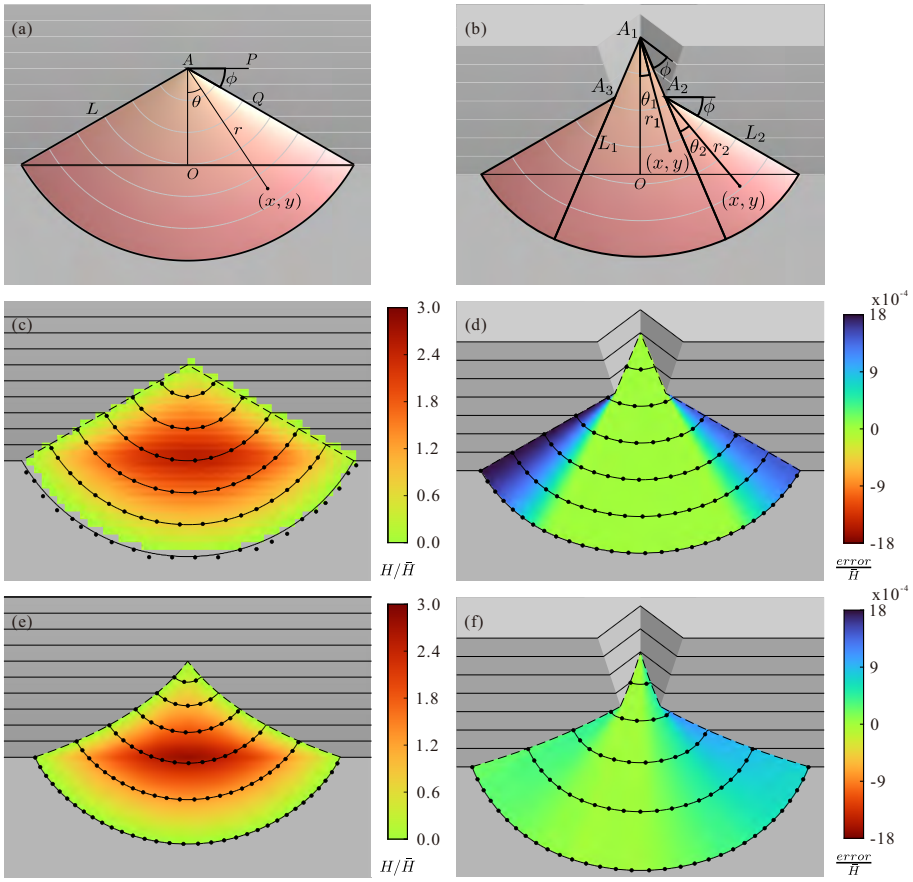

Figure 2.5: Top views of simple and composite fans with analytical solutions. (a,c,e) Terrain composed of two planes; (b,d,f) faceted valley; (a,b) definition sketches for constant slope fans; (c,d) comparison of analytical (lines) and computational results (dots) for constant slope fans (mesh size $d = 0.04L$ in (c) and $d = 0.004L$ in (d)); (e,f) comparison of analytical solutions (lines) and computational results (dots) for concave fans (mesh size $d = 0.004L$). Color in (c,e) shows the computed deposit depth normalized by the average depth. Color in (d,f) represents the elevation error, normalized by the average depth. The dashed lines in (c-f) are the analytical fan margins.

doi:10.6342/NTU202204140

$$(x(s), y(s)) = (\pm s\cos\phi, Y - s\sin\phi), \tag{2.24}$$

where

$$\sin\phi = \frac{\tan\alpha}{\tan\beta}, \tag{2.25}$$

and

$$0 < s < L = \frac{Y}{\sin\phi}\,. \tag{2.26}$$

The fan toe can then be found at the intersection between the cone sector and the downstream plane. When the latter is horizontal ($z(x, y) = 0$), this intersection is the locus

$$Y\tan\beta - \tan\alpha\sqrt{x^2 + (y - Y)^2} = 0\,, \tag{2.27}$$

i.e. an arc of circle of radius L centered at $(0, Y)$. As a result, the fan surface elevation can be calculated from Eq. (2.22) at any point (x, y) that satisfies

$$\begin{cases} r = \sqrt{x^2 + (y - Y)^2} < L \\ -\dfrac{\pi}{2} + \phi \le \theta = \tan^{-1}\dfrac{x}{Y - y} \le \dfrac{\pi}{2} - \phi\,. \end{cases} \tag{2.28}$$

When the apex position Y is changed, we see that the fan grows or shrinks in a self-similar way with respect to the origin $O = (0, 0)$.

In Fig. 2.5c, we compare the analytical fan surface with that computed by the numerical method on a coarse Cartesian grid. The results are in close agreement, but not free from error even in this simple case. Although the analytical solution derives from a single apex, computations on a grid produce multiple child apexes along the margins of the fan. Their positions are slightly away from the true margins, because the contouring algorithm introduces small errors when performing cone-plane inter-

doi:10.6342/NTU202204140

sections on the grid. This in turn induces surface elevation errors, especially close to the margins. The contouring algorithm likewise induces errors when locating the toe boundary of the fan. We present the influence of mesh size on computational errors in Section 2.5.

For the second case (Fig. 2.5b,d), we consider a constant slope fan on the faceted valley used earlier (Fig. 2.4) to describe our method. For this case, the analytical solution features three cone sectors: a central lobe, visible from the primary apex, and two side lobes associated with corner apexes located along the side ridges of the canyon. We derive the analytical solution as follows.

The V-shaped canyon is formed by two inclined planes of equation

$$z(x, y) = \tan\beta \, (\pm x \sin\psi + y \cos\psi) \, . \tag{2.29}$$

Along the thalweg of this valley, we place the initial apex of the fan at position $(X_1, Y_1) = (0, Y_1)$ and elevation

$$Z_1 = Y_1 \tan\beta \cos\psi. \tag{2.30}$$

Within the canyon, the fan will have margins formed by two straight lines at angle ϕ relative to the plane contours, and given in parametric form by

$$(x(s), y(s)) = (\pm s \cos(\phi + \psi), Y_1 - s \sin(\phi + \psi)). \tag{2.31}$$

The same straight lines also delineate the central sector visible from apex A_1. The intersection of this sector with the horizontal plain forms a circular arc

$$\frac{\tan\beta}{\tan\alpha} Y_1 = \sqrt{x^2 + (y - Y)^2}, \tag{2.32}$$

where

doi:10.6342/NTU202204140

$$-\frac{\pi}{2}+\phi+\psi \leq \theta_1 = \tan^{-1}\frac{x}{Y_1-y} \leq \frac{\pi}{2}-\phi-\psi. \tag{2.33}$$

Two child apexes, A_2 and A_3 are produced at the intersection of the margins with the ridge lines connecting the canyon with the mountain front. The ridges are the intersections of the two planes in Eq. (2.29) with the plane in Eq. (2.20), and given in parametric form by

$$(x(t), y(t)) = \left(\pm\cos\left(\tfrac{\pi-\psi}{2}\right)t, \sin\left(\tfrac{\pi-\psi}{2}\right)t\right). \tag{2.34}$$

The two child apexes A_2 and A_3, therefore, have analytical positions

$$(X_2, Y_2) = (-X_3, Y_3) = \left(\frac{Y_1}{\tan(\phi+\psi)+\tan\left(\frac{\pi-\psi}{2}\right)}, \frac{\tan\left(\frac{\pi-\psi}{2}\right)Y_1}{\tan(\phi+\psi)+\tan\left(\frac{\pi-\psi}{2}\right)}\right) \tag{2.35}$$

and elevation

$$Z_2 = Z_3 = Z_1 - \tan\alpha\frac{\tan(\phi+\psi)Y_1}{\tan(\phi+\psi)+\tan\left(\frac{\pi-\psi}{2}\right)}. \tag{2.36}$$

Likewise, we can determine the side margins and toe lines bounding the cone sectors associated with apexes A_2 and A_3. The elevation of the three cone sectors and their boundaries can therefore be obtained analytically, and combined into a fan complex. We find that this fan complex is again self-similar with respect to the origin $O = (0, 0)$. However, the fan is no longer radially symmetric. Instead, the contour associated with a given elevation is more strongly curved in the side sectors than in the central sector.

In Fig. 2.5d, we compare the analytical fan surface with that computed by the numerical method on a fine Cartesian grid. On this fine grid, the analytical and numerical contours are indistinguishable, so we use color to show the elevation error, normalized by the average deposit thickness. Errors are small overall, but greater

doi:10.6342/NTU202204140

in the side sectors than in the central sector. This is again due to inaccuracies in the positioning of child apexes along margins and ridge lines, when performed on a Cartesian grid. These errors accumulate over successive generations of child apexes. They therefore affect more strongly the side sectors, produced by more distant descendants of the initial apex.

We then consider concave fans on the same topographies (Fig. 2.5e,f). In both cases, the fans are formed of multiple concave cone sectors having apexes located along the fan margins. For these two cases, implicit analytical solutions can be found. For the third case (Fig3e), we consider a single sector concave fan on two planes where the ground substrate is the same as the one in the first case. The slope $\tan\alpha$ of the concave fan is decreasing with elevation

$$\tan\alpha(z) = \tan\alpha_0 - (Z - z)K \tag{2.37}$$

where $\tan\alpha_0$ and Z are slope and elevation of the fan apex A, and K is the concavity. As for the previous two cases, the angle ϕ between the fan margins to the contours of the inclined plane depends on the ratio of the fan slope $\tan\alpha$ and the inclined plane slope $\tan\beta$. Therefore, the angle ϕ will decrease with elevation as

$$\phi(z) = \sin^{-1}\frac{\tan\alpha(z)}{\tan\beta} \tag{2.38}$$

from $\phi_0 = \sin^{-1}(\tan\alpha_0/\tan\beta)$ to $\phi_{toe} = \sin^{-1}(\tan\alpha_0/\tan\beta - ZK/\tan\beta)$. Therefore, the margins will gradually open toward the side along the locus

$$x_m = X \pm \int_{y_m}^{Y} \frac{dy}{\tan\phi}, \tag{2.39}$$

where (X, Y) is the location of apex A and (x_m, y_m) is a point on the margins. After integration, the margin is obtained in parametric form as

doi:10.6342/NTU202204140

$$\begin{cases} x_m = X \pm \dfrac{1}{K}\left(\log\left(\dfrac{\cos\phi_0 + 1}{\cos\phi + 1}\dfrac{\sin\phi}{\sin\phi_0}\right) + \cos\phi - \cos\phi_0\right) \\ y_m = Y - \dfrac{\sin\phi_0 - \sin\phi}{K}. \end{cases} \tag{2.40}$$

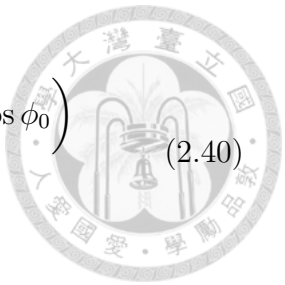

An arbitrary point (x, y) on the fan surface can be connected to the margins by an eikonal ray, so that its elevation can calculated from

$$z = z_m - \frac{\tan\alpha}{K}\left(1 - \exp\left(-K\sqrt{(x - x_m)^2 + (y - y_m)^2}\right)\right), \tag{2.41}$$

where $z_m = Z - (Y - y_m)\tan\beta$ is the elevation of the margin point (x_m, y_m). If the angle between the contour of the inclined plane and the line segment connecting point (x, y) and apex A is larger than ϕ_0, then (x, y) is visible to apex A. The eikonal ray will pass through apex A and we can substitute (X, Y) into Eq. (2.41). Otherwise, the eikonal ray will be tangential to the margin at (x_m, y_m) at angle ϕ

$$\frac{x_m - x}{y_m - y} = \pm\tan\phi. \tag{2.42}$$

We can solve the equation implicitly to obtain ϕ, and then calculate z.

For the fourth case (Fig3f), we consider a single sector concave fan on the same faceted valley as in the second case. We can combine the concepts used for the previous two cases to solve this new case. We first determine the margins within the canyon by rotating the margins obtained in the previous case by angle Ψ. Then we implicitly solve the intersections of the margins and the two ridge lines to obtain the child apexes A_2 and A_3. Next, we solve the margins from the child apexes to the fan toe. Last, we find the eikonal ray connecting the margins for each point on the fan and calculate the fan elevation.

In Fig. 2.5e,f, we compare the analytical fan surfaces with those computed by our algorithm on fine Cartesian grids. On the fine grids, the contours from the two methods are indistinguishable. In Fig. 2.5e, we use color to show a map of fan

doi:10.6342/NTU202204140

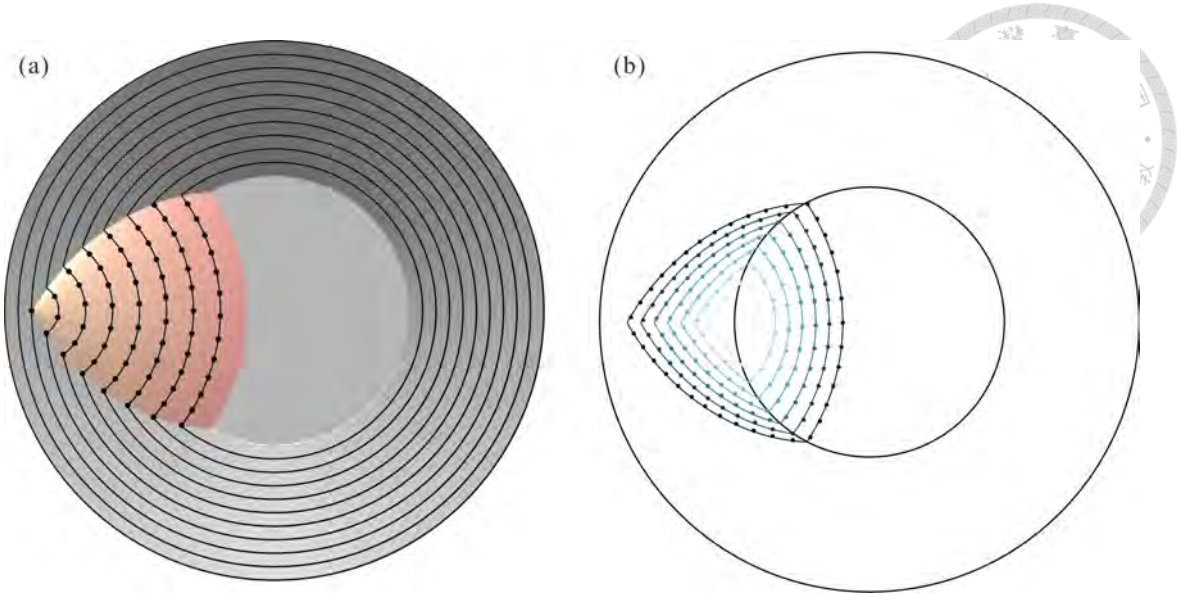

Figure 2.6: (a) Top view of a fan on a crater. Line: contours of analytical fan elevation; dot: contours of computational fan elevation. (b) Fan boundaries changing with apex position. Line: analytical solution; dot: computational result.

deposition depth. In Fig. 2.5f, we use color to show the normalized elevation error. The overall errors are small and again greater in the side sectors than in the central sector.

2.3.2 Curved topographies

As illustrated in Fig. 2.6a, we considered a crater bounded by a horizontal plain

$$z(x, y) = 0. \tag{2.43}$$

and an inverted cone

$$z(x, y) = Z_0 + \tan\beta\sqrt{x^2 + y^2} \tag{2.44}$$

where $Z_0 < 0$.

A constant slope fan can be described in eq. 2.22 with slope $\tan\alpha$ smaller than $\tan\beta$ and apex A at position $(X, Y) = (X, 0)$, where $X < 0$, and elevation

doi:10.6342/NTU202204140

$$Z = Z_0 + \tan\beta(0 - X). \tag{2.45}$$

We find the fan toe in the same way as in the previous cases, so that the fan toe is an arc of a circle with radius $-X + \frac{Z0}{\tan\beta}$ centering at $(X, 0)$. We find the fan margin as the intersection of the two cones, so that

$$Z_0 + \tan\beta\sqrt{x^2 + y^2} = Z_0 - \tan\beta X - \tan\alpha\sqrt{(x - X)^2 + y^2}. \tag{2.46}$$

This can yield the curve in parameter form

$$(x, y) = (X + r\cos\theta, r\sin\theta) \tag{2.47}$$

where

$$r = \frac{-X(\tan^2\beta - \tan^2\alpha\cos\theta - \sqrt{\tan\alpha^2(1 - cos\theta)(2\tan\beta^2 - \tan\alpha^2(1 + cos\theta))})}{\tan\beta^2 - \tan\alpha^2}. \tag{2.48}$$

Since the curve is concave, the region bounded by the fan margin and toe is all visible to the apex and there is no more apex.

We compare the analytical and computational fan surface elevations in Fig. 2.6a and we compare the analytical fan margins and fan toes to the computational fan boundaries of a series of fans with various apex positions in Fig. 2.6b. The algorithm can capture the fan that grows without self-similarity.

In the next case, we consider a volcano described by the cone

$$z(x, y) = Z_0 - \tan\beta\sqrt{x^2 + y^2} \tag{2.49}$$

and a constant-slope fan with a primary apex at $(X, Y) = (R_0, 0)$, as illustrated in Fig. 2.7b,d.

doi:10.6342/NTU202204140

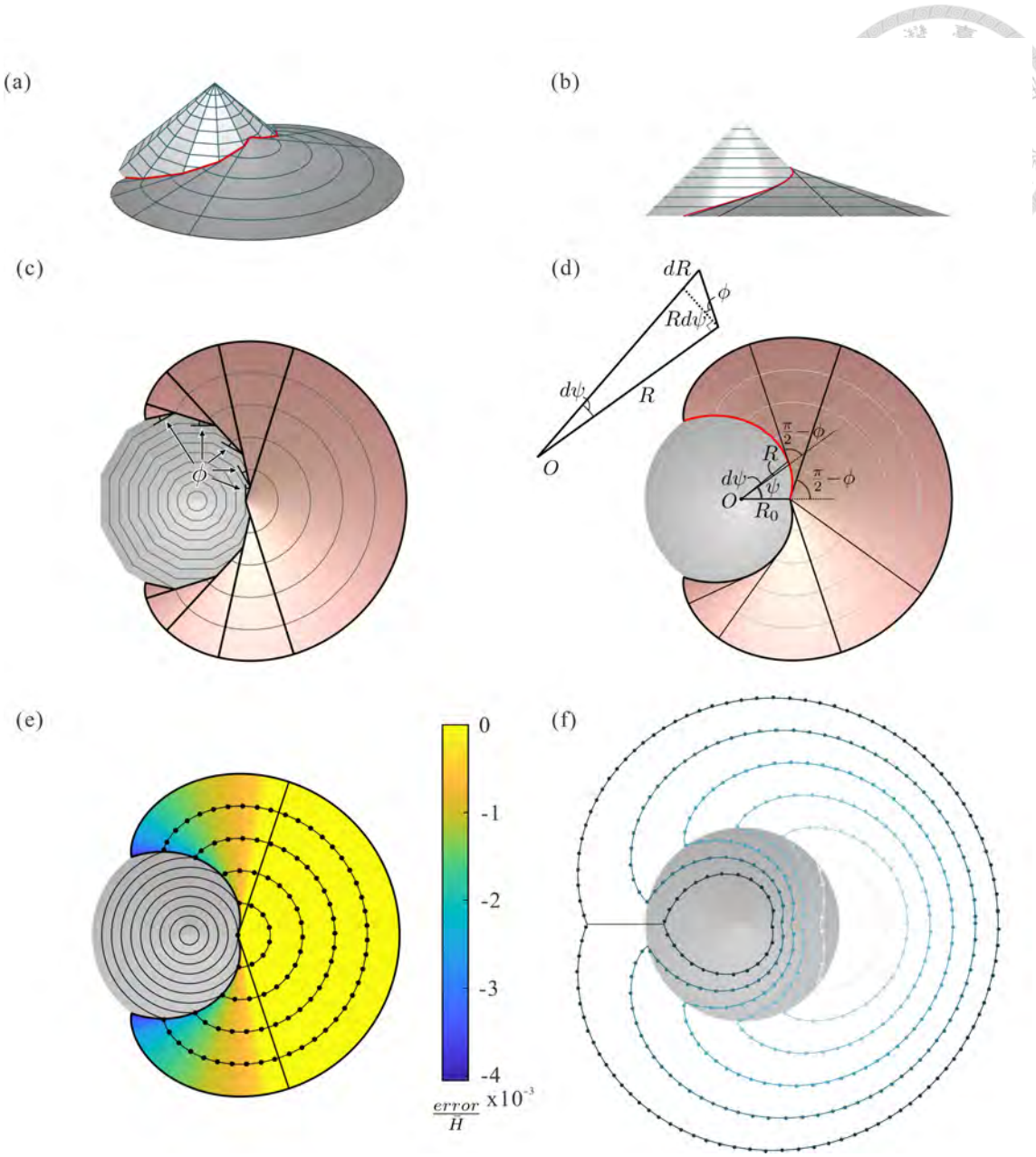

Figure 2.7: (a) Perspective view a fan on a dodecagonal pyramid. (b) Side view of a fan on a cone. (c) Top view of a fan on a dodecagonal pyramid. (d) Top view of a fan on a cone. (e) Comparison of analytical solution (line) and computational result (dot). Colors represent the error between the computational and analytical fan deposit depths over analytical average deposit depth. (f) Fan boundaries changing with apex position. Line: analytical solution; dot: computational result.

Before deriving the analytical solution of the fan morphology, we use a fan on a pyramid to present the concept (Fig. 2.7a,c). By using the method presented in the previous subsection, we can derive that the fan on pyramid consists of a series of cone sectors. The cone sectors have apexes located on the fan margin. And the

doi:10.6342/NTU202204140

margin consists of straight line segments that are set at an angle, ϕ, to the contours of the substrate.

Increasing the number of the faces of the pyramid to infinity, we can obtain the fan on a cone and the margin of the fan will approach two logarithmic spirals (Fig. 2.7d). The logarithmic spiral has the property that the angle between a radius vector from the origin O to a point on the margin and the tangent at the point is a constant, which is $\frac{\pi}{2} - \phi$ in this case. If point $(x, y) = (R\cos\psi, R\sin\psi)$ is on the margin, then

$$\frac{dR}{Rd\psi} = \tan\phi. \tag{2.50}$$

Rearranging and integrating the equation yield

$$R = R_0 e^{\tan\phi|\psi|}, \tag{2.51}$$

where $-\psi_{max} < \psi < \psi_{max}$. Considering the elevation drop along the margin equals to the fan height

$$\frac{\tan\alpha}{\cos\phi}\int_0^{\psi_{max}} R_0 e^{\tan\phi|\psi|}d\psi = Z_0 - R_0\tan\beta, \tag{2.52}$$

we can derive

$$\psi_{max} = \ln\left(\frac{Z_0}{R_0\tan\beta}\right)\frac{\tan\alpha}{\cos\phi} = \ln\left(\frac{Z_0/\tan\beta}{R_0}\right)\frac{1}{\tan\phi}. \tag{2.53}$$

An arbitrary point (x, y) on the fan surface can be connected to the margin by the eikonal ray (the maximum decent path with slope $\tan\alpha$). We define θ as the angle between the eikonal ray and x direction and λ as the length of the eikonal ray from the margin point $(R\cos\psi, R\sin\psi)$ to the point (x, y). Therefore, the position and elevation of the point can be presented as

doi:10.6342/NTU202204140

$$(x, y, z) = (R\cos\psi + \lambda\cos\theta, R\sin\psi + \lambda\sin\theta, Z_0 - R\tan\beta - \lambda\tan\alpha) \quad (2.54)$$

If point (x, y) is visible to the fan apex $(R_0, 0)$, then the eikonal ray passing through it will point to the fan apex, and

$$\begin{cases} \theta = \tan^{-1}\left(\dfrac{y}{x - R_0}\right) \leq \dfrac{\pi}{2} - \phi \\ \lambda = \sqrt{(x - R_0)^2 + y^2} \leq \dfrac{Z_0 - R_0\tan\beta}{\tan\alpha} \\ \psi = 0. \end{cases} \quad (2.55)$$

Otherwise, the eikonal ray will be a tangent of the margin at $(R\sin\psi, -R\cos\psi)$ and

$$\begin{cases} \theta = \tan^{-1}\left(\dfrac{x - R\cos\psi}{y - R\sin\psi}\right) \\ \lambda = \sqrt{(x - R\cos\psi)^2 + (y - R\sin\psi)^2} \leq \dfrac{Z_0 - R\tan\beta}{\tan\alpha} \\ \psi = \theta - \dfrac{\pi}{2} + \phi. \end{cases} \quad (2.56)$$

To determine the tangent point $(R\cos\psi, R\sin\psi)$ for a given point (x, y), we exploit the derivative of the margin (logarithmic spiral)

$$\begin{cases} \dfrac{dx}{d\psi} = \dfrac{dR}{d\psi}\cos\psi - R\sin\psi \\ \dfrac{dy}{d\psi} = \dfrac{dR}{d\psi}\sin\psi + R\cos\psi, \end{cases} \quad (2.57)$$

and obtain

$$\frac{y - R\sin\psi}{x - R\cos\psi} = \frac{\frac{dR}{d\psi}\sin\psi + R\cos\psi}{\frac{dR}{d\psi}\cos\psi - R\sin\psi}. \quad (2.58)$$

Substituting eq. 2.50 into the equation yields

$$(-x\tan\phi - y)\sin\psi + (y\tan\phi - x)\cos\psi + R_0 e^{\tan\phi|\psi|} = 0. \quad (2.59)$$

doi:10.6342/NTU202204140

We can solve the equation implicitly to obtain ψ, obtain R in eq. 2.51, and calculate the elevation z in eq. 2.54. We compare the analytical and computational fan surface elevations and deposit depths in Fig. 2.7e. The figure shows that the error accumulated along angle θ. In the region where the eikonal rays point to the fan apex, the computational solution approach the analytical solution so that the error is extremely small. We compare the analytical and computational fan boundaries of a series of fans with various apex positions in Fig. 2.7f. It can be seen that the fan grows and bends around the volcano while the apex moves upward, and finally the fan will interact with itself and form a weld line. Since the fan is symmetric, the weld line is a straight line. We explain in the next subsection how to deal with the weld line for non-symmetrical cases.

2.3.3 Interacting fans with weld lines

In this subsection, we discuss the weld lines formed along with multiple interacting fans. We first consider fans with the same slope, $\tan\alpha$, on a steep inclined plane with slope $\tan\beta$ upstream of a horizontal plane. If two adjacent fans, whose apexes A_1 and A_2 are located at (X_1, Y_1) and (X_2, Y_2), are close enough, they interact with each other and form a weld line. The weld line starts at the intersection of the two fan margins

$$\begin{cases} (x(s), y(s)) = (X_1 + \cos\phi s, Y_1 - \sin\phi s) \\ (x(t), y(t)) = (X_2 - \cos\phi t, Y_2 - \sin\phi t), \end{cases} \tag{2.60}$$

where ϕ is the angle from the margin to the contour of the inclined plane (eq. 2.25). And the weld line ends at the intersection of the two fan toes

$$\begin{cases} \tan\beta Y_1 - \tan\alpha\sqrt{(x - X_1)^2 + (y - Y_1)^2} = 0 \\ \tan\beta Y_2 - \tan\alpha\sqrt{(x - X_2)^2 + (y - Y_2)^2} = 0. \end{cases} \tag{2.61}$$

Along the weld line, the elevations of point (x, y) calculated from apexes A_1 and

doi:10.6342/NTU202204140

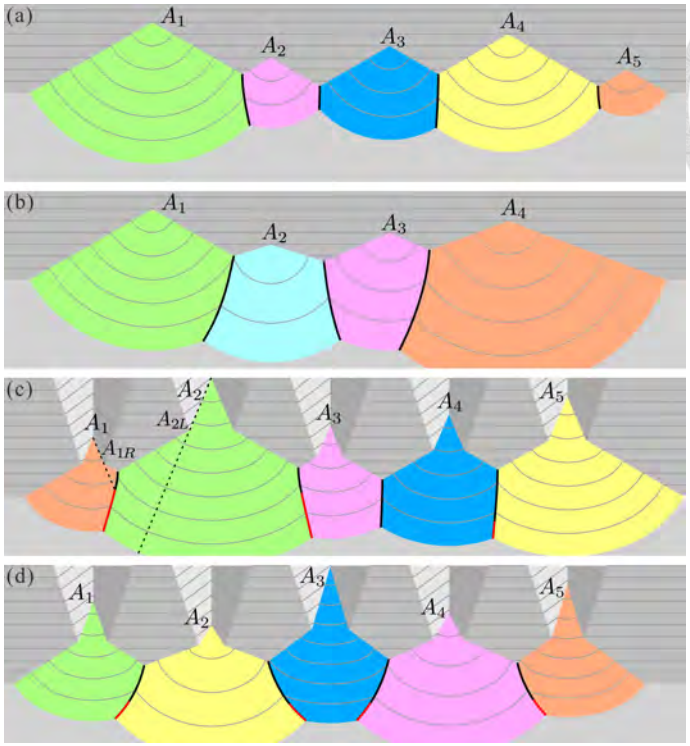

Figure 2.8: Coalescing fans (bajadas) along idealized mountain fronts. (a) Fans of the same slope on a plane mountain front. (b) Fans of different slopes on a plane mountain front. (c) Fans of the same slope at the mouths of faceted valleys. (d) Fans of different slopes at the mouths of faceted valleys. The plots show the contours (thin lines) and provenance (color) of the computed fans, together with the analytical weld line paths (bold lines).

A_2 are the same

$$Z_1 - \tan\alpha\sqrt{(x-X_1)^2+(y-Y_1)^2} = Z_2 - \tan\alpha\sqrt{(x-X_2)^2+(y-Y_2)^2} = 0, \quad (2.62)$$

where Z_1 and Z_2 are the apexes elevations. Therefore, the weld line is a hyperbola and can be solved implicitly. We input the apexes of the series of fans and the fan slope, $\tan\alpha$ into the algorithm and use the resulted provenance map to track the domain of each fan. The result is shown in Fig. 2.8a. We plot the analytical weld lines on it and find that the analytical and computational results fit each other well.

In the next case, we consider a series of fans with various slopes. We input the apex and slope of a fan into the algorithm by turns to obtain the morphology of the

doi:10.6342/NTU202204140

fan series and the domain of each fan (Fig. 2.8b). In this case, it should be noticed that the weld line between two fans may compose of a spiral with numerous child apexes if it extends to the invisible region of one of the fan apex. To simplify, we choose the conditions that will not lead to such situation so that the weld line is always visible to the apexes of the two fans. Therefore, the weld line can be solved analytically by modifying eqs. 2.60-2.62 to adopt various fan slopes. Though the weld line is not hyperbola, it can also be solved implicitly. We draw the analytical weld lines onto Fig. 2.8b and find they lie exactly on the intersections of the fan domains.

Next, we consider fans originating from a series of faceted valleys, such as Bajada. We also apply the algorithms to the fans with the same slope (Fig. 2.8c) and the fans with various slope (Fig. 2.8d). In these cases, to solve the weld lines analytically, we need to calculate the position of the child apexes on the ridges in eqs. 2.35 and 2.36 first. We calculate the intersection of the two margins starting from the two close child apexes (A_{1R} and A_{2L}) to be the upstream point of the weld line. We adopt the position of A_{1R} and A_{2L} to solve the weld line (eq. 2.62) and calculate the intersections of the weld line and the rays $\overrightarrow{A_1A_{1R}}$ and $\overrightarrow{A_2A_{2L}}$ to check if the weld line is visible to apexes A_1 or A_2. If the weld line is visible to apex A_1, the weld line needs to be segmented. The lower part of the weld line and the endpoint of it are solved in eq. 2.62 and 2.61 with the position of A_1 and A_{2L}. We plot the analytical weld lines of the two cases in Fig. 2.8c, d, and they fit the intersections of the computational fans. This is a validation that the algorithm can be applied to the cases with fans from a series of tributaries and with various slopes, which can be seen frequently in fields.

2.4 Validation with field cases

In this section, we apply our proposed method to two field sites for which we have acquired detailed topographic data. The two sites, illustrated in Fig. 2.9, feature

doi:10.6342/NTU202204140

Figure 2.9: Field sites in Taiwan's montane areas selected to test the proposed algorithm. (a,b) Tributary fan formed along the Zhuoshui River, Central Taiwan; (c,d) highly active debris flow fan at the confluence of the Laonong River with its Pu-Tun-Pu-Nas tributary, southwestern Taiwan. (a) Surveyed contours (2017) and satellite image (2015); (b) ground photo (2017); (c) surveyed contours (2018) and satellite image (2018); (d) UAV photo taken in 2019. Source of the satellite images: Google Earth.

debris fan landforms typical of Taiwan's montane areas. Fans in such areas usually originate from small (<50 km^2) and steep (slope 0.5 to 2.7 m/m) tributary catchments, and deposit in trunk river valleys of milder inclination (slope < 0.03 m/m). The resulting fans have small fan areas (<2 km^2) and intermediate fan slopes (0.05 to 0.2 m/m) (Chang et al., 1995). Although exposed to different climates, similar tributary-junction fans are common in mountainous areas around the world (Gómez-Villar et al., 2006; Al-Farraj and Harvey, 2005; Stokes and Mather, 2015; Leenman and Tunnicliffe, 2020).

Figure 2.9a,b, shows the first study site, a fan formed along the Zhuoshui River

doi:10.6342/NTU202204140

in Central Taiwan. This fan has an area of 0.064 km^2 and slopes of 0.14 to 0.19 m/m, and has not significantly evolved in recent years. It is roughly semi-conical in shape. As the fan toe has not been trimmed by the trunk river, it connects continuously with the wide, even river bed surface. Along its margins, however, the fan connects with steep, irregular valley sides. We acquired the fan topography by photogrammetry in 2017, using an unmanned aerial vehicle (UAV), with the assistance of the Computer-Aided Engineering Group of the Department of Civil Engineering, NTU. This case is chosen to verify that the algorithm can mimic the morphology of field fans in comparatively simple conditions.

Figure 2.9c,d, shows the second study site, the confluence of the Pu-Tun-Pu-Nas tributary with the Laonong River, in Southwestern Taiwan. The site exhibits elevated, vegetated fan terraces formed by ancient debris episodes dated from 6500 to 160 years before present (Hsieh and Chyi, 2010; Hsieh and Capart, 2013). In recent decades, it has experienced significant fan aggradation due to a series of debris flows originating from the tributary catchment, alternating with periods of incision and trimming by the trunk river (Hsieh and Capart, 2013; Capart et al., 2010). The currently active debris fan has a total area of 1.01 km^2 and slopes ranging from 0.08 to 0.105 m/m. Between 2010 and 2020, we acquired repeat topographic surveys of the site using Airborne LiDAR and UAV photogrammetry. At this site, the remnants of the ancient debris fans form complex boundary conditions for renewed fan aggradation, including an island around which diffluences and confluences may occur. To test our algorithm in these more complex conditions, we apply it to an aggradation episode for which the topography both before and after the event is well documented.

We first apply the algorithm to the fan in the Zhuoshui river valley. For this case, a high resolution (1 m) digital elevation model (DEM) of the 2017 fan was acquired by photogrammetry (shown in Fig. 2.10a). Since no topography data is available for the situation before fan formation, we use instead a hypothetical topography as

doi:10.6342/NTU202204140

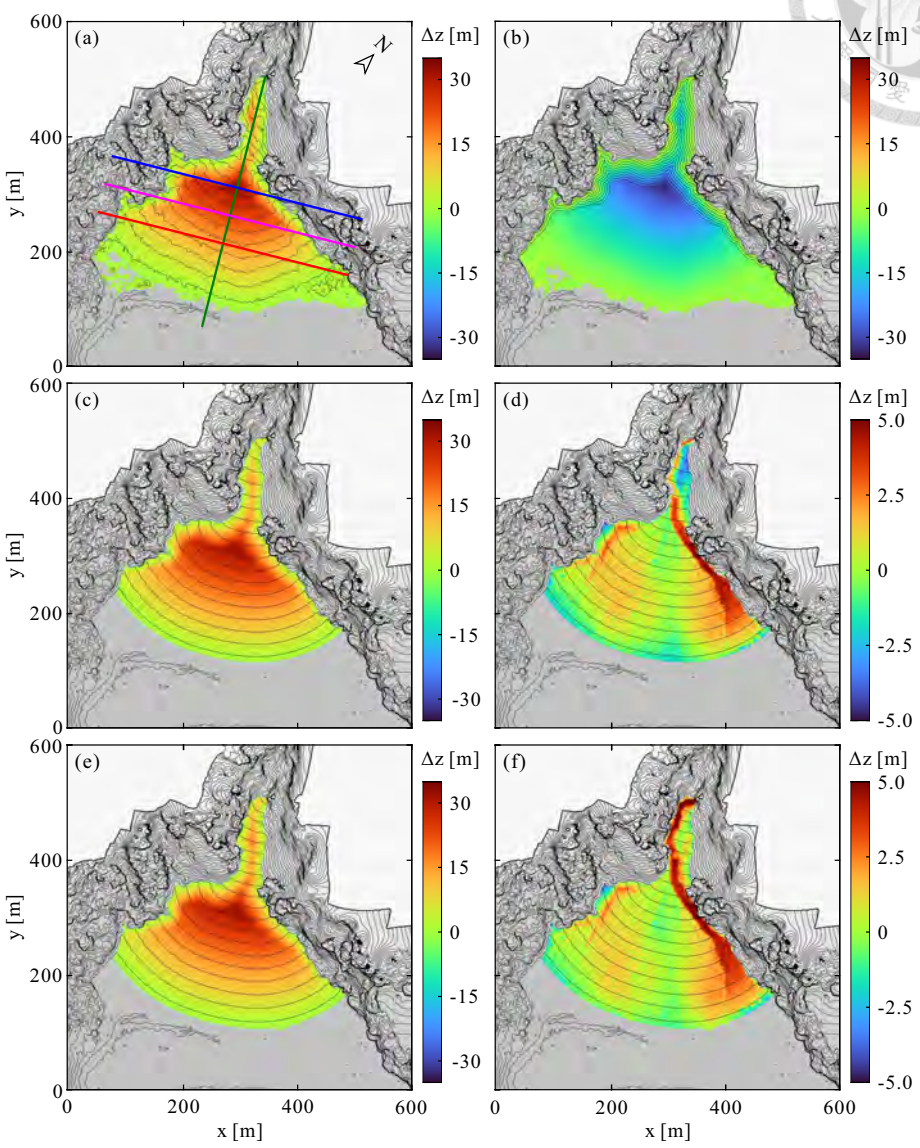

Figure 2.10: Application to the Zhuoshui River tributary-junction fan. (a) Surveyed topography (contours) and associated deposit thickness $\Delta z = z_{2017} - z_0$ (color); (b) hypothetical valley topography $z_0(x, y)$ (contours) provided as initial condition to the simulation, upon artificially depressing the topography by thickness $\Delta z = z_0 - z_{2017}$ (color); (c) simulated constant slope fan topography (contours) and deposit thickness $\Delta z = z - z_0$ (color); (d) simulated constant slope fan topography (contours) and error $\Delta z = z - z_{2017}$ (color); (e) Simulated concave fan topography (contours) and deposit thickness $\Delta z = z - z_0$ (color); (f) simulated concave fan topography (contours) and error $\Delta z = z - z_{2017}$ (color). Lines: elevation contours at intervals of 3.5 m. Colored lines in (a): transects for the profiles shown in Fig. 2.11.

doi:10.6342/NTU202204140

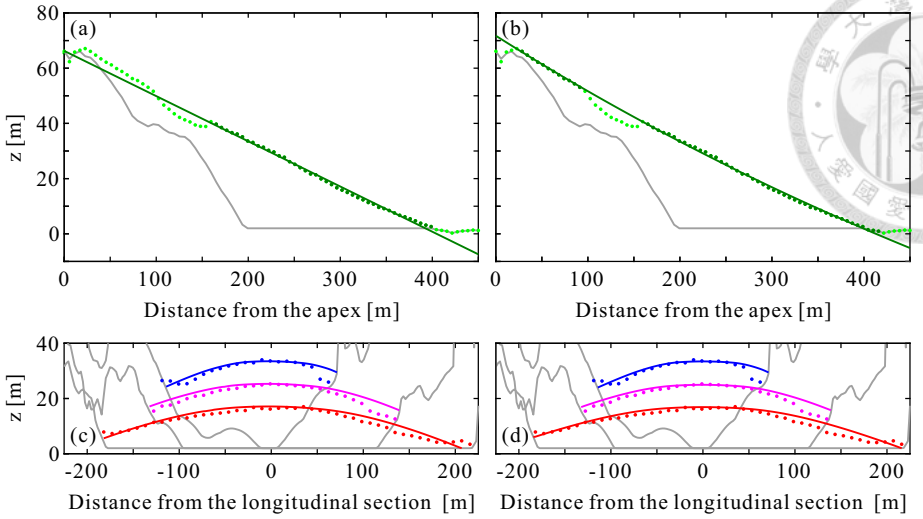

Figure 2.11: Profiles of the Zhuoshui River tributary-junction fan. (a) Longitudinal profile with constant slope fit (slope $S = 0.1637$) (b) Longitudinal profile with concave fit (concavity $K = 0.964$ km^{-1}, apex slope $S_A = 0.211$). Dark green dots: data used for fitting; light green dots: data not used for fitting; dark green lines: fitted profiles. (c,d) Comparison of simulated and surveyed elevations for three transverse profiles (blue: 200 m, magenta: 250 m, red: 300 m from the apex). Colored dots: survey data; colored lines: simulated profiles; gray lines: assumed valley topography.

initial condition. For this purpose, we delineated the boundary of the fan by using the surface gradient to identify fan margins, and a low elevation contour to identify the fan toe. Within this boundary, a surface of constant slope extending the valley sides downwards was generated from apexes along the margins, and truncated by a horizontal surface set at the toe elevation. Figure 2.10b shows the thickness removed in this way, and the resulting initial topography $z_0(x, y)$.

Figure 2.11 shows the longitudinal fan profile and three orthogonal transects, shown in plan on Fig. 2.10a. In Fig. 2.11a,b, gray lines represent the hypothetical topography, highlighting the contrast between the steep mountain sides and the mild-sloped (assumed horizontal) trunk river bed. Green dots represent the surveyed fan topography. We use the data in the main fan region (dark green dots in Fig. 2.11a) to fit a constant slope profile (line in Fig. 2.11a) and include the upstream data (dark green dots in Fig. 2.11b) to fit a concave profile (line in Fig. 2.11b). Although using a curved profile allows a better fit, for this debris fan the concavity

doi:10.6342/NTU202204140

is small ($K = 0.964$ km^{-1}). The fitted constant slope and concave profiles differ in the proximal and distal zones of the fan, but match closely in the main fan region.

To simulate the morphology of the fan, the dependence of slope on elevation is assumed to follow the fitted profiles. We run the algorithm starting from a single apex, placed upstream within the narrow canyon that supplies the fan with debris. We first set the fan slope S as the fitted constant slope in Fig. 2.11a. Simulation results are shown in Fig. 2.10c. By construction, the simulated fan surface has constant surface gradient, and therefore features equally spaced contours. As observed earlier for the simple case of Fig. 2.5d, the contours are not radially symmetric. Instead, they curve more strongly within side sectors of the fan, as these originate from corner apexes located at the downstream end of the canyon. The less curved contours within the central sector, by contrast, originate from apexes further upstream within the canyon. Unlike the simple case of Fig. 2.5d, here the fan must lap onto or wrap around highly irregular topography along its left and right margins. By creating child apexes as needed, the algorithm deals well with this irregularity, and succeeds in connecting the fan surface continuously to the ground topography along the entire fan boundary.

We then let the fan slope S vary with elevation, following the fitted concave profile shown in Fig. 2.11b. The simulated concave fan is shown in Fig. 2.10e. Overall, the resulting morphology is close to that produced assuming a constant slope. In both cases, the contour curvature within the side sectors is greater than in the central sector, which matches the feature of the surveyed contours. The main changes produced by letting the slope vary appear in the upstream canyon (contour spacing smaller) and near the fan toe (contour spacing slightly larger), where the simulated concave fan matches more closely the surveyed fan. The main discrepancy between the simulated and surveyed fans is that the simulation cannot capture local features on the fan surface like re-incised stream channels and margin deposition from side gullies.

doi:10.6342/NTU202204140

In Fig. 2.10d,f, we show maps of modeling error for the two simulations. Both reproduce well the elevation in the mid-fan area. The simulated constant slope fan shows larger simulation errors within the canyon and along the fan toe (Fig. 2.10d). At the price of an additional fitting parameter, the simulated concave fan reduces such errors (Fig. 2.10e). Nevertheless, both simulations show large errors where incision has altered the fan morphology. This drawback can also be seen as a useful tool, to identify incisional features on debris and alluvial fans. For instance, within the canyon and along the right margin, there is a deep active incisional channel, and along the left margin there is a small relict channel that is not obvious from the surveyed contour map (Fig. 2.10a). From the error maps (Fig. 2.10d,f), we can easily identify these channels by the large positive errors they produce (brown color). Along the left margin, there is also some local deposition from side gullies. On the error maps, we can identify these zone of additional local deposition by the negative simulation errors they produce (blue color). In Fig. 2.11c,f, finally, the simulated and surveyed fan elevations are compared along the three transects shown in plan on Fig. 2.10a. It can be seen that both simulations capture the convex shape of the transverse surveyed profiles. For all three transects, the simulated and surveyed profiles match well except along the margins, where local deposition and stream channel incision affect the fan morphology.

Secondly, we apply the algorithm to the Pu-Tun-Pu-Nas fan by the Laonong River to simulate a medium event in 2018. We have the topography data of the Pu-Tun-Pu-Nas fan in February 2018 and January 2019 (0.5m DEMs acquired by using UAV photogrammetry from (Tu, 2019)), which show an inactive fan surface on the west side of the fan and an enlarged terrace on the east side of the fan as the signature of at least one debris flow event. Since the aggraded fan was re-incised by the Laonong River and the stream flow over the fan, the information of the aggraded fan, such as fan area and deposition volume, is unknown. Therefore, we want to use the algorithm to reconstruct the aggraded fan to realize the possible aggradation

doi:10.6342/NTU202204140

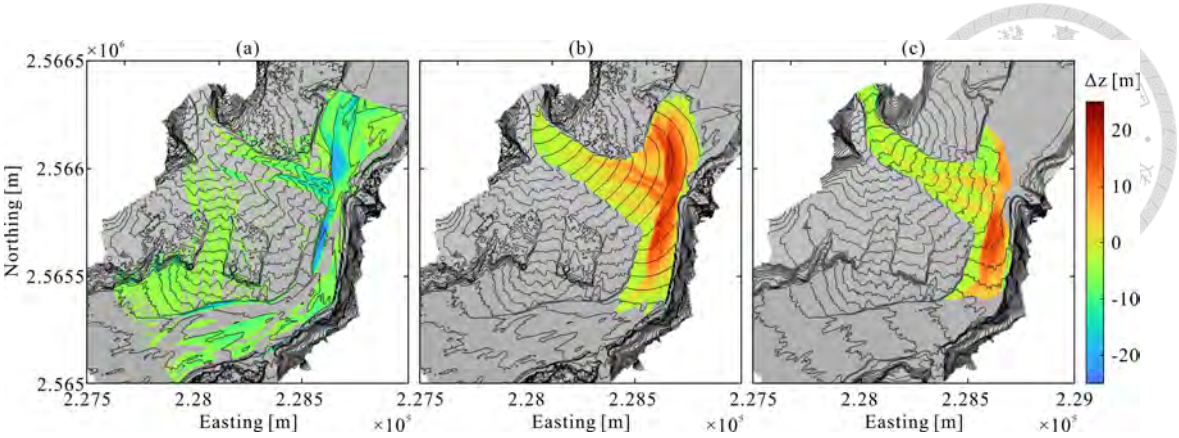

Figure 2.12: Simulation that reconstructs the incised Pu-Tun-Pu-Nas fan in 2018 summer. (a) Topography obtained by the minimal elevations of February 2018 and January 2019 as the initial condition of the simulation ($\Delta z = z_{201802} - z_0, z_0 = \min(z_{201802}, z_{201901})$). (b) Simulated fan topography. (c) Field topography in August 2018. Lines: elevation contours 5 m apart from each other.

morphology and estimate that information. Fortunately, we have another topography data of the Pu-Tun-Pu-Nas fan in August 2018 (1m DEM acquired by Airborne LiDAR, provided by C.-Y. Hung, NCHU), in which the Pu-Tun-Pu-Nas fan has been aggraded and suffered from less re-incision so that we are allowed to evaluate the simulated result.

We use the minimal elevations of the two DEMs (February 2018 and January 2019) to be the initial condition of the simulation (z_0), demonstrated in Fig. 2.12a, where colors present the depths removed from the topography in February 2018. We estimate the fan slope from the terrace on the DEM in January 2019. We assign an apex around the entrance of the tributary valley with an elevation higher than the initial fan surface since we do not have the topography data of the upstream tributary valley. We reconstruct the fan by using the algorithm and adjusting the location of the fan apex to let the simulated fan fit the stranded terrace in 2019. The result is demonstrated in Fig. 2.12b, where colors present the deposition depth.

Note that we can apply the algorithm to the topography data with various resolutions. See the next section for the effects of the topography data resolution on the simulation results. Here, we focus on the comparison between the simulation and field topographies so that we only present the result that simulated by applying the

doi:10.6342/NTU202204140

algorithm to the 5m DEM.

We identify the boundary of the active fan in August 2018 by satellite image (Source:the Geo-technical Team of CECI Engineering Consultants) and calculate the deposition depth within the region of the active fan (comparing to z_0). The result is presented in Fig. 2.12c. Comparing Fig. 2.12b,c, the simulation reconstructs the fan morphology before being re-incised. In the proximal region, the simulated fan elevation matches the high elevation in the region of the field observed fan, which represents the fan surface without perturbation of the stream flow from the tributary. In the distal region, the simulation captures the fan toe in the south. It explains why the contours curve around the corner of the terrace and are nearly parallel but not perpendicular to the radial direction of the entire fan. By contrast, the simulation does not match the field observation in the north. The simulated fan shows extensive aggradation upstream of the trunk river and completely blocks the river valley as it hits the opposite bank. By contrast, the field observed fan presents a downstream-skewed fan toe, which matches the observations by Giles et al. (2018); Leenman and Tunnicliffe (2020) in fields and Wu (2020) in laboratory experiments. According to Giles et al. (2018); Wu (2020), such fan morphology is attributed to the trunk river, which strongly erodes the distal fan upstream as it reaches the fan toe at a large angle and is deflected toward the opposite side of the river valley as a narrow channel. Nevertheless, we consider the fan volume calculated by using the simulated fan is acceptable for estimating the debris flow event magnitude.

We then apply the algorithm to a major aggradation episode experienced by the Pu-Tun-Pu-Nas fan from 2012 to 2013, and which involved debris flow diffluence and confluence around an island. Prior to 2012, only the eastern sector of the fan had been active in recent decades, and was entrenched relative to the ancient fan terraces. Debris flows through this sector supplied material to a single, wide deposit lobe at their confluence with the trunk river. In 2012, due to renewed aggradation of the eastern sector, almost up to terrace level, debris flows bifurcated to a relict channel

doi:10.6342/NTU202204140

on the west side of the fan. This avulsion caused the incision and widening of the relict channel, and the deposition of a new western lobe into the trunk river. Between the two sectors, a small portion of the ancient terrace remained. This formed an elevated island downstream of which the two lobes came into contact along a weld line. In 2013, several new debris flows caused both the eastern and western lobes to aggrade further, subject to continued diffluence and confluence around the island obstacle. To test the ability of our model to deal with such complex conditions, we aim to simulate the topography of the resulting deposits.

Because our model does not capture channel incision and bank erosion, we simulate deposition over a pre-incised topography, constructed as follows. First, a base topography is obtained as the minimum of two surveyed DEMs, acquired respectively before and after the episode in 2010 and 2018 (the latter courtesy of C.-Y. Hung, NCHU). Both have a resolution of 1 m and were acquired by airborne LiDAR. We then obtain a depressed DEM by subtracting 10 m from this topography over the active region of the fan. Finally, we backfill the depressed DEM up to the elevation of an inclined plane representing the trunk river bed, deduced from 3 data points of the 2018 survey. The resulting initial topography $z_0(x, y)$ is shown in Fig. 2.13a, with color used to represent the elevation difference Δz subtracted from the minimal elevation of the 2010 and 2018 DEMs. For this case, we only use the constant slope assumption to simulate the fan. For the fan slope $S = \tan\alpha$, we adopt a constant value of 0.10 m/m, approximating the slope of the western lobe based on the 2018 DEM. A single fan apex is assumed upstream of the tributary valley, at an elevation chosen to match the elevations of unreworked deposits again ascertained from the 2018 DEM.

Simulated results are shown in Fig. 2.13b, with contours used to represent the surface topography, and color to represent the deposit thickness. The algorithm is found to deal well with the complex topography. It produces a constant slope surface of complex morphology, that connects continuously with the assumed initial

doi:10.6342/NTU202204140

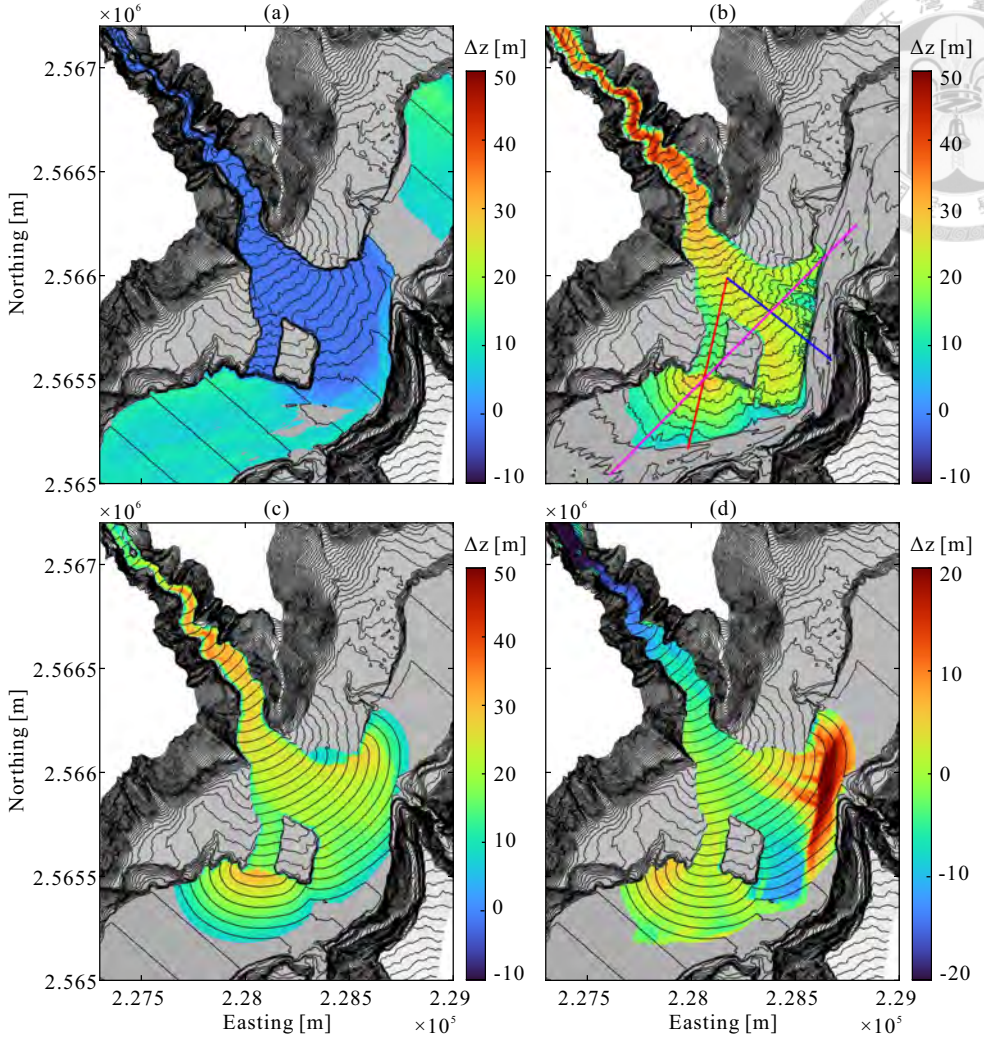

Figure 2.13: Application to a major aggradation episode experienced by the Pu-Tun-Pu-Nas debris fan from 2012 to 2013. (a) Depressed topography $z_0(x, y)$ (contours) used as initial condition for the simulation, and difference $\Delta z = z_0 - \min(z_{2010}, z_{2018})$ (color); (b) surveyed topography (contours) and deposit thickness (color) from 2014 survey; (c) simulated topography (contours) and deposit thickness (color); (d) simulated topography (contours) and elevation error $\Delta z = z - z_{2014}$ (color). Colored lines in (b): transects for the profiles shown in Fig. 2.14. Elevation contours spaced at intervals of 5 m.

topography along different types of boundaries: steep, highly irregular valley sides in the upstream canyon; previous deposits of nearly identical slope along the ancient side terraces; steep deposit faces around the elevated island; the river bed of milder inclination along deposit toes; and the steep opposite side of the valley, featuring an adverse slope over which the eastern lobe onlaps. In the upstream canyon, the algorithm has no problem dealing with the narrow, winding path of the canyon.

doi:10.6342/NTU202204140

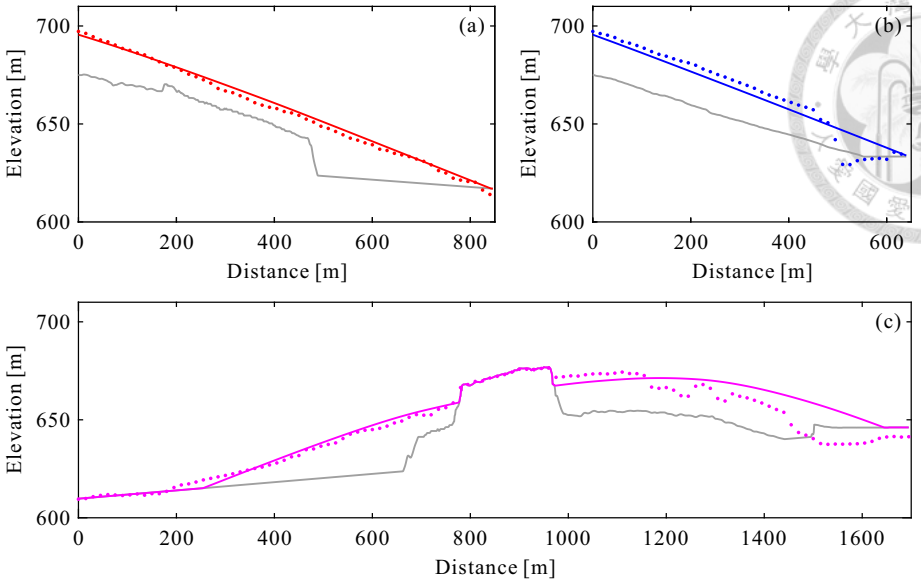

Figure 2.14: Transects of the Pu-Tun-Pu-Nas fan. (a) Long profile of the newly formed western lobe; (b) long profile of the pre-existing eastern lobe; (c) transverse profile across the fan complex. Gray lines: initial topography z_0, colored dots: surveyed profiles z_{2014}, colored lines: simulated profiles. The corresponding transects are indicated by red, blue, and magenta lines on Fig. 2.13b.

Along the eastern margin of the fan, the simulated contours connect nearly seamlessly with the surveyed contours of the ancient fan surface, dating from 160-300 years before present (Hsieh and Capart, 2013). This suggests that, in addition to simulating new deposits, the model could prove useful to interpret past deposits. Downstream of the central island, finally, the simulation resolves well the cusped weld line along which the eastern and western lobes come into contact. This shows that, even for complex conditions, the model can deal with deposit self-intersections as well as contacts with the pre-existing topography.

To check that the model can reproduce the actual fan topography due to the 2012-2013 aggradation episode, we compare the simulated results with an additional topographic survey (courtesy of the Taiwan Directorate General of Highways), not used to set up the simulation. This was acquired by Airborne LiDAR in January 2014, soon after the end of the episode. The corresponding topography and deposit thickness are shown in Fig. 2.13c. Over most of the fan surface and along the fan margins, excellent agreement is obtained, both for the topographic contours and for

doi:10.6342/NTU202204140

the deposit thickness. Nevertheless, the surveyed contours are again more irregular than the simulated ones. Some notable discrepancies, moreover, are observed upstream and downstream of the fan. In 2.13d, the simulation error is shown. It reveals that, in the upstream canyon, the deposit is steeper than our assumed fan slope. Along the downstream toe of the western lobe, conversely, the inclination is milder than assumed, and transitions gradually towards the inclination of the river bed rather than undergoing a sharp slope break as produced by the simulation. Downstream of the island, the surveyed weld line is located slightly westward of the simulated one. Along the toe of the eastern lobe, finally, the debris flow deposit has been trimmed by the trunk river, which re-incised a wide channel for itself. At various locations, the resulting scarp has also been downcutted by subsequent streamflow from the tributary.

To further compare the simulated and surveyed results, profiles along three selected transects are shown in Fig. 2.14. Two long profiles are taken along the centerlines of the western and eastern deposit lobes, and one transverse profile across the entire fan complex (see Fig. 2.13c for the transect locations). For each transect, we profile the initial topography z_0 (grey line), the simulated deposit surface (colored line), and the surveyed deposit surface z_{2014} (colored dots). For the long profile through the new western lobe (Fig. 2.14a), excellent agreement is observed between the simulated and surveyed results. Two factors contribute to this agreement: our choice of constant slope in the simulation, matching the surveyed inclination of the western lobe, and the absence of significant trimming by the trunk river along this lobe. For the long profile through the eastern lobe (Fig. 2.14b), agreement is reasonable but two differences can be noted. First, the surveyed inclination (approximately 0.08 m/m) is milder than the modelled inclination (0.10 m/m). As it assumes that the fan slope is either constant or dependent on height with respect to the apex, our model cannot account for such azimuthal variations between different sectors of the fan complex. Secondly, the toe of the surveyed deposit has been trimmed

doi:10.6342/NTU202204140

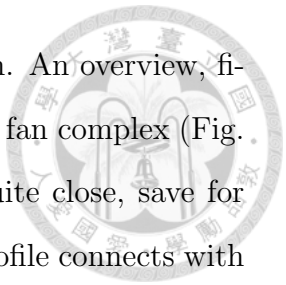

by the trunk river, an effect also not considered in the simulation. An overview, finally, is provided by the transverse profile across the width of the fan complex (Fig. 2.14c). To the left of the island (western lobe), agreement is quite close, save for the milder surveyed slope at the leftmost distal end, where the profile connects with the river bed. To the right of the island (eastern lobe), agreement is only partial. In the survey, local depressions occur where the fan surface has been re-incised by streamflow, and, at the rightmost end, the toe of the deposit was trimmed by the trunk river. Overall, in spite of the various approximations and discrepancies, good agreement is obtained between the simulated and surveyed results, demonstrating the applicability of our model to field cases.

2.5 Algorithm implementation and performance

We implemented our proposed method and its application to ideal and field cases in the Matlab environment. The corresponding scripts, functions and input data can be accessed from a digital repository (see Code availability section). The main function (Algorithm 1) initializes the simulation, and loops over the sorted dynamic list comprising the given apexes and the corner apexes generated during the process. To carry out the iterations, three subsidiary algorithms are needed: a visibility polygon algorithm, a contouring algorithm, and a point-in-polygon algorithm. For the visibility polygon algorithm, we implemented Algorithm 1. For contouring, we use the built-in algorithm provided in Matlab. To determine which points lie inside a given polygon, we use the point-in-polygon algorithm developed by Engwirda (Engwirda, 2020), and described in Kepner et al. (2020), which is about 100 times faster than the built-in point-in-polygon algorithm in Matlab. The contributions of these different algorithms to the computational cost depends on mesh resolution, as documented in Table 2.1.

For simulations on coarse meshes, the visibility polygon algorithm may account for nearly 20% of the computational cost, while the point-in-polygon algorithm only

doi:10.6342/NTU202204140

Table 2.1: Effect of mesh size on total CPU time and on the relative costs of the different sub-functions, for the field application of Fig. 2.13 involving a fan of area $A = 0.69$ km^2 and length $L = 800$ m.

d [m]	1	2	5	10	20	50
Contouring [%]	53.7	56.0	67.6	78.2	76.4	68.9
Point-in-polygon [%]	29.8	26.5	17.4	8.2	4.0	1.9
Visibility polygon [%]	8.4	9.6	9.0	9.3	13.4	18.1
Total CPU time [s]	7945	1235	101.3	19.57	5.523	1.709

takes about 2%. When refining the mesh, however, the computational cost of the visibility polygon algorithm increases less steeply than that of the point-in-polygon algorithm. For fine meshes, the visibility polygon algorithm accounts for only 8-9% of the computational cost, while the point-in-polygon algorithm accounts for nearly 30%. Regardless of mesh size, however, it is the contouring algorithm which incurs most of the computational cost. In addition, it is also the main source of error in fan morphology simulations, since it is responsible for the errors affecting the positions of child apexes. As a result, adopting or developing a faster and/or more accurate contouring algorithm would be a good target to improve the performance of our proposed method. This could possibly be done by specializing the contouring algorithm to the special problem encountered in our case, which is to find intersections between upright cones and a meshed topography.

To document the current performance of our method, Fig. C.1 shows how the root mean square error (RMSE) (top panels) and total CPU time (bottom panels) vary with mesh size for two different cases: an ideal case (left panels), the fan in faceted valley of Fig. 2.5 c, and a field case (right panels), the Pu-Tun-Pu-Nas fan complex of Fig. 2.13 . For the ideal case, we calculate the RMSE from the difference between the analytical and simulated fan elevation over the fan domain, normalized by the average deposit depth. For the field case, there is no analytical solution, so we calculate the RMSE from the difference in elevation between each simulated fan and a reference simulation conducted at the smallest mesh size (1 m).

doi:10.6342/NTU202204140

Table 2.2: Comparison of modeling error and computational errors for different mesh sizes, for the different field profiles shown in Fig. 2.13 d-f.

RMS of [m]	$z_1 - z_{field}$	$z_2 - z_1$	$z_5 - z_1$	$z_{10} - z_1$	$z_{20} - z_1$	$z_{50} - z_1$
Long profile (eastern lobe)	6.865	0.007	0.058	0.059	0.243	0.717
Long profile (western lobe)	2.540	0.034	0.061	0.055	0.258	0.467
Transverse profile	4.732	0.082	0.173	0.446	0.915	1.494

All simulations are run with an i5-9500 intel processor, and the results are plotted against the mesh size d, normalized by the fan length L. This is measured from the tributary valley mouth and is approximately 800 m for the field case. As seen from the figure, the simulation accuracy and efficiency are impacted by the mesh size in much the same way for both cases, except that the order of magnitude of the errors and CPU times are much greater for the field case, due to the rugged topography which produces a large number of corner apexes. In both cases, refining the mesh leads to an approximately first-order error convergence. Reducing the mesh size causes a mild increase in CPU time for coarse meshes, and a steeper increase for fine meshes. This implies a non-uniform trade-off between accuracy and efficiency. For the same marginal increase in accuracy, fine meshes incur greater computational costs since they require the generation and processing of a large number of apexes.

In practice, adopting a fine mesh may not be needed, and a relatively coarse mesh may be sufficient to resolve the features of interest. For field cases, in particular, other sources of error involving say the constant slope approximation limits the gain in accuracy that can be achieved by reducing the mesh size. This is shown in Table 2.2, which lists the modeling and computational errors affecting the three profiles shown in Fig. 2.13 d-f. For each profile, the modeling error is estimated from the difference between the simulation on the finest mesh and the survey measurements, while the computational error is estimated as before from the difference between simulation results for different mesh sizes and the simulation on the finest mesh. Even for relatively coarse mesh sizes of, say, 10 m, the computational error is already

doi:10.6342/NTU202204140

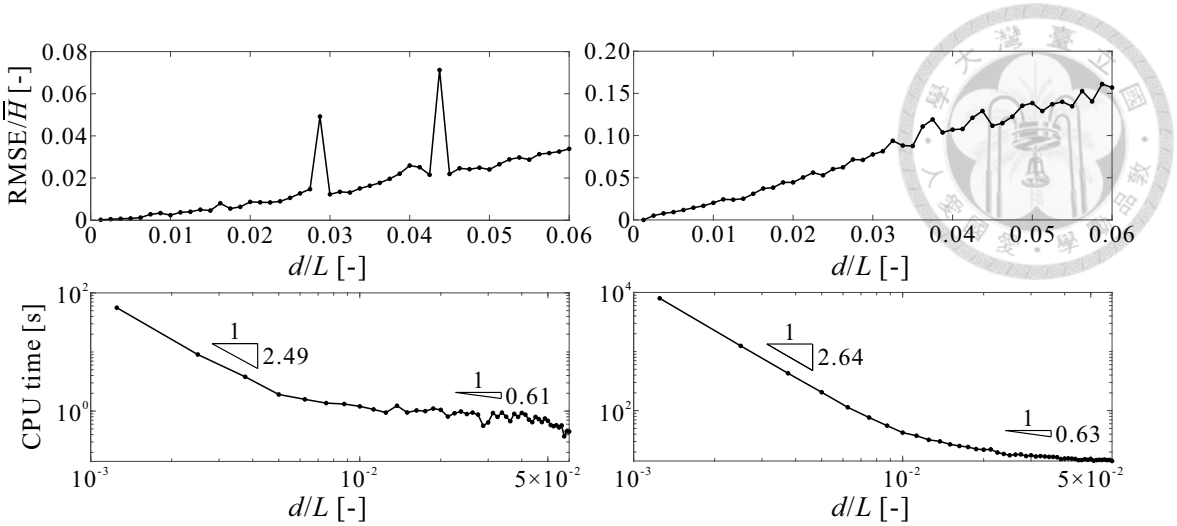

Figure 2.15: Effect of mesh resolution on simulation accuracy and computational cost. Top panels: RMSE for the fan elevation, normalized by the average depth. Bottom: CPU time. Left panels; results for an idealized case (Fig. 2.5 c); right: results for a field case (Fig. 2.13).

much smaller than the modeling error. Nevertheless, finer meshes may be useful to resolve more sharply some morphological features of special interest, like the weld lines formed where different lobes come into contact.

2.6 Conclusion

In the present work, we proposed a new computational method to predict the morphology of debris and alluvial fans on irregular terrain. The method is based on identifying, using the visibility polygon, the sector reachable from a certain apex by straight paths, and the new corner apexes needed to access occluded regions. By iterating over a sorted list of given and newly generated apexes, the method can reconstruct complex fan surfaces. To validate the method, we tested it on idealized cases for which analytical solutions can be derived, including fans on faceted topography, fans on curved topography, and coalescing fans. The method was then applied to field cases, on highly irregular ground topography derived from surveyed digital elevation models (DEMs). In both simple and complex conditions, the method was shown to produce accurate fan surfaces. Where fans come into contact with the

doi:10.6342/NTU202204140

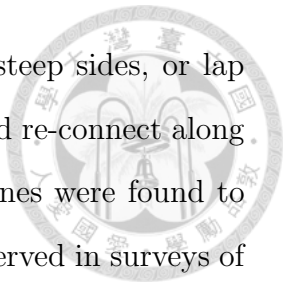

pre-existing topography, they may either abut or bend around steep sides, or lap onto flatter ground. They may also bifurcate around obstacles and re-connect along weld lines. The resulting fan surfaces, margins, toes and weld lines were found to match well those derived from analytical solutions, and those observed in surveys of actual fan deposits, before they are reworked by water flow.

In its current implementation, our proposed method is suitable for various different applications. Applied prospectively, it can help assess the possible extent of future fan aggradation, and the corresponding risks to communities and infrastructure. Applied retrospectively, it can help reconstruct the maximal aggradation surface and deposit volume produced by a debris flow event, correcting for subsequent debris removal by streamflow incision or trunk river trimming. Going back further in time, the method can also help interpret the preserved fan terraces that record ancient debris flow episodes. Other possible applications would require extensions to the model. To simulate long term fan evolution, both supply and removal of debris would need to be modelled (Leenman and Tunnicliffe, 2020). By turning the model upside down, the method could be applied to constant slope incisional landforms, like the networks of V-shaped valleys formed in certain subaerial and submarine environments (Hasbargen and Paola, 2000; Lai et al., 2016). Extension from stationary point apexes to moving line sources, finally, would allow the model to deal with applications like prograding deltaic shorelines (Ke and Capart, 2015; Zhao et al., 2019), or migrating valley thalwegs (Hasbargen and Paola, 2000). These extensions are suggested as avenues for future work.

Code availability

The Matlab code for the visibility polygon and fan morphology algorithms, scripts for comparing with analytical solutions, and input data for the field cases are available from the digital repository Zenodo via https://doi.org/10.5281/zenodo.7004397.

doi:10.6342/NTU202204140

Chapter 3

A control volume finite element model for predicting the morphology of cohesive-frictional debris flow deposits

To predict the morphology of debris flow deposits, a control volume finite element model (CVFEM) is proposed, balancing material fluxes over irregular control volumes. Locally, the magnitude of these fluxes is taken proportional to the difference between the surface slope and a critical slope, dependent on the thickness of the flow layer. For the critical slope, a Mohr–Coulomb (cohesive-frictional) constitutive relation is assumed, combining a yield stress with a friction angle. To verify the proposed framework, the CVFEM numerical algorithm is first applied to idealized geometries, for which analytical solutions are available. The Mohr–Coulomb constitutive relation is then checked against debris flow deposit profiles measured in the field. Finally, CVFEM simulations are compared with laboratory experiments for various complex geometries, including canyon-plain and canyon-valley transitions. The results demonstrate the capability of the proposed model and clarify the influence of friction angle and yield stress on deposit morphology. Features shared by the field, laboratory, and simulation results include the formation of steep snouts along lobe margins.

Submitted manuscript: Chen, T. Y. K., Wu, Y. C., Hung, C. Y., Capart, H., and Voller, V. R.. A control volume finite element model for predicting the morphology of cohesive-frictional debris flow deposits, *Earth Surf.* Dynam. [preprint], https://doi.org/10.5194/esurf-2022-11. (Under review).

doi:10.6342/NTU202204140

3.1 Introduction

When they transition from steep gullies to milder topography, debris flows typically spread out and slow down to form fresh deposits. By burying houses, bridges, or other assets, these may cause considerable damage to communities and infrastructure (Liu and Huang, 2006; Scheidl et al., 2008; Tai et al., 2019). This is illustrated in Fig. 3.1 for a case in Taiwan (courtesy of the Chi Po-lin Foundation, 2009), where debris flow deposition near a gully mouth buried the lower stories of multiple buildings. To mitigate debris flow hazards, it is therefore important to anticipate the possible extent and thickness of their deposits.

To simulate the flow and deposition of debris flows, many highly resolved models have been proposed. These typically apply mass and momentum balance equations to flows over non-erodible (O'Brien et al., 1993; O'Brien, 2006; Liu and Huang, 2006; Murillo and García-Navarro, 2012; Pudasaini, 2012; Kowalski and McElwaine, 2013; Gregoretti et al., 2016; Meng and Wang, 2016; Tai et al., 2019; Pudasaini and Fischer, 2020) or erodible substrates (Armanini et al., 2009; Bartelt et al., 2017). Such simulations, however, require detailed hydrological input data and various rheological parameters which may be difficult to obtain, and may also differ dramatically from one case to another. In this context, it is worth exploring whether reduced complexity models could predict key features of debris flow deposits with less computational effort and more limited data requirements.

A class of reduced complexity models developed for fluvial problems rests on defining a constitutive model for the mass flux, which in turn can be used with a mass balance equation (e.g., the Exner equation) to evolve the bed surface elevation. For applications to alluvial fans and river deltas, for instance, some models have been proposed that simply set the mass flux proportional to the current slope at that point (Voller and Paola, 2010; Lorenzo-Trueba and Voller, 2010; Lorenzo-Trueba et al., 2013). More sophisticated approaches employ the device of a critical threshold

doi:10.6342/NTU202204140

Figure 3.1: Aerial view of the debris flow deposit formed at Xinfa, Southern Taiwan, during Typhoon Morakot in August 2009 (Photograph by Chi Po-lin. Provided by Chi Po-lin Foundation © Above Taiwan Cinema, Inc.)

(Mitchell, 2006; Lai and Capart, 2007), whereby sediment transport occurs only when the bed inclination exceeds a critical slope (Lai and Capart, 2007; Hsu and Capart, 2008; Lai and Capart, 2009). In these models, the critical slope for the fluvial sediment flux can be derived by considering the friction stress at the sediment-water

doi:10.6342/NTU202204140

interface (the Shields stress). In some sense, this idea of a critical slope is analogous to the angle of repose governing the shapes of dry sand piles (Kuster and Gremaud, 2006; Giudice et al., 2019).

Mass flux models have also been used to model mud flows. In particular, we refer to the work of Yuhi and Mei (2004) where a flux law was obtained by combining lubrication theory with a cohesive yield stress criteria. Predictions from this model were verified by comparing with analytical solutions which constrain the slope of the deposit, in axi-symmetric domains, based on a cohesive yield stress criteria (Coussot et al., 1996; Yuhi and Mei, 2004). Unlike what might be seen in a sand pile or fluvial system close to the threshold, here the slope at a point varies with the thickness of the deposit.

Contrasting with fluvial and mud flows, for debris flows it is believed that both friction angle and yield stress can affect the morphology of deposits (O'Brien et al., 1993; Mangeney et al., 2010; Murillo and García-Navarro, 2012; Pudasaini, 2012; Gregoretti et al., 2016; Tai et al., 2019; Pudasaini and Fischer, 2020). The study of Coussot et al. (1996) emphasizes this point. Using only a yield stress criterion, these authors derived solutions for deposit profiles which they compared with surveyed debris flow transects. This model was found to work well for cohesive debris flow deposits with high clay content. For lower clay content, however, deposit inclinations are more consistent with control by the saturated angle of friction (Takahashi, 1991). For debris deposits mixing coarse and fine material, therefore, it appears necessary to consider both a yield stress and a saturated friction angle, as in the well-known Mohr–Coulomb model for cohesive-frictional materials.

The objective of the current work is 3-fold, first, we will develop a mass flux expression that considers both friction angle and yield stress in setting the critical slope. Secondly, we will use this mass flux in an unstructured control volume finite element method (CVFEM) solution of the Exner mass balance equation to arrive at, for a given input mass, predictions of the final deposit location and shape.

doi:10.6342/NTU202204140

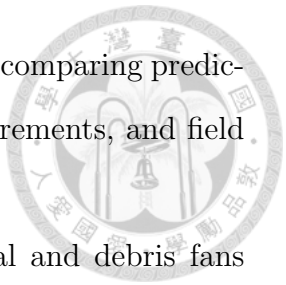

Finally, we will assess the predictive performance of this model by comparing predictions with available closed-form expressions, experimental measurements, and field observations.

In line with our objectives, we note that, in general, alluvial and debris fans build up over time in more complex ways than those immediately addressed by our proposed model and experiments. For example, channel formation, migration, and avulsion are expected to significantly affect fan evolution, especially for large scale debris flow fans. For alluvial fan experiments devoted to these processes, the reader is referred to Le Hooke and Rohrer (1979), Whipple et al. (1998), Delorme et al. (2018), and Savi et al. (2020). Our focus here, however, is on the formation of fresh deposits, possibly over a pre-existing fan surface, by unchannelized debris flows. For such conditions, illustrated by Fig. 3.1, we hope to formulate and verify a simplified model that could later be extended to more general conditions.

The chapter is structured as follows. Section 2 presents the governing equations that form the core of our model. The CVFEM algorithm developed to obtain numerical solutions is then described in Sect. 3. Section 4 describes how we incorporate a Mohr–Coulomb constitutive relation into this framework. In Sect. 5, we explain how to supplement our CVFEM with a flux limiter, to model flow over non-erodible surfaces. In Sect. 6, we check simulations against available analytical solutions. In Sect. 7, we verify our model by comparing results with field data and laboratory experiments. In Sect. 8, finally, we discuss the contribution and limitations of our work, emphasizing how our model can help understand the influence of material properties on the morphology of debris flow deposits.

3.2 Governing equations

To write governing equations, we consider a debris mixture depositing over a fixed substrate of arbitrary topography. An example is shown in Fig. 3.2a: supplied upstream of a steep triangular channel, the mixture flows into a trapezoidal channel

doi:10.6342/NTU202204140

of mild inclination, where it spreads out and slows to a complete stop. We denote by $\tilde{z}(x, y, t)$ the time-varying surface elevation during flow, and by $z_b(x, y)$ the underlying bed topography. The corresponding profiles are shown on Fig. 3.2b on a schematic section.

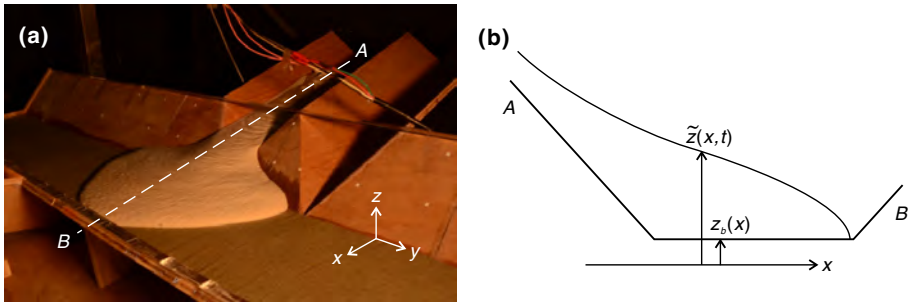

Figure 3.2: Deposition of a cohesive-frictional material over a substrate of known geometry. (a) Experimental case featuring a symmetric deposit; (b) Schematic section along the deposit centerline.

To capture the deposition process and predict the final deposit morphology, we express mass conservation by the Exner equation (Exner, 1920, 1925)

$$\frac{\partial \tilde{z}}{\partial t} = -\nabla \cdot \mathbf{q} + \delta(\mathbf{x_s}) \left(\frac{\partial z}{\partial t} \right)_s , \tag{3.1}$$

where $\mathbf{q} = (q_x, q_y)$ is the volumetric flux (volume transferred per unit width and time), $\nabla \cdot \mathbf{q}$ with $\nabla = (\partial/\partial x, \partial/\partial y)$ is the divergence of this flux, δ is the Dirac delta function, $\mathbf{x_s} = (x_s, y_s)$ is the location of the source, and $(\partial z/\partial t)_s$ is the elevation change rate due to the source. For simplicity, we assume that the flow is sufficiently slow to be regarded as quasi-static, allowing inertia effects to be neglected. At each location (x, y), the flux $\mathbf{q}$ is assumed aligned with the direction of steepest descent according to

$$\mathbf{q} = -\nu \nabla \tilde{z} \, . \tag{3.2}$$

The diffusivity ν, however, is not assumed constant but instead depends on the local

doi:10.6342/NTU202204140

surface slope $||\nabla\tilde{z}||$ according to the formula

$$\nu = \nu^* \max\left(\frac{||\nabla\tilde{z}|| - S_c}{||\nabla\tilde{z}||}, 0\right). \tag{3.3}$$

where ν^* is a real and positive constant, and S_c a critical slope dependent on material properties and on the local instantaneous thickness of the flow layer, this dependence of S_c is derived in section 4. As in the model proposed by Lai and Capart (2007, 2009), fluxes are only non-zero when the local slope $||\nabla\tilde{z}||$ exceeds this critical slope S_c. Combining Eq. (3.1), (3.2) and (3.3), we see that we obtain a non-linear diffusion process with a diffusivity ν that depends on the difference between the magnitude of the local gradient and the critical slope S_c. When the flow slows to a complete stop, the flux $\mathbf{q}$ vanishes which implies that, everywhere along the deposit surface,

$$||\nabla\tilde{z}|| \leq S_c\,. \tag{3.4}$$

To incorporate the above flux definition in an Exner balance, our model includes three main components. First, we need a numerical method to solve the governing mass balance equation with the proposed flux model. Second, we need to derive an appropriate expression for the critical slope—in doing this we will consider both a friction angle and a yield stress. Third, we need to provide a limiter in our evolution algorithm to avoid fluxing out from a control volume more than the amount of material available.

3.3 Numerical method

To solve the Exner equation as formulated above, we adopt the control volume finite element method (CVFEM), a method first proposed by Winslow (1966) and later extended by Baliga and Patankar (1980, 1983), Voller (2009) and Tombarevic et al. (2013). The CVFEM is a useful tool for this application because it couples the finite

doi:10.6342/NTU202204140

element flexibility of fitting the domain geometry with the explicit mass balance of the control volume.

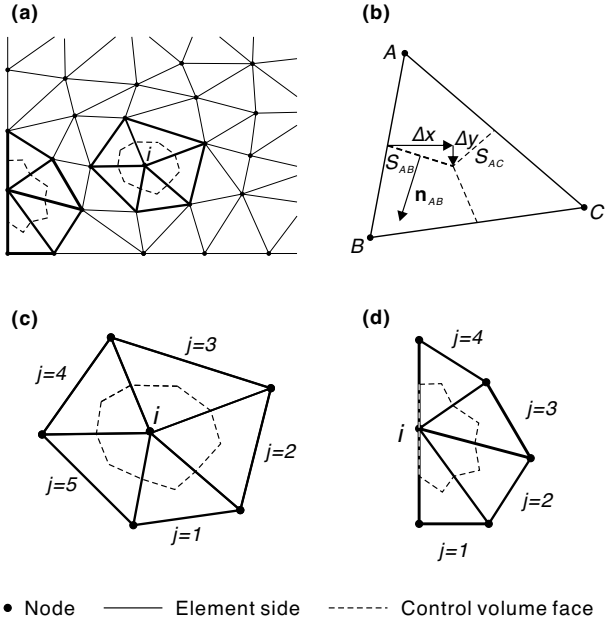

Figure 3.3: Global and local mesh geometry: (a) The discretized domain and elements; (b) a triangular element divided by the segments connecting the centroid and the midpoint of each side; (c) the control volume and the region of support of an internal node; (d) those of a node on the boundary.

The application of the CVFEM to model debris flow deposits over an existing topography starts by identifying a 2-D planar problem domain (x, y) and then covering this domain with a mesh of connected, non-overlapping, plane geometric elements. In our case, we use a rectangular domain and cover it with an unstructured mesh of linear triangle elements (Fig. 3.3a). Each triangular element is associated with three vertex node points (locally labeled A, B, and C) (Fig. 3.3b). This will result in $i = 1, 2, \ldots N$ node points in the domain, each storing values for the fixed bed substrate elevations $z_b(x, y)$, assumed given, and for the time-dependent flow surface elevations $\tilde{z}(x, y, t)$, to be determined. To evaluate the values of z_b and $\tilde{z}$ at internal points in an element we use the classic finite-element interpolation based on linear shape functions. In this way, at a point (x, y) in a given element we approximate

doi:10.6342/NTU202204140

the bed substrate elevation as

$$z_b(x,y) = n_A(x,y)z_{b_A} + n_B(x,y)z_{b_B} + n_C(x,y)z_{b_C} \tag{3.5}$$

and the flow surface elevation as

$$\tilde{z}(x,y,t) = n_A(x,y)\tilde{z}_A(t) + n_B(x,y)\tilde{z}_B(t) + n_C(x,y)\tilde{z}_C(t)\,, \tag{3.6}$$

where the shape functions, n_A, n_B and n_C, linear functions in x and y, take a unit value at nodes A, B and C respectively and vanish along the element sides opposite the labeled node, i.e, sides $B-C$, $C-A$, and $A-B$ respectively. Thus, the CVFEM discretization provides piece-wise linear approximations of the bed substrate and flow surfaces. In particular, we note that in any element j in our domain we can readily approximate the surface gradient by

$$\nabla\tilde{z}_j = \left(n_{A_x}\tilde{z}_A + n_{B_x}\tilde{z}_B + n_{C_x}\tilde{z}_C, n_{A_y}\tilde{z}_A + n_{B_y}\tilde{z}_B + n_{C_y}\tilde{z}_C\right)\,, \tag{3.7}$$

where, n_{A_x}, n_{A_y} etc are the derivatives of the shape functions. Due to the linear nature of the shape functions, we note this approximation renders a constant value for the slope in each element.

To move on, we construct an additional geometric element on our grid of triangular elements. We join the midpoint of each element side to the centroid of each element, generating a set of connected non-overlapping control volumes around each node i in the domain, see Fig. 3.3c,d. Thus the control volume around node i has $j = 1, 2, \ldots m$ elements connected to it (the region of support), and each of these elements contains two faces of the control volume. To discretize our governing equation, Eq. (3.1), we integrate the equation over the control volume, use the divergence theorem, and make an explicit finite difference approximation in time to arrive at a

doi:10.6342/NTU202204140

discrete equation for the surface elevation at each node point and time step,

$$\frac{\tilde{z}_i^{\text{new}} - \tilde{z}_i}{\Delta t} = -\frac{1}{A_{CV,i}} \sum_{j=1}^{m} Q_j + \frac{Q_{\text{in},i}}{A_{CV,i}}\,, \tag{3.8}$$

where $A_{CV,i}$ is the area of the control volume and

$$Q_j = \int_{S_{AB}+S_{AC}} \mathbf{q}_j \cdot \hat{\mathbf{n}}\, ds \tag{3.9}$$

is the net discharge out of the control volume across the two faces in element j, e.g., sides S_{AB} and S_{AC} in Fig. 3.3b, and $Q_{\text{in},i}$ accounts for source node points where material is added to the domain.

With an appropriate constitutive equation for determining the critical slope–see discussion below–we can use our approximations for the deposit slope in the element, Eq. (3.7) to, through Eq. (3.2), arrive at an approximation for the flux $\mathbf{q}_j = (q_{x_j}, q_{y_j})$ in element j; we should expect this value to be constant over the element. Further, if we use Δx and Δy to express the change in the x and y values along a face as we move counter-clockwise around node i (see Fig. 3.3b), we can express the constant outward normal on a face with length ℓ as $\mathbf{n} = (\Delta y/\ell, -\Delta x/\ell)$. This provides us enough information to fully approximate the discharge in Eq. (3.9) in terms of the current nodal values of $\tilde{z}_i$ in the element (for full details refer to Voller (2009)). On making this approximation for each element in the support of node i and rearranging Eq. (3.8) we arrive at the following update for the surface elevation:

$$\tilde{z}_i^{\text{new}} = \tilde{z}_i - \frac{\Delta t}{A_{CV,i}} \left(\sum_{j=1}^{m} Q_j - Q_{\text{in},i} \right)\,. \tag{3.10}$$

We note that when a node i is on the domain boundary, see Fig. 3.3d, we set the discharge across the control volume faces that coincide with the boundary to zero. Hence Eq. (3.10) provides us with an explicit means of updating the nodal values

doi:10.6342/NTU202204140

of the surface elevation at time $t + \Delta t$ from the known values at time t.

To insure the numerical stability, we use time step $\Delta t = 0.2\Delta\ell^2/(\nu^* \max((\nabla\tilde{z}_{ele} - Sc_{ele})/(\nabla\tilde{z}_{ele}))$, where subscript $_{ele}$ represents values at elements, and $\Delta\ell$ is the average element size. For time step where $\max((\nabla\tilde{z}_{ele} - Sc_{ele})/(\nabla\tilde{z}_{ele}) \leq 0$, we use $\Delta t = 0.25\Delta\ell^2/\nu^*$. Provided that the diffusivity coefficient ν^* should be sufficiently large to fast diffuse materials from the elements whose slopes exceed the critical slopes to surrounding elements, we chose $\nu^* = 100\max(Q_{in})$.

3.4 Critical slope

In the previous sections, we assumed that flow occurs when the surface slope exceeds a critical slope, or, upon assuming that the direction of steepest descent coincides with the x-axis

$$\left|\frac{\partial\tilde{z}}{\partial x}\right| > S_c\,, \tag{3.11}$$

To set this critical slope, we adopt a Mohr–Coulomb failure criterion. For flow to occur, the shear stress τ at the base must then satisfy

$$\tau > \sigma\tan\phi + \tau_Y\,, \tag{3.12}$$

where σ is the normal stress, ϕ is the saturated friction angle dependent on the solid fraction, the void fraction, and the fine content in the fluid (Takahashi, 1991), and τ_Y is the yield stress. When the deposit surface slope is less than or equal to the critical slope (i.e., $|\partial\tilde{z}/\partial x| \leq S_c$), the mixture remains in static equilibrium, with $\tau \leq \sigma\tan\phi + \tau_Y$. In the limiting state, we can therefore use a force balance to derive an expression for the critical slope.

In the CVFEM model, we express this force balance element by element under the following two simplifying assumptions: (i) the surface slope in an element is uniform

doi:10.6342/NTU202204140

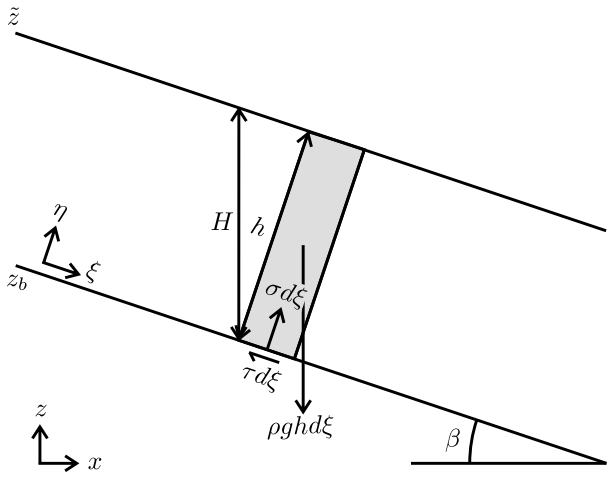

Figure 3.4: Force balance of a small piece of material on a fixed bed whose local gradient has a value equal to $\tan\beta$ and direction pointing towards ξ.

(a direct consequence of our choice of linear elements); (ii) the flow thickness in an element is also uniform. This latter restriction is needed to keep expressions simple, but will still allow us to apply the model to flows of variable thickness. Under these assumptions, we can simply consider a 2-dimensional force balance in the (ξ, η) coordinate system aligned with the surface inclination, as illustrated in Fig. 3.4. Force balance in the normal and tangential directions can then be expressed as

$$\sigma d\xi = \rho g h \cos\beta \, d\xi \,, \quad \tau d\xi = \rho g h \sin\beta \, d\xi \,, \tag{3.13}$$

where ρ is the density of the mixture, g the gravitational acceleration, h the oblique layer thickness in the η direction, and β the bed inclination angle. To move forward, we note, by our assumptions, that

$$\frac{\partial \tilde{z}}{\partial x} = \tan\beta \,. \tag{3.14}$$

and that the vertical and oblique thicknesses are related by

$$H = \frac{h}{\cos\beta} \,. \tag{3.15}$$

doi:10.6342/NTU202204140

Thus, on substituting Eq. (3.14) and (3.15) into the force balance relations, Eq. (3.13), we obtain the following expression for the shear stress

$$\tau = \rho g h \sin\beta = -\rho g H \frac{\partial \tilde{z}}{\partial x} \,. \tag{3.16}$$

an expression that matches the derivation made by Yuhi and Mei (2004). Finally, on substituting this shear stress into the Mohr–Coulomb criterion, we arrive at a model for the critical slope

$$S_c = \left| \frac{\partial \tilde{z}}{\partial x} \right|_{\max} \approx \frac{\tau}{\rho g H} \approx \tan\phi + \frac{\tau_Y}{\rho g H} \,. \tag{3.17}$$

The critical slope in each element can therefore be determined by setting values for the saturated friction angle and yield stress, taking into account the local vertical layer depth $H = \tilde{z} - z_b$. What distinguishes our expression from previous suggestions for the critical slope Liu and Mei (1989), Coussot et al. (1996) and Yuhi and Mei (2004) is the appearance of the friction angle in addition to the yield stress.

3.5 Flux limiter

In our CVFEM model, we assume a non-eroding bed substrate. This will require the use of a "flux limiter" to ensure mass conservation in an element over each time step of the calculation. Over a time step, we cannot flux out more material than what is available at the beginning of the time step.

With reference to the selected element in Fig. 3.3b, we note that one-third of the element area A_{ABC} contributes to the control volume around node A and thus, at the start of a time step, the material available for fluxing from this sub-section of the control volume will be $\frac{1}{3}(\tilde{z}_A - z_{bA})A_{ABC}$. In this way, over a time step Δt, the maximum discharge that can be fluxed out from this section, contributing to

doi:10.6342/NTU202204140

the inflows to nodes B and C, is given by

$$Q_{\max,A} = \frac{\tilde{z}_A - z_{bA}}{\Delta t} \frac{A_{ABC}}{3} \tag{3.18}$$

From this, following the time step calculation of the flux Q_A across faces S_{AB} and S_{AC}, we can provide a limiter by setting

$$Q_A = C_A Q_A \tag{3.19}$$

where the limiting factor ≤ 1 is calculated as

$$C_A = \begin{cases} Q_{\max,A}/Q_A, & \text{if } Q_A > Q_{\max,A} \\ 1\,, & \text{otherwise.} \end{cases} \tag{3.20}$$

Similar limiters must likewise be applied to the outflows from nodes B and C. In practice, to ensure that fluxes balance out, we apply a single value of the limiting factor

$$C = \min(C_A, C_B, C_C) \tag{3.21}$$

to each element in the solution domain.

3.6 Analytical solutions

As the flow spreads and slows, it will eventually come to a complete stop and freeze in place. At each point of the resulting deposit, the limit equilibrium condition, Eq. (3.4), will then be satisfied. If, say because of symmetry, the surface gradient along a certain transect is everywhere aligned with this transect, then the surface profile

doi:10.6342/NTU202204140

will satisfy the simpler equation

$$\frac{\partial \tilde{z}}{\partial x} = \pm S_c = \pm \tan\phi \pm \frac{\tau_Y}{\rho g H}\,, \tag{3.22}$$

with coordinate x taken along the transect direction. In this expression, the plus operators denote downhill deposition ($\tilde{z}$ and z_b decreasing in the same direction), and the minus operators denote uphill deposition ($\tilde{z}$ and z_b decreasing in opposite directions). Substituting $\tilde{z} = z_b + H$, the equation becomes an ODE for the deposit thickness

$$\frac{\partial H}{\partial x} = -\frac{\partial z_b}{\partial x} + \frac{\partial \tilde{z}}{\partial x} = -\tan\beta \pm \tan\phi \pm \frac{\tau_Y}{\rho g H}\,. \tag{3.23}$$

For the special case in which the bed slope $\partial z_b/\partial x = \tan\beta$ is constant, Eq. (3.23) becomes a first-order autonomous ODE that can be integrated analytically. In implicit form, the resulting depth profile $H(x)$ is given by

$$x - x_0 = \begin{cases} (H(x) - H(x_0))/A & \text{if } B = 0, \\ (H(x)^2 - H(x_0)^2)/(2B) & \text{if } A = 0, \\ (AH(x) - B\ln(|AH(x) + B|))/A^2 - C & \text{otherwise,} \end{cases} \tag{3.24}$$

where

$$A = -\tan\beta \pm \tan\phi, \quad B = \pm\frac{\tau_Y}{\rho g}, \quad C = \frac{AH(x_0) - B\ln(|AH(x_0) + B|)}{A^2}\,. \tag{3.25}$$

In the above expressions, $H(x_0)$ is the boundary condition at x_0, which can be any point within the depositing region. Note that A will be zero for frictionless material deposits on a horizontal plane, or frictional materials depositing downhill when the friction slope equals the bed slope, and B will be zero when there is no yield stress. In what follows, these analytical solutions will be used for three purposes: clarify model properties, verify the numerical method, and calibrate material parameters

doi:10.6342/NTU202204140

when comparing model results with field and laboratory data.

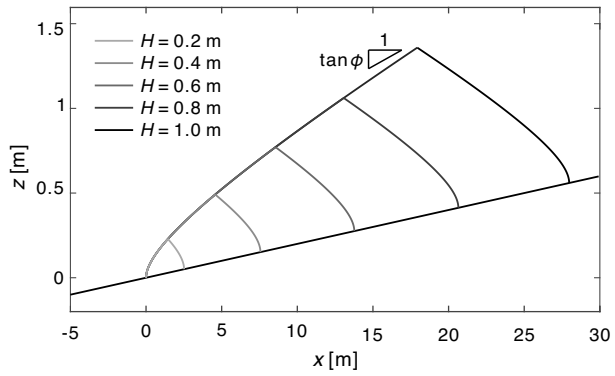

Figure 3.5: Analytical solutions for the centerline profiles of cohesive-frictional deposits on an inclined plane of slope $\tan\beta = 0.02$, for different deposit heights, assuming identical material properties $\tan\phi = 0.05$, $\tau_Y/(\rho g) = 0.01$ m.

As an example, analytical solutions for the centerline profiles of cohesive-frictional deposits over an inclined plane are illustrated in Fig. 3.5. For each case with different deposit heights H, we supply material at a single point corresponding to the apex of each deposit, whose location x_s follows the function $x_s = (AH - B\ln(|AH + B|))/A^2 - C$, where $A = -\tan\beta + \tan\phi$, $B = \tau_Y/(\rho g)$, $C = (-B\ln(B))/A^2$. In all cases, the material properties are the same, and the origin is taken at the downstream end of each deposit. This representation is chosen to highlight two important features of the solutions. First, the shape of the deposit toe does not change with the size of the deposit, and depends only on the bed slope and material properties. Secondly, the different material properties affect separate features of the profiles. The yield stress τ_Y controls the scale of the steep snouts, where the deposit thickness reaches zero, whereas the friction slope $\tan\phi$ sets the deposit inclination far away from the snouts, where the deposit thickness becomes large.

It follows from these properties that a single profile of sufficient length through the toe of a deposit is sufficient to calibrate the material properties of the model. This is very useful as it greatly facilitates model application to field and experimental cases. A second implication is that, for deposits of large size compared to the scale

doi:10.6342/NTU202204140

of the snouts, deposit shapes may be well approximated by surfaces of constant slope. For the deposits of Fig. 3.5, setting the yield stress to zero would produce upright cones of slope $\tan\phi$ centred at the apex of each deposit. In general, however, the morphology of deposits will be affected by both the yield stress and the friction angle.

3.7 Numerical model evaluation

In this section, we evaluate the CVFEM numerical model by comparing results with analytical solutions. This provides an opportunity to show how model results depend on material parameters, for some additional simple cases. We also examine how mesh geometry and size affect the accuracy and performance of the model.

3.7.1 Comparison with analytical solutions

To verify our CVFEM algorithm we consider deposits formed by supplying material from a point source onto three idealized geometries: (i) a horizontal plane, (ii) an axisymmetric conical basin of slope $\tan\beta = 0.05$, and (iii) an inclined plane of constant slope ($\tan\beta = 0.02$). The CVFEM model for each of these cases operates in Cartesian coordinates and will produce 3D deposit shapes. Thus, to compare with analytical solution profiles we need to select appropriate transects. For the horizontal plane and conical basin cases, we examine radial profiles (see Fig. 3.6a,b,e,f,i,j). For the inclined plane, we select two profiles through the source point: a longitudinal profile in the direction of the base slope, and a transverse profile orthogonal to this direction (see Fig. 3.6c,d,g,h,k,l). For the longitudinal profile (Fig. 3.6c,g,k), we can use the analytical solution in Eq. (3.24) as the exact solution. For the transverse profile (Fig. 3.6d,h,l), the transect is not a true symmetry axis; therefore, we can only use the analytical solution obtained by setting $\tan\beta = 0$ as an approximated solution. Since we do not have analytical deposit volume for these deposits on

doi:10.6342/NTU202204140

inclined planes, for each case, we impose a fixed thickness of the deposit at the origin for both analytical solutions and numerical solutions. Then we compare the results and find they match each other well.

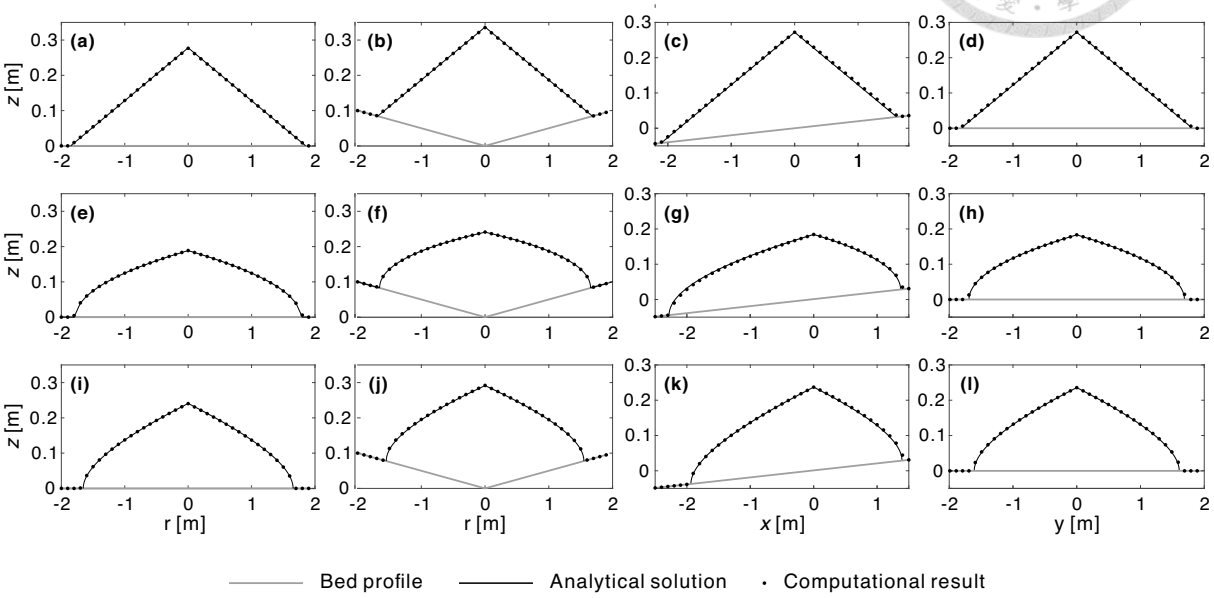

Figure 3.6: Comparison between computational and analytical solutions for different material parameters and geometries: (a,e,i) radial deposit profiles on horizontal plane; (b,f,j) radial deposit profiles on conical basin; (c,g,k) longitudinal deposit profiles on inclined plane; (d,h,l) transverse deposit profiles on inclined plane; (a-d) deposit with friction angle and no yield ($\tan\phi = 0.15$, $\tau_Y/(\rho g) = 0$ m); (e-h): deposit with yield stress and no friction angle ($\tan\phi$ =0, $\tau_Y/(\rho g) = 0.01$ m); (i-l): deposit with both friction angle and yield stress ($\tan\phi = 0.05$, $\tau_Y/(\rho g) = 0.01$ m).

To show how parameters affect results and check the numerical model under different assumptions, we compare numerical and analytical solutions for three groups of material properties. We first simulate the deposits with constant friction stress and no yield ($\tan\phi > 0$, $\tau_Y = 0$), producing final deposits with constant surface slopes, always equal to the friction slope regardless of the bed slope (Fig. 3.6a–d). The computational results and the analytical solutions match each other well and agree with physical and computational models for sand piles (Kuster and Gremaud, 2006; Giudice et al., 2019).

Next, we simulate the deposits with only yield stress ($\tan\phi = 0$, $\tau_Y > 0$) and obtain piles with mild slopes in the central regions and steep slopes along the margins

doi:10.6342/NTU202204140

of the deposit, resulting in toes that have a snout-like profile (Fig. 3.6e–h). The computational results for this case fit the analytical solutions and models proposed by Coussot et al. (1996) and Yuhi and Mei (2004) for slow mud flows (fluids with a Bingham plastic rheology). By considering the yield stress, it is therefore possible to reproduce the snout-like toes observed along the margins of many debris flow, mud flow and snow avalanche deposits (Johnson, 1970; Pudasaini and Hutter, 2007).

Finally, we simulate deposits affected by both friction and yield stress ($\tan\phi > 0$, $\tau_Y > 0$) and obtain excellent agreement between the computational results and the analytical solutions (Fig. 3.6i–l). Here we note that snout-like profiles are again obtained at the toes. Away from the toes, however, the deposit slope now tends toward a finite inclination, controlled by the friction angle. Overall the results in Fig. 3.6 clearly demonstrate how the friction angle and yield stress affect deposit shapes. Regardless of the choice of parameters, the numerical solutions match closely the analytical profiles, demonstrating the accuracy of the proposed CVFEM algorithm.

3.7.2 Influence of mesh geometry and size

By using triangular elements as building blocks, the CVFEM model can be applied to either structured or unstructured meshes. In Fig. 3.7, we show how model results are affected by mesh geometry and size. For these calculations, we again consider a simple test case in which material supplied at the origin deposits over a horizontal substrate, under the combined influence of friction angle and yield stress ($\tan\phi > 0$, $\tau_Y > 0$). For these tests a prescribed volume of material is supplied, by controlling the accumulated discharge supplied at the source.

Three different meshes are considered: a structured mesh, built from triangular elements laid out in a row-column pattern (Fig. 3.7a); an unstructured mesh, constructed by the mesh generation algorithm of Engwirda (2014) (Fig. 3.7b); a fine unstructured mesh, constructed by the same algorithm (Fig. 3.7c). The corresponding model results are shown in Fig. 3.7d–f, representing the calculated topography

doi:10.6342/NTU202204140

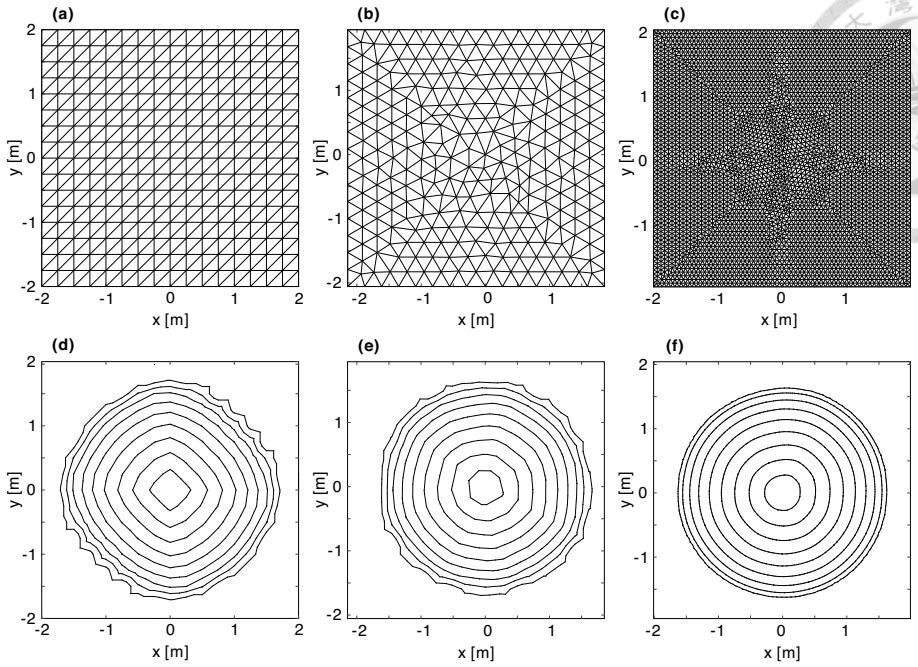

Figure 3.7: Mesh geometries (a,b,c) and calculated contours (d,e,f) for the deposition of a prescribed volume of material on a horizontal substrate: (a,d) structured mesh; (b,e) unstructured mesh; (c,f) fine unstructured mesh (8408 elements). The contours show deposit elevations $\tilde{z} = 0.1h, 0.2h, \ldots, 0.9h$.

by elevation contours.

In Fig. 3.7d, clear directional errors can be seen when results are computed on the structured mesh. In this case, the deposits contours visibly protrude along the x and y directions. Such errors can be reduced by using an unstructured mesh (Fig. 3.7e), and by calculating on a finer grid (Fig. 3.7f). By doing so, the calculated contours become closer to the expected circular pattern.

By performing tests on progressively finer meshes, we can also check the convergence of our CVFEM algorithm. For this purpose, we consider two predictive measures to assess grid convergence. The first is the ratio H/h between the calculated deposit height H and the analytical value $h = 0.241$ m. Noting that even unstructured meshes can introduce some bias (in particular when the mesh is coarse), our second measure is the difference between the maximum and minimum radii associated with the contour $\tilde{z} = 0.1h$, normalized by the analytical value $r_{10} = 1.628$ m.

doi:10.6342/NTU202204140

In Table 3.1, we list these height and radius measures for different mesh sizes, as characterized by the average length of element edges and by the number of elements of the mesh. As the mesh is refined, we see that the first measure (H/h) converges to 1, while the second measure ($(R_{10\,\max} - R_{10\,\min})/r_{10}$) approaches 0. In Table 3.1, we also report the computational time in seconds needed to run these simulations on an i5-9500 Intel processor.

Table 3.1: Influence of mesh size on model accuracy and computational time.

Avg. element size [m]	# of elements	H/h	$(R_{10\,\max} - R_{10\,\min})/r_{10}$	Computational time [s]
0.265	526	0.937	0.092	0.092
0.132	2116	0.968	0.037	2.46
0.066	8612	0.980	0.012	46.5
0.033	33986	0.989	0.007	1117.4

3.8 Comparisons with field and laboratory data

To further test the model, in the section we present comparisons with field and laboratory data. Measured profiles for the toes of debris flow deposits from Coussot et al. (1996) are first exploited, to verify the applicability of the critical slope and Mohr–Coulomb model to field cases. To study this kind of flow, small-scale experiments were designed and performed by Wu (2020). Comparisons with the experiments are then made, to check the ability of the CVFEM model to predict the overall morphology of cohesive-frictional deposits. The calibration and CVFEM numerical model code and input/output data discussed in this section are available in Chen et al. (2021).

3.8.1 Comparison with field profiles

Coussot et al. (1996) observed six natural debris flow deposits in the French Alps. By categorizing these deposits by their fines fraction (ratio of particles whose diameter is less than 40 μm to total solid volume), they found that debris flow deposits with a low fines fraction ($< 1\%$), at Bourgeat, Le Bez and Ste-Elisabeth, exhibit nearly

doi:10.6342/NTU202204140

straight profiles, whereas debris flow deposits with a high fines fraction (10%-15%), at Les Sables, St-Julien, and Mont Guillaume, exhibit significant snout-like toes. Coussot et al., therefore, focused on the latter case to test their model involving only the effect of yield stress. For each deposit with a high fines fraction, they documented two profiles, frontal and lateral, which they sought to fit by calibrating two parameters: the bed slope $\tan\beta$ and the yield stress over specific weight $\tau_Y/(\rho g)$. For each site, they calibrated these parameters separately for the frontal and lateral profiles. The lengths of the profiled deposits were in the range 2 to 15 m, and the corresponding thicknesses in the range 1.5 to 3 m.

Straight profiles, characterized by a constant slope, can be reproduced in our model by setting the yield stress to zero and the saturated friction slope $\tan\phi$ equal to the deposit surface slope. We therefore need to check whether our model can reproduce also the snout-like profiles observed for the case of high fines fraction. By taking both friction angle and yield stress into account, we can test whether analytical profiles can reproduce the field profiles using only one set of parameters per site. For this purpose, we assume that the frontal and lateral profiles at the same site share the same material properties ($\tan\phi$ and $\tau_Y/(\rho g)$). For the frontal profile, we treat the substrate bed slope ($\tan\beta$) as unknown, while for the lateral profile we assume that the bed slope is zero ($\tan\beta = 0$).

To estimate the three parameters, we fit the analytical solution given by Eq. (3.24) to the two measured profiles. Assigning the measured toe position as the boundary condition ($x_0 = x_{\text{toe}}$ and $H(x_0) = 0$), we obtain a predicted profile for given values of the frontal substrate bed slope $\tan\beta$, the saturated friction angle $\tan\phi$, and the ratio of yield stress over specific weight $\tau_Y/(\rho g)$. Then, on minimizing the root mean square error (RMSE) between predicted and measured fan profiles we arrived at best-fit estimates for $\tan\beta$, $\tan\phi$ and $\tau_Y/(\rho g)$.

In Fig. 3.8, we compare the resulting profiles with the field data, normalizing both axes by the length scale $\tau_Y/(\rho g)$. From the figure, we see that our critical slope

doi:10.6342/NTU202204140

model based on the Mohr–Coulomb constitutive law can fit the field observations well in the cases of Les Sables (Fig. 3.8a,b) and Mont Guillaume (Fig. 3.8e,f) and acceptably in the case of St-Julien (Fig. 3.8c,d). The ability to use the same parameters (friction angle and yield stress) to fit both frontal and lateral profiles is evidence that inertia can be neglected at the field scale for final deposits while it may have more significant effects during the flowing stage. On the contrary, sometimes inertia effects cannot be all neglected for the final deposit: for example, in the case of St-Julien, when using the same parameters the modeling results have larger differences from the field observations. For the debris flow deposits in Les Sables (Fig. 3.8a,b) and St-Julien (Fig. 3.8c,d), the additional parameter ($\tan\phi$) plays an important role in determining the deposit morphology, and provides the degree of freedom needed to describe each pair of profiles for the same site using the same set of parameters. For Mont Guillaume (Fig. 3.8e,f), calibration produces a low value for the saturated friction angle, indicating that the yield stress and bed slope are sufficient to represent the deposit morphology. This may be due to the high clay content at this site.

Depending on scale and material composition, either the friction angle or the yield stress alone may be sufficient to characterize certain debris deposits in the field. Both influences, however, must be considered for intermediate cases, and to encompass the range of possible behaviors in a single description. In the field and experiments, note that other effects can cause or contribute to the formation of steep snouts, such as pore pressure loss at the front or along the margins of debris flows, where sorting of particles can increase permeability (e.g. Iverson, 1997; Iverson and Vallance, 2001; Savage and Iverson, 2003; Iverson et al., 2010; Gray, 2018) and the frictional hysteresis of the angular sand particles (e.g. Félix and Thomas, 2004; Mangeney et al., 2007; Edwards et al., 2017; Rocha et al., 2019; Edwards et al., 2019). These effects are not currently included in our model.

To go beyond transect comparisons, in the next section we will use laboratory

doi:10.6342/NTU202204140

experiments to test the ability of our CVFEM model to simulate the complete morphology of cohesive-frictional deposits.

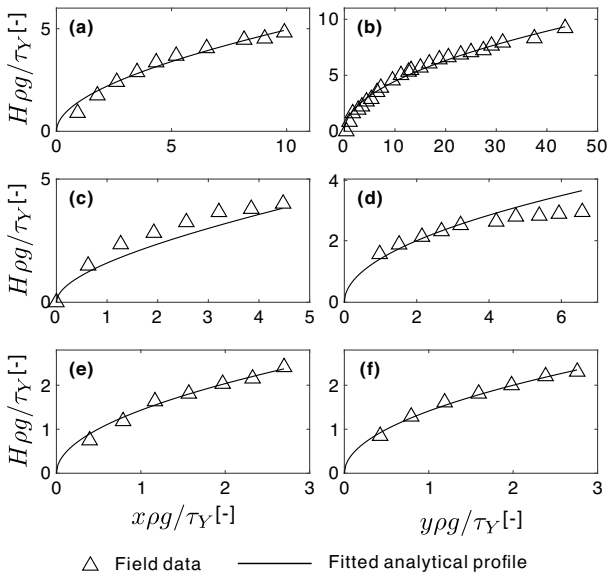

Figure 3.8: Comparison of debris deposit profiles at three field sites in the French Alps (Coussot et al., 1996) with analytical profiles calculated using calibrated values for parameters $\tan\beta$, $\tan\phi$ and $\tau_Y/(\rho g)$: (a,c,e) Frontal profiles; (b,d,f) lateral profiles; (a,b) Les Sables ($\tan\beta = 0.136$, $\tan\phi = 0.069$, $\tau_Y/(\rho g) = 0.297$ m); (c,d) profiles for St-Julien ($\tan\beta = 0.296$, $\tan\phi = 0.262$, $\tau_Y/(\rho g) = 0.432$ m); (e,d) profiles for Mont Guillaume ($\tan\beta = 0.245$, $\tan\phi = 0.028$, $\tau_Y/(\rho g) = 0.656$ m).

3.8.2 Experimental design and conditions

To investigate the morphology of cohesive-frictional deposits in well-controlled conditions, but more complex geometries, Wu (2020) designed and performed two series of small-scale experiments. As illustrated in Fig. 3.9, these experiments were conducted in faceted flumes, assembled from bevelled wood panels. Different from alluvial fan experiments (Le Hooke and Rohrer, 1979; Whipple et al., 1998; Delorme et al., 2018; Savi et al., 2020), involving water and cohesionless sediment, here the deposits are built from mixtures of sand, kaolinite and water, mixed together thoroughly to behave as a cohesive-frictional material. To produce varied deposits, controlled volumes of these mixtures were supplied upstream of steep V-shaped canyons, and conveyed by these canyons to zones of milder topography where they

doi:10.6342/NTU202204140

could spread, slow, and freeze in place. Water-soluble dyes were added to distinguish the materials supplied to different canyons. Finally laser scanning (Ni and Capart, 2006; Lobkovsky et al., 2007) was used to acquire high-resolution maps of the substrate and deposit topography.

As illustrated by the photographs of Fig. 3.9d–f, the experiments generate rather idealized deposits, which nevertheless reproduce various features exhibited by debris flow deposits in the field. These include steep snouts along lobe margins, and cusped weld lines where separate lobes come into contact. Surface folds, indicative of viscoplastic behavior, can be observed at various locations (see for instance the lobe in the foreground of Fig. 3.9e), similar to the folds visible in some areas of the field deposit shown in Fig. 3.1.

Two series of tests were conducted: canyon-plain experiments (T01–T04), using the geometry shown in Fig. 3.9a, and canyon-valley experiments (T11–T15), using the geometry shown in Fig. 3.9b. For the canyon-plain experiments (runs T01–T04), two V-shaped canyons connect to a wide U-shaped plain that has a planar floor and vertical walls. The canyon thalwegs have an inclination of 18.8 degrees relative to the planar floors. The experiments were designed so that the whole flume could be tilted away from horizontal, in the longitudinal direction of the tributary channels. In each run, a mixture of 61.4 wt% silica sand ($d_{50} = 0.6$ mm), 8.8 wt% kaolin, and 29.8 wt% water was used to deposit a fan into an initially empty and clean flume.

For run T01 the flume floor was horizontal, and two equal volumes of mixture were poured simultaneously upstream of the two canyons. For run T02 the inclination was the same, but the volumes supplied to the two tributary channels TC1 and TC2 were in a ratio of 1 to 2. The continuous mass input was arranged to start and end at the same time. Runs T03 and T04 were identical to run T02 apart from different flume tilt angles, set respectively to 3 and 6 degrees. For these runs, the topography was scanned with the laser oriented perpendicular to the canyons, and the resulting DEM data have resolution 2 mm x 2 mm.

doi:10.6342/NTU202204140

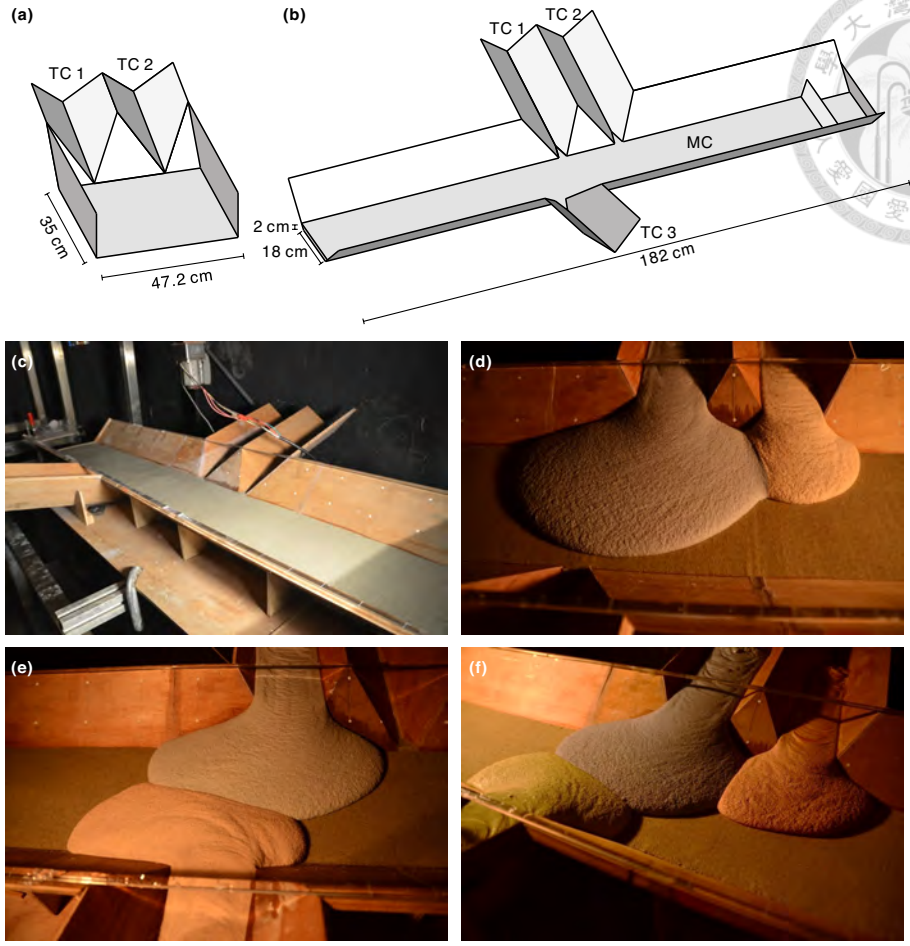

Figure 3.9: Experimental set-up and photos: (a) flume geometry for the canyon-plain experiments (T01–T04); (b) flume geometry for the canyon-valley experiments (T11–T15); (c) initial condition for runs T11–T14; (d,e,f) final deposits for runs T12, T13, and T14.

For the canyon-valley experiments (T11–T15), the flume had a more complex configuration, illustrated in Fig. 3.9b. Three V-shaped canyons, having thalweg inclinations equal to 14 degrees, connect at right angles to a wide trapezoidal channel of longitudinal inclination equal to 3 degrees. Two of the canyons (TC1 and TC2) connect on the right side, and one on the left (TC3), slightly downstream. In all runs the initial state of the canyon was clean wood, but the main channel was covered by a 2 cm thick layer unconsolidated silica sand (d_{50} = 0.6 mm). For run T11 a controlled volume of mixture was supplied to tributary TC1 only. For run T12 different volumes were supplied simultaneously to tributaries TC1 and TC2, and arranged to start and end at the same times. For run T13 different volumes

doi:10.6342/NTU202204140

were supplied to tributaries TC1 and TC3, and for run T14 different volumes were supplied simultaneously to all 3 tributaries.

For run T15, deposits were formed in three separate stages. In the first stage, deposits were formed as in run T13 by supplying different volumes to tributaries TC1 and TC3. In the second stage, a constant water discharge was supplied to the main channel for 20 minutes, eroding the first stage deposits. The resulting topography was scanned to provide initial conditions for the third stage, in which new volumes of material were supplied to tributaries TC1 and TC3. This provides an opportunity to examine the formation of fresh deposits onto a pre-existing deposit surface. For all canyon-valley experiments, the topography was scanned with the laser oriented orthogonal to the main channel and parallel to the canyons, and the resulting DEM data have resolution 5 mm by 5 mm.

In the next sections, the data from these different experiments will be used to calibrate model parameters, and compare CVFEM simulation results with the topography measurements acquired in each case.

3.8.3 Comparison with canyon-plain experiments

To apply the CVFEM method to the canyon-plain experiments (runs T01–T04), we first determine model parameters from longitudinal deposit profiles, measured along the centrelines of the deposits from each canyon (see example profile locations in Fig. 3.10a). The calibration method used is the same as the one applied to the field profiles, except that the substrate slope $\tan\beta$ is known from the flume geometry, hence only the material parameters $\tan\phi$ and $\tau_Y/(\rho g)$ remain to be determined. For this set of experiments, some variability in material properties was caused by uncontrolled variations in moisture in the kaolin. For this reason, we use all eight of the available measured profiles together, to estimate a pair of parameters that best fit the whole series of experiments. The resulting estimates are $\tan\phi = 0.063$ and $\tau_Y/(\rho g) = 0.115$ cm.

doi:10.6342/NTU202204140

Initial and boundary conditions are set up as follows. An unstructured mesh of average element size $\Delta\ell = 4$ mm is generated over the problem domain. The flume topography measured before each experiment is then used to set the substrate and initial surface elevations $z_b(x, y)$ and $\tilde{z}(x, y, 0)$. To input the deposits, constant discharge sources are placed at the vertices closest to the upstream ends of the two channel thalwegs $(x, y) = (0{,}10)$ cm and $(x, y) = (0{,}34.8)$ cm, respectively. The rates of these discharges are set to ensure that, at the end of the chosen simulation time, the volumes supplied match the measured experimental volumes for each source.

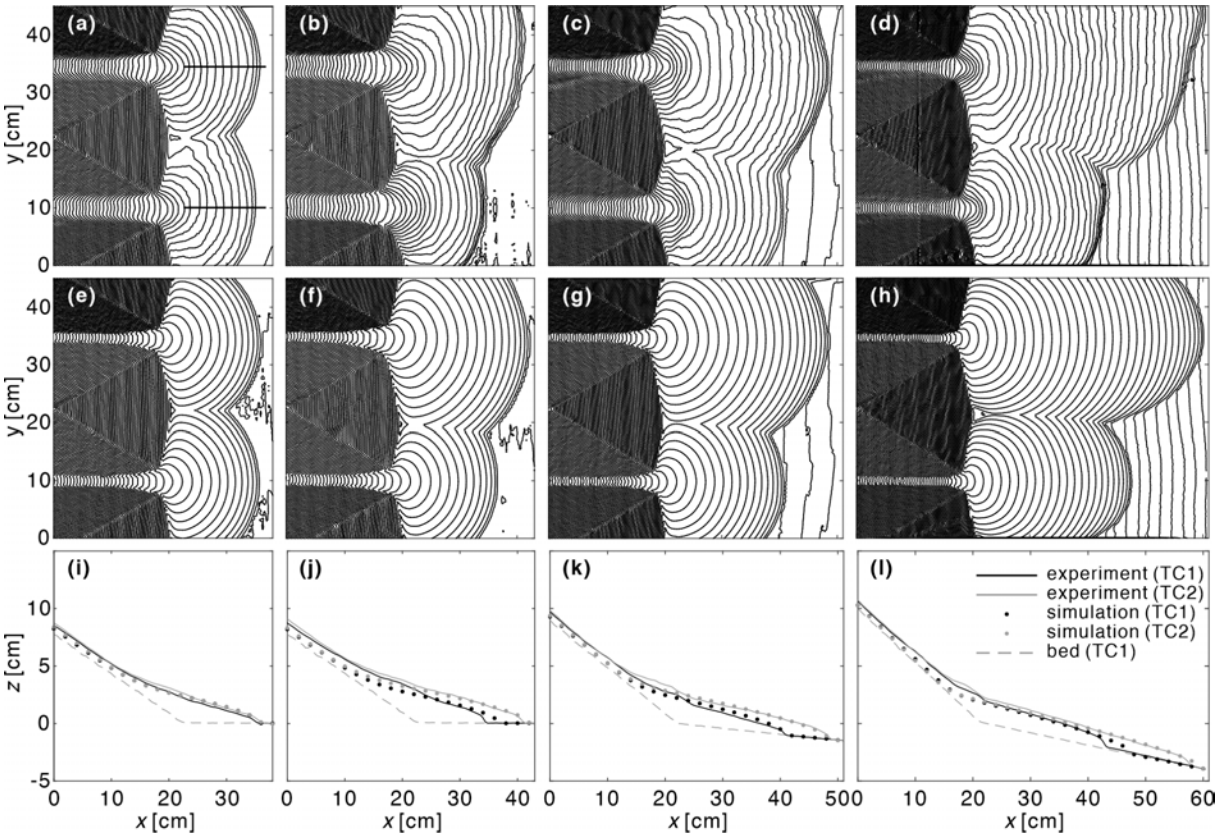

Figure 3.10: Comparison of measured and simulated deposit topographies for the canyon-plain experiments. Left to right: runs T01, T02, T03, and T04 corresponding to flume inclinations of 0, 0, 3, and 6 degrees; (a-d) experimental results; (e-h) CVFEM simulations; (i-l) longitudinal profiles for transects y = 10 cm (black) and y = 34.8 cm (gray), along the centerlines of the deposits. Contours at intervals $\Delta z = 0.2$ cm.

In Fig. 3.10, we compare simulation results with the experimental measurements for the four runs T01–T04. Qualitatively and quantitatively, the simulations are

doi:10.6342/NTU202204140

found to predict reasonably well the measured topography of the deposits. As indicated by the contours, both the simulations and experiments produce grooves along the margins where the deposit intersects with the substrate, steep snouts along lobe margins, well-defined cusps along weld lines, where two lobes come into contact, and saddle points along these same weld lines.

In planform (Fig. 3.10a–h), the model is able to reproduce well the outer boundaries of the deposits, both along the steep canyon and valley sides, and over the mildly inclined floor. Agreement holds for both the symmetric (equal volumes supplied to the two canyons) and asymmetric cases (unequal volumes). The model also reproduces the gradual elongation of the deposit lobes as the flume inclination is increased.

In profile (Fig. 3.10i–l), model results also compare well with the measurements. The model is able to capture the observed deposit slope variations, from steep upstream of the canyons, to mild over the thick lobes, back to steep snouts at the downstream toes. In both the simulations and experiments, furthermore, the deposits become gradually shallower as the flume slope is increased.

Nevertheless, there are some discrepancies between the CVFEM model and the experiments. Within the canyons and at canyon outlets, the model produces narrower and shallower deposits than the experimental results. This could be due to the geometrical simplifications used to derive the critical slope model, in which the basal substrate was assumed approximately parallel to the surface. There are also some mismatches in planform length and width, possibly due to the previously mentioned moisture variations between runs. This is especially notable for the distal parts of run T04.

3.8.4 Comparison with canyon-valley experiments

For the canyon-valley experiments (T11–T15), the moisture was better controlled, hence the material composition was more nearly identical for all runs. We can

doi:10.6342/NTU202204140

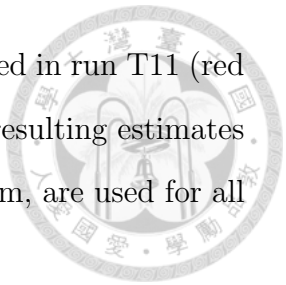

therefore use the longitudinal profile for the single deposit produced in run T11 (red line in Fig. 3.11a) to calibrate the parameters for all cases. The resulting estimates for the material parameters, $\tan\phi = 0.118$ and $\tau_Y/(\rho g) = 0.344$ cm, are used for all CVFEM simulations of this series.

To simulate these runs, we use an unstructured mesh of average element size $\Delta\ell = 5$ mm. Like before, for each case we obtain the initial condition by sampling the measured pre-event topography at the mesh nodes. For runs T11–T14, we prescribe point sources of constant discharge at the vertices where canyon thalwegs intersect the domain boundaries (red points in Fig. 3.11). For run T15, the deposits partly buried the canyons, hence line sources are used instead at cross sections along the domain boundary (red lines in Fig. 3.11j). The discharge for these various sources are again set to match the volumes of the individual deposits.

To compare measured and simulated results, topographic contours and deposit thickness maps for the different cases are presented in Fig. 3.11. Overall, good agreement is observed between the CVFEM simulations and the experiments. Because the main channel dips to the left, the deposit lobes acquire an asymmetric, distorted shape, which is well-reproduced by the simulations. In both the experiments and the simulations, steep snouts are produced along the outer and side margins of the deposits, where they connect with the valley bed and sides. For runs T12 to T14, the weld lines obtained where different lobes come into contact are also accurately predicted. Using a single set of material parameters, the simulations also reproduce well the deposit thickness distributions obtained in the different experiments.

Similar to the canyon-plain experiments, some discrepancies are nevertheless observed between the simulations and experiments. The simulated fans are slightly wider (x direction) and shorter (y direction) than their experimental counterparts. This could be due to momentum, neglected in our CVFEM model, allowing the experimental mixture to flow out further in the canyon direction.

The T15 experiment, finally (Fig. 3.11i,j), allows us to test our model for the case

doi:10.6342/NTU202204140

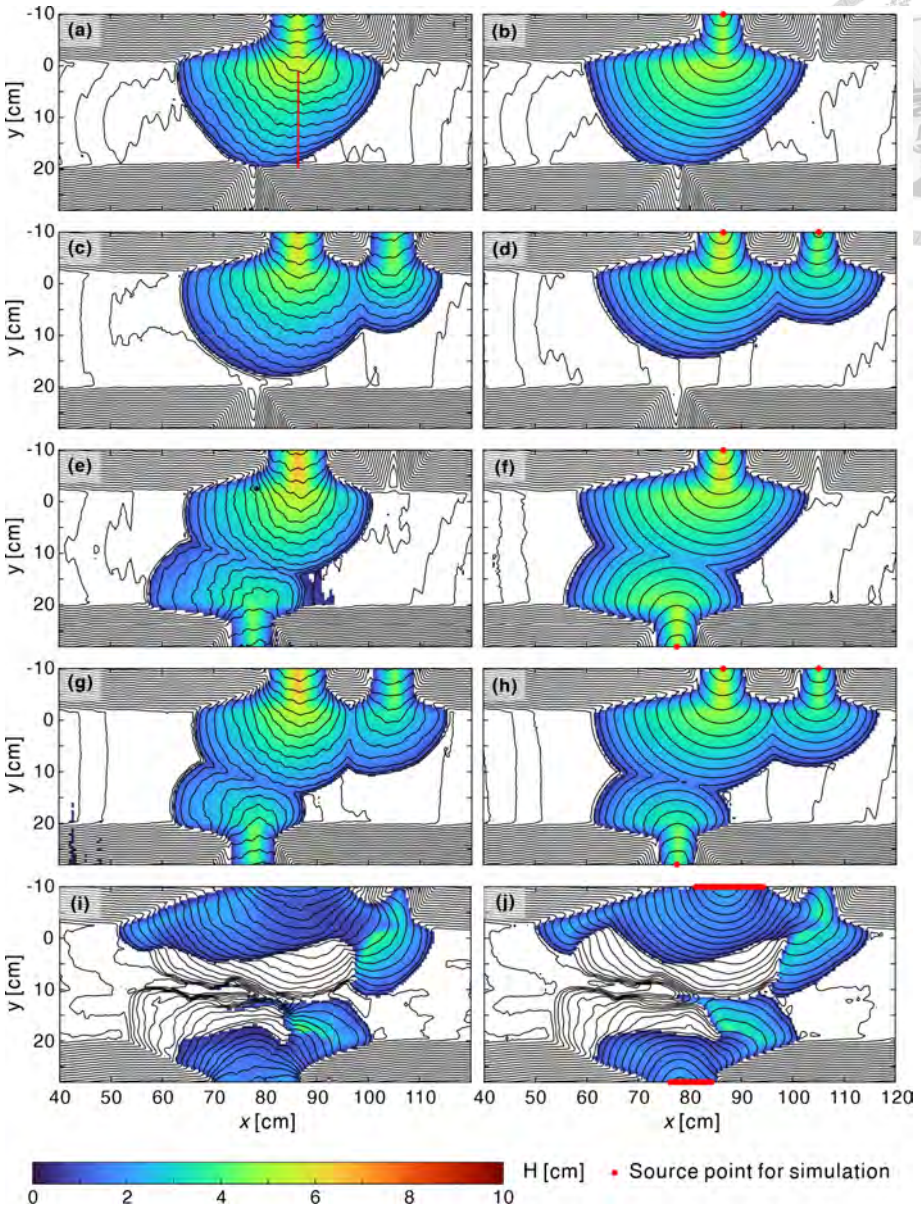

Figure 3.11: Comparison of measured (left) and simulated deposit topographies (right) for the canyon-valley experiments: (a,b) run T11; (c,d) run T12; (e,f) run T13; (g,h) run T14; (i,j) run T15. Lines: elevation contours at intervals $\Delta z = 0.5$ cm.

of fresh deposits onto a pre-existing deposit of complex shape. In the experiments, the earlier deposit may deform slightly due to the new deposition, but we neglect this complication and take it as a new rigid boundary in the simulations. For this challenging case, the CVFEM model again provides an excellent overall prediction of the thickness, extent, and morphology of the secondary deposits. In both experiment and simulation, the fresh deposits do not completely cover the pre-existing lobes.

doi:10.6342/NTU202204140

The fresh material stops over these lobes at some locations, flowing further at other locations to form new secondary lobes. The corresponding margins again feature well-defined snouts. As illustrated by Fig. 3.1, some debris flow deposits on pre-existing fans in the field exhibit very similar features to the deposits in the T15 experiment.

3.9 Conclusions

In this chapter, we proposed a novel computational model to simulate the morphology of debris flow deposits. The numerical algorithm uses the control volume finite element method (CVFEM) to discretely approximate fluxes over a finite element mesh, and explicitly enforce mass balance over prescribed control volumes. Unlike fluvial and mud flow deposits, debris flow deposits are affected by both cohesion and friction. To set the critical slope at which flow starts or stops, we therefore adopted a Mohr–Coulomb criterion that includes both a yield stress and a friction angle.

We verified the CVFEM algorithm by comparing computational results to analytical solutions in idealized cases, obtaining excellent agreement. Comparisons with field profiles were then performed to check that our critical slope model based on the Mohr–Coulomb relation can reproduce the key features of debris flow deposits. For deposits characterized by a high fines fraction, the inclusion of a yield stress allows our model to reproduce the blunted snouts observed at deposit toes. Accounting for a friction angle, on the other hand, allows our model to match the trailing slope observed away from the toes, and makes the model applicable also to deposits with a low fines fraction, which feature more even slopes.

Finally, comparisons with new laboratory experiments were conducted to test the ability of our CVFEM model to predict the extent, thickness and morphology of cohesive-frictional deposits in more complex geometries. The conditions considered include supply by single and multiple sources, and deposition over faceted substrates and pre-existing deposits. Using material parameters calibrated from one or more

doi:10.6342/NTU202204140

transects, the model is found to reproduce well the measured topography in all cases. Deposits features captured accurately by the model include steep snouts along the margins of primary and secondary lobes, and cusped weld lines where different lobes come into contact.

Although good agreement was obtained for the different comparisons, the model is nevertheless subject to various limitations. First, the model runs with hypothetical diffusivity and pseudo time steps and therefore simulates quasi-static deposit morphology instead of morphodynamics. Second, flow momentum and basal erosion are neglected, hence the model does not apply to rapid or erosive debris flows (Armanini et al., 2005). Besides, the model does not include other effects that may lead to the formations of snouts and channel levees, such as pore pressure loss at the front or along the margins of debris flows, where sorting of particles can increase permeability (Iverson, 1997; Iverson and Vallance, 2001; Savage and Iverson, 2003; Iverson et al., 2010; Gray, 2018) and the frictional hysteresis of the angular sand particles (Félix and Thomas, 2004; Mangeney et al., 2007; Edwards et al., 2017; Rocha et al., 2019; Edwards et al., 2019). Likewise, it does not account for the thixotropic behavior whereby deposits gradually solidify to form a new substrate for fresh deposits (Murata, 1984; Roussel, 2006). Finally, our model and experiments do not include processes like channel formation, migration and avulsion that also affect the evolution over time of debris and alluvial fans (Le Hooke and Rohrer, 1979; Whipple et al., 1998; Delorme et al., 2018; Savi et al., 2020).

Despite these current limitations, we have shown that a critical slope model accounting for yield stress and friction angle can simulate deposit morphology for a broader range of conditions than considered previously. To simulate such deposits in complex geometries, moreover, the control volume finite element method (CVFEM) was found to provide a promising numerical approach, and could possibly be extended in the future to more general processes or other geomorphic systems.

doi:10.6342/NTU202204140

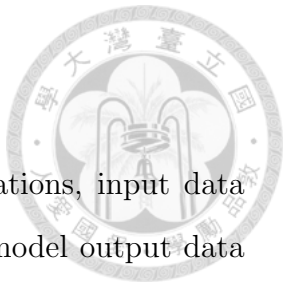

3.10 Code and data availability

The Matlab codes of the CVFEM model and parameter calibrations, input data (experimental pre-event and post-event topography data), and model output data are available at Chen et al. (2021), https://doi.org/10.5281/zenodo.5933841.

The algorithm for constructing unstructured mesh used in this chapter is an open access Matlab package built by Engwirda (Engwirda, 2014) available at https://github.com/dengwirda/mesh2d.

The algorithms for linearly interpolating triangulation and plotting contours for triangular mesh used in this chapter are open access Matlab codes built by Hanselman (Hanselman, 2021b,a) available at https://www.mathworks.com/matlabcentral/fileexchange/38925 and https://www.mathworks.com/matlabcentral/fileexchange/38858.

doi:10.6342/NTU202204140

Chapter 4

Influence of fine particle content in debris flows on alluvial fan morphology

Alluvial fans are large-scale depositional structures commonly found at the base of mountain ranges. When frequented by debris flows (massive, muddy, rocky flows) they contribute significantly to local hazards as they carry focused, collisional, fast-moving materials across alluvial fans, unpredictable in size, speed, and direction. We research how fine particle content in debris flows correlates with directional changes, i.e., debris flow avulsions. Toward this, we analyzed field data from two neighboring alluvial fans in the White Mountains (California, USA) that exhibit dramatically different topographies despite their proximity and associated similar long-term climates. Informed by these measurements, we performed long-term and incremental alluvial fan experiments built by debris flows with systematically-varied fine particle content. We found that (1) decreasing fine particle content increases the variability of fan slopes and associated channelization dynamics, and (2) for all mixtures longer-term continuous alluvial fan experiments form more complex surface channelizations than repeated flows for the same total time, indicating the importance of *both* particle sizes and timescales on alluvial fan surface morphology.

Submitted manuscript: Chen, T. Y. K., Hung, C. Y., Mullenbach, J., and Hill, Kimberly. Roles of Fine Particle Content and Timescales in Debris Flow Hazards on Alluvial Fans, *Scientific Reports*. (Under review).

doi:10.6342/NTU202204140

4.1 Introduction

Alluvial fans are large-scale conical structures that often form in chains (or bajadas (Gilbert, 1882)) at the base of mountainous regions worldwide: in wetter warmer climates (Kochel and Johnson, 1984; Saito and Oguchi, 2005; Hsieh and Capart, 2013; Lo, 2017; Lo et al., 2018), in periglacial climates (de Haas et al., 2015b; Tomczyk, 2021), and in arid environments (where they have been most commonly studied) (Drew, 1873; Gilbert, 1882; Hooke, 1967; Harvey, 2002; Whipple and Dunne, 1992). They are primarily comprised of abraded colluvium carried by repeated flows of streams and/or debris flows from steeper catchment areas. Because of associated break-up processes (from abrasion to comminution), fans contain relatively workable regolith compared to the bedrock in their catchments, making the fans particularly suitable for human infrastructure in mountainous areas. Yet, many of these fans were built by debris flows: unpredictable and destructive flows of boulders, gravel, and mud, motivating significant study of similar future events.

Typically, debris flows travel from the steeper catchment are through relatively narrow canyonlands and into a wider expanse at the fan apex, after which they often channelize the more shallow-sloped fan and deposit. The dynamics of the flows vary with many factors including: grain size distributions, water content, and local slopes. All of these factors are governed by much longer-term dynamics from geomorphological processes to local hydrology and climate. Subsequently, debris flows and their subsequent depositional structures can vary substantially. For example, in wetter tropical regions whose lithology is dominated by sedimentary rock (as in Taiwan, e.g., Fig. 4.1**a**) debris flows appear more muddy, at first glance similar to sheet flows, though still suspending and then dispersing gravel, rocks, and massive boulders across much of the fan in single-flow events. In drier areas, single debris-flow events appear rockier and fluid-starved at their fronts (i.e., "snouts") and are often restricted to a single channel over any particular flow event (Berger

doi:10.6342/NTU202204140

et al., 2011). Sometimes even several consecutive debris flow events deposit over a relatively narrow fan region (Dühnforth et al., 2007; de Haas et al., 2018; Densmore et al., 2019). Still, among the deposits, certain commonalities define what the scientific community associates with debris-flow dominated fans: large boulders scattered across fan surfaces; relatively high catchment slopes; stream cuts and levees that reveal poorly-sorted thickly-layered deposits, and depositional "lobes," tongue-shaped depositional structures (Tsai, 2006; Scheidl and Rickenmann, 2010; Chau et al., 2000).

Many efforts have been successful at associating properties of catchment regions and alluvial fan structure with likelihood of past or future debris flows and their magnitudes (Jackson et al., 1987; Marchi et al., 1993; Marchi and Tecca, 1995). For example, Melton (1965) found a distinguishing measure of debris-flow (rather than stream-flow) dominated fans in Arizona to be what he called the *ruggedness* of the catchment area ($R = H/\sqrt{A}$; H and A represent the maximum vertical relief and the planview area, respectively). Jackson et al. (1987) (in the Canadian Rockies) and Marchi et al. (1993); Marchi and Tecca (1995) (in the Italian Alps) found high magnitudes of the Melton number and also slope correlated with debris-flow dominated fans. Recently research been directed toward relating variability in flow *contents* and particular dynamics – specifically *avulsion behaviors* – to distinctions in *depositional structures* (de Haas et al., 2016; Brown, 2016; de Haas et al., 2018; Pederson et al., 2015; Zubrycky et al., 2021; Herbert, 2021; Densmore et al., 2019). Yet significant questions remain regarding avulsion controls whether it be local rock materials, hydrology, and/or climate forcing.

While significant attention has been paid to grain-size distributions of larger particles (D'Arcy et al., 2017; Tsunetaka et al., 2021) relatively little attention has been paid to finer particle grain size distributions in the field (i.e., particles ¡ 2mm in diameter). However, recent work has demonstrated importance of fine particle content in particle-fluid materials in general and in-channel debris flow dynamics

doi:10.6342/NTU202204140

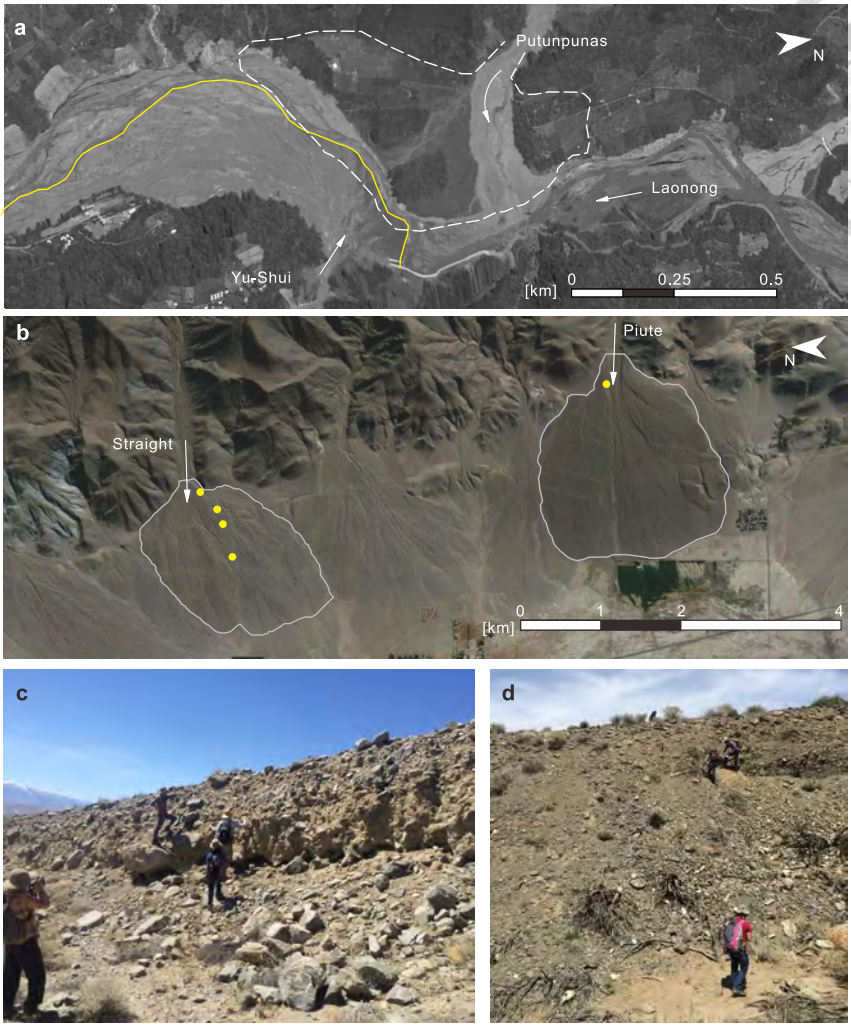

Figure 4.1: Examples of debris-flow dominated alluvial fans in the field, from **a** Laonong River Valley, Taiwan and **b-d** Owen's Valley, White Mountains, California, US. **a**, Laonong river's satellite image in August, 2021. (1) white lines indicate the DEM-determined Pu-tun-pu-nas fan boundary in February 2020; (2) yellow lines(solid/dash) indicate the DEM-determined Yu-Shui fan boundary in August 2021 **b**.(b) Owens Valley satellite image, September 2019. White lines denote DEM-determined fan boundaries for Straight and Piute. Yellow dots indicate sampling locations. **c**, **d**, photos with (researchers for scale) on the channel levees in **c** Straight and **d** Piute.

in particular. For example, debris flow experiments at laboratory scale (Yohannes et al., 2012; Kaitna et al., 2014, 2016) and larger flumes (Iverson et al., 2011; Iverson, 2015) have demonstrated that in-channel debris-flow behaviors, particle sorting and mobility vary significantly with fine particle content. Related multi-scale computational and experimental studies of multi-scale particle-fluid systems (Man and Hill,

doi:10.6342/NTU202204140

2021; Man et al., 2022) have demonstrated the distinct role of fine particle content in mediating system-scale behaviors by modifying larger particle-particle interactions. Motivated by these results, herein we investigate how fine particle content may be related to differences in down-slope avulsion controls using preliminary field observations and systematic laboratory experiments.

4.2 Methods

4.2.1 Field case analysis

To test for evidence of the influence of fine particle content on field-scale avulsion behaviors on alluvial fans, we consider similarities and differences of two fans on the west side of the White Mountains (California, USA) (Figs. 4.1**b-d**): Straight and Piute Fans. Their relatively high slopes and catchment area roughness numbers are presented in Table 4.1.

For our field data we obtained: (1) documented lithology of the catchment areas; (2) the fine particle grain size distribution (2mm and finer), often considered a substantial part of the muddy fluid or "matrix" of a debris flow, and (3) measures of slopes and complexity of channelization.

Table 4.1: Data from Straight and Piute Fans and catchment areas. S_i refers to the slope for which i% of the slopes are smaller.

Fan Name		Straight	Piute
Catchment	Max height [m]	3747	3836
	Min height [m]	1577	1635
	Drainage area [km^2]	6.29	15.08
	Meltons number [-]	0.87	0.57
Fan	Fan area [km^2]	3.12	3.79
	S_1	0.0411	0.0778
	S_5	0.0593	0.1085
	S_{25}	0.1012	0.1301
	S_{50}	0.1440	0.1449
	S_{75}	0.1943	0.1640
	S_{95}	0.3197	0.2337
	S_{99}	0.4864	0.3820

doi:10.6342/NTU202204140

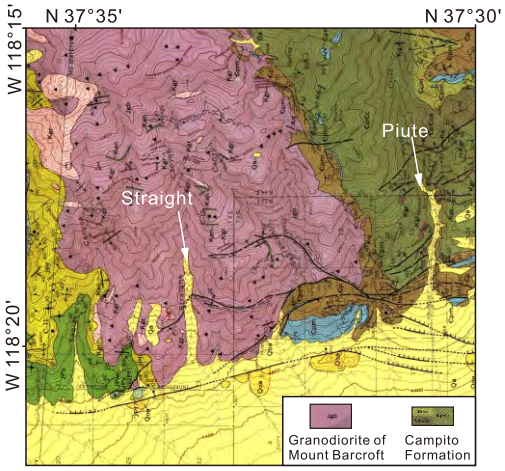

Figure 4.2: Field geological map Crowder and Sheridan (1972). The catchment material of Straight Creek and fan is primarily granodiorite, a relatively hard (∼225 MPa) coarse-grained intrusive igneous rock comprised of quartz and plagioclase feldspar. In contrast, the catchment material of Piute Creek primarily consists of hornfels, contact metamorphic rock that is considerably less hard (∼5.8 MPa). Additionally, at the base of the Piute catchment, adjacent to the apex of the fan, the material is that of the poleta formation, mostly sedimentary rock, silt and limestone Crowder and Sheridan (1972); McKee and Gangloff (1969).

We relied on a previously published USGS map (Crowder and Sheridan, 1972) for the lithology (Fig. 4.2 and caption). We used the data measured by Mullenbach (2018), which provides the fine particle size distribution from regions shielded from non-debris flow events, such as rain-wash or fluvial transport (Sampling location: Fig. 4.1**b** and Table 4.2; sampling results: Fig. 4.3 and Table 4.3). To do so, Mullenbach (2018) sampled beneath large objects (e.g., boulders) in levee walls of what appeared to be the most recent flow event for that fan. To sample below the protective object, they scraped away the exposed material from the roughly vertical wall surface beneath it and collected material from the region we exposed behind that for our measurements. For the Straight Fan, they took samples from the channel walls we associated with the historic debris flow recorded in 1918 based on the lighter coloration and previous documentation as in (Beaty, 1963). There is no recent, indeed no historical, debris flow on the Piute fan, so they sampled the sediment near the fan apex from within the top levee layer approximately 20m above the bottom of what they judged to be the most recent channel based on apparent

doi:10.6342/NTU202204140

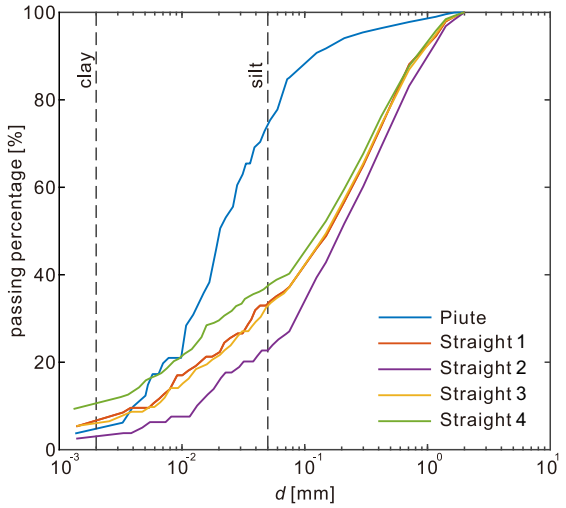

Figure 4.3: Fine particle (d < 2 mm) grain size distribution for Straight and Piute in the White Mountains (California, USA). Based on our measurements, the matrix particles of the Straight fan deposit are more than 60% sand while the finer grains on the Piute grains were more than 75% silt or finer.

stream activity at its base. The During the their preliminary field visit, additional sample collection was not part of the scope, though we plan to do this during near future visits. Mullenbach (2018) used sieves to measure the fractions of each grain size down to approximately 0.5mm. For smaller sizes we used sedimentation (hydrometer) analysis (ASTM D7928-17, 2016). For slopes and channelization, we used published Digital Elevation Model data (Lifton, 2013). We processed this for slopes and channel statistics, similar to the methodology for the experiments, described in the next section.

Table 4.2: GPS data for locations of the fine particle sampling in the field.

	UTM zone 11		
Fan Name	Easting (m)	Northing (m)	Elevation (m)
Piute	382956	4152326	1565
Straight 1	381728	4157467	1548
Straight 2	381512	4157255	1503
Straight 3	381328	4157184	1470
Straight 4	380919	4157066	1411

doi:10.6342/NTU202204140

Table 4.3: Sediment size distribution for the field (only showing the part of sand/silt/clay (d<2mm) (Information for sampling location see Table 4.2).

Piute		Straight 1		Straight 2		Straight 3		Straight 4	
grain size (mm)	passing rate (%)	grain size (mm)	passing rate (%)	grain size (mm)	passing rate (%)	grain size (mm)	passing rate (%)	grain size (mm)	passing rate (%)
2.00000	100.0	2.00000	100.0	2.00000	100.0	2.00000	100.0	2.00000	100.0
1.65000	100.0	1.65000	99.0	1.65000	98.3	1.65000	99.0	1.65000	99.2
1.41000	99.6	1.41000	97.9	1.41000	96.8	1.41000	98.1	1.41000	98.4
1.16800	99.0	1.16800	94.5	1.16800	92.8	1.16800	94.9	1.16800	95.8
0.71000	97.8	0.71000	88.1	0.71000	82.7	0.71000	86.9	0.71000	87.8
0.41700	96.3	0.41700	73.9	0.41700	68.3	0.41700	74.1	0.41700	76.2
0.29700	95.4	0.29700	65.0	0.29700	58.9	0.29700	65.2	0.29700	67.7
0.21000	94.0	0.21000	56.7	0.21000	50.1	0.21000	57.0	0.21000	59.6
0.14900	91.7	0.14900	48.8	0.14900	41.0	0.14900	49.1	0.14900	52.3
0.12500	90.6	0.12500	46.1	0.12500	37.4	0.12500	45.9	0.12500	49.2
0.07500	84.9	0.07500	37.2	0.07500	24.7	0.07500	36.7	0.07500	40.3
0.07197	83.7	0.06766	36.1	0.07058	24.2	0.06794	34.7	0.07145	39.9
0.05990	78.7	0.05882	35.1	0.06113	23.0	0.05930	33.6	0.05894	38.9
0.05212	76.2	0.05261	34.0	0.05487	21.9	0.05304	32.6	0.05155	37.8
0.04705	73.7	0.04839	33.0	0.05009	20.7	0.04860	31.5	0.04634	36.7
0.04334	71.2	0.04328	33.0	0.04480	20.7	0.04380	29.4	0.04271	36.1
0.03894	69.9	0.03951	31.9	0.04118	19.6	0.03999	28.4	0.03820	35.6
0.03587	66.2	0.03672	29.8	0.03813	18.4	0.03716	27.3	0.03521	35.0
0.03321	66.2	0.03461	28.7	0.03566	18.4	0.03476	26.3	0.03260	34.5
0.03120	63.7	0.03118	26.6	0.03190	18.4	0.03109	26.3	0.03064	33.4
0.02814	61.2	0.02846	26.6	0.02932	17.3	0.02860	25.2	0.02766	32.8
0.02602	56.2	0.02465	25.5	0.02539	16.1	0.02495	23.1	0.02548	31.7
0.02272	53.7	0.02213	24.5	0.02271	16.1	0.02231	22.1	0.02216	30.6
0.02049	51.2	0.02035	22.3	0.02080	15.0	0.02044	21.0	0.02000	29.5
0.01893	46.2	0.01762	21.3	0.01814	12.7	0.01770	20.0	0.01826	29.0
0.01671	38.7	0.01576	21.3	0.01622	11.5	0.01595	18.9	0.01588	28.5
0.01500	36.2	0.01296	19.1	0.01333	9.2	0.01302	17.9	0.01445	25.7
0.01234	31.2	0.01126	18.1	0.01158	6.9	0.01136	15.8	0.01204	23.0
0.01081	28.7	0.01007	17.0	0.01036	6.9	0.01020	14.7	0.01047	21.9
0.00984	21.2	0.00914	17.0	0.00946	6.9	0.00931	13.7	0.00944	20.8
0.00898	21.2	0.00797	13.8	0.00819	6.9	0.00806	13.7	0.00862	20.2
0.00778	21.2	0.00718	12.8	0.00737	5.8	0.00726	11.6	0.00755	18.6
0.00701	20.0	0.00656	11.7	0.00673	5.8	0.00667	10.5	0.00681	17.5
0.00644	17.5	0.00588	10.6	0.00602	5.8	0.00597	9.5	0.00621	17.0
0.00576	17.5	0.00537	9.6	0.00550	5.8	0.00547	9.5	0.00558	16.4
0.00528	15.0	0.00465	9.6	0.00476	4.6	0.00477	8.4	0.00509	15.9
0.00504	12.5	0.00382	9.6	0.00386	3.5	0.00389	8.4	0.00448	14.2
0.00401	10.0	0.00331	8.5	0.00335	3.5	0.00256	6.3	0.00365	12.6
0.00328	6.2	0.00138	5.3	0.00138	2.3	0.00139	5.3	0.00318	12.0
0.00135	3.7							0.00131	9.3

4.2.2 Laboratory Experiments

We designed large-scale experiments to mimic the structure of the canyon-basin system by using a narrow channel that fed into a wide basin with a permeable surface (Fig. 2**a**). With guidance from Prof. Hill and Prof. Hung, I conducted these experiments at the Saint Anthony Falls Lab of the University of Minnesota with the assistance of the research staff, Benjamin Erickson, Richard Christopher, Erik Noren,

doi:10.6342/NTU202204140

Matthew Lueker, and Jim Tucker, and exchange student, Xiaoqiong Jiang. During each experiment, we continuously mixed and discharged clay/water/flocculent mixtures into a funnel mixer, into which we simultaneously input sand at a steady rate, so that they entered the channel well-mixed at the upstream end and flowed down the channel into the basin.

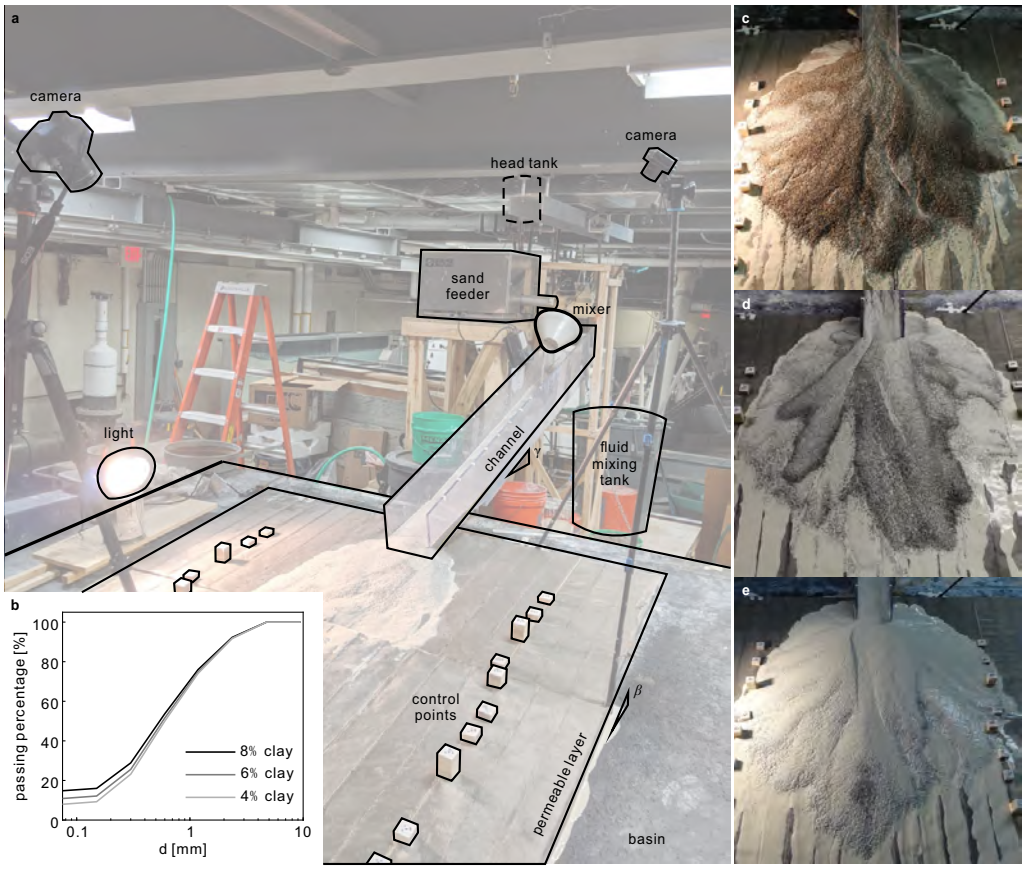

Figure 4.4: **a**, Laboratory set-up and **b**, grain size distribution of our three mixtures (data presented in Tables 4.6). **c-e**, experimental alluvial fans resulting from continuous 15-minute releases with: **c**, (sand: clay: water) = (50: 4: 46) by weight; **d**, (sand: clay: water) = (52: 6: 42) by weight; **e**, (sand: clay: water) = (48: 8: 44) by weight.

For our experimental mixtures, we used angular sand (specific gravity of 2.65, size distribution shown in Fig. 4.4**b**), clay (Kaolinite with specific gravity of 2.65), Polydiallyldimethylammonium chloride (PDADMAC), and water. We note two key details about the mixtures that differ from a typical debris flow to accommodate our experimental design: (1) We use a water content of approximately 44% by

doi:10.6342/NTU202204140

weight, compared with a more typical field-scale water content of 15-30% by weight (Iverson et al., 2011); we required this for instantaneously well mixing the sediments and fluids for sustained flows that mimics long-duration events in the field. (2) We used a small percentage of PDADMAC; we required this to flocculate clay particles, so that the clay would settle more quickly in our scaled-down experimental setting.

Table 4.4: Experiment runs, conditions, and associated video files/slope maps.

Run #	basal boundary	duration	continuous (c) or incremental (i)	flow type	% clay	video file name	Slope map in Fig. 4.5
R1	permeable bed	5 min	i	debris flood	4	V4 & V7	Yes, Fig. S4c
R2	top of run 1 deposit	5 min	i	debris flood	4	V4 & V7	No
R3	top of run 2 deposit	5 min	i	debris flood	4	V4 & V7	Yes, Fig. S4f
R4	permeable bed	15 min	c	debris flood	4	V3	Yes, Fig. S4i
R5	permeable bed	5 min	i	runny debris flow	6	V2	Yes, Fig. S4d
R6	top of run 5 deposit	5 min	i	runny debris flow	6	V2	No
R7	top of run 6 deposit	5 min	i	runny debris flow	6	V2	Yes, Fig. S4g
R8	permeable bed	15 min	c	runny debris flow	6	V1	Yes, Fig. S4j
R9	permeable bed	5 min	i	viscous debris flow	8	V6 & V8	Yes, Fig. S4e
R10	top of run 9 deposit	5 min	i	viscous debris flow	8	V6 & V8	No
R11	top of run 10 deposit	5 min	i	viscous debris flow	8	V6 & V8	Yes, Fig. S4h
R12	permeable bed	15 min	c	viscous debris flow	8	V5	Yes, Fig. S4k

We performed twelve experiments (summarized in Table 4.4) using three different mixtures varying primarily in clay fraction from 4% to 8% (Fig. 4.4**b**, Tables 4.5, 4.6). We initiated two distinct experiments for each mixture over the cleaned permeable surface of the sloped basin. For each mixture, we initiated one experiment over the cleaned bed for which we discharged the mixture continuously for 15 minutes (Figs. 4.4**c-e**) and one experiment over the cleaned bed for which we discharged the mixture continuously for only 5 minutes (e.g., Fig. 4.8**a**). After each of these 5-minute experiments, we performed two additional 5-minute experiments over the previous fan without cleaning down to the previous bed. (e.g., Fig. 4.5**f-h**).

doi:10.6342/NTU202204140

Since our primary data came from photogrammetry after the deposition was halted, this resulted in a total of twelve fan surfaces.

Table 4.5: Varied experimental flow composition and discharge.

Label	Exp run #'s	Sand (w%)	Clay (w%)	PDADMAC (w%)	Water (w%)
		Sand discharge (g/s)	Fluid discharge (g/s)		
Debris flood	R1 - R4	50	4	0.004	45.996
		100	100		
Runny debris flow	R5 - R8	52	6	0.006	41.994
		100	92		
Viscous debris flow	R9 - R12	48	8	0.008	43.992
		100	108		

Table 4.6: Experiment sediment size distribution (plotted in Figure 2 inset) and mixture properties.

	Debris flood	Runny debris flow	Viscous debris flow
Sieve size (mm)	sediment passing rate (%)		
4.75	100	100	100
2.36	92.3	91.9	91.7
1.18	76	74.9	74.1
0.6	53.7	51.6	50
0.3	28.9	25.6	23.1
0.15	16	12.1	9.3
0.075	14.8	10.9	8.0
clay:fluid ratio	0.08	0.12	0.16
clay:sediment ratio	0.074	0.10	0.14
clay:mixture ratio	0.04	0.06	0.08

We prepared the materials to flow in the channel/basin experiment as follows. We filled the sediment feeder (center in Fig. 4.4**a**) and calibrated the output. Separately, we pre-mixed the clay, PDADMAC, and water with the designed ratio in the fluid mixing tank (center right of Fig. 4.4**a**) and pumped the fluid (clay-water mixture) into the head tank (top center in Fig. 4.4**a**). During the experiments we continuously circulate the fluid between the head tank and the mixing tank to assure we maintain a good mixture. To initiate an experiment, we simultaneously released the fluid and sand into a rotating funnel mixer from which they emerged well-mixed and flowed into the inclined channel (top-right center of Fig. 4.4**a**).

doi:10.6342/NTU202204140

The channel was approximately 2m long and 20cm wide and for all experiments was inclined at a slope of 0.3. The sediment mixtures flowed continuously through the channel and into the top center of the basin (approximately 3 m wide by 5 m long and inclined at a slope of 0.118). To mimic boundary conditions in the field which are more porous than a typical basin boundary, we built a "permeable layer" (approximately 10 mm thick, covered by #200 mesh filter screen sheet, and filled with sand) onto which the sediment-fluid mixture flowed. Relatively quickly, fluid left the sediment layer through the permeable layer and, over time, the sediment deposit thickened into a cone-shaped deposit (e.g., Figs. 4.4**c-e**) with channel and lobe-like features as discussed in the text.

We include videos from many of the experiments in open access https://doi.org/10.5281/zenodo.7069689 (legends and contents of the videos are listed in Tables 4.7 and 4.8) to help the reader understand the evolving nature of the flow and deposits, particularly as the boundary conditions change from a porous base to a erodible deposit. We particularly call the reader's attention to the terminology we use referring to the type of the flow (i.e., debris flood, runny debris flow, and viscous debris flow). These are common nomenclatures in the literature but often have overlapping and even non-consistent uses. Initially, the "debris flow nature" of the dynamics are difficult to determine in all cases as the flows appear wide and runny. Nevertheless they show feature common to debris flows such as the largest particles (i.e., sand in this case) suspended on top of the flow in the channel. All flows are wide until an initial deposit is established. Then the flow behavior on the fan evolves from the early sheet flow behavior to the later channelized behavior, most noticeable in the figures (E.g., Fig. 4.5) for the higher clay content cases. For all cases, this channelization is noticeable in the films. Other properties common to debris flows evidenced in these videos are lobe formation.

From the Supplementary Video V1, we can see clear channelization at 0:22, 0:37, 0:44, 0:58, 1:12, 1:30, and 1:49, deposition of lobes at 0:33, 0:55, 1:02, 1:42,

doi:10.6342/NTU202204140

Table 4.7: Legends, Titles, and Contents for Supplementary Videos 1-8

Legend	Title	content
V1	V1C615MinsSideViewacc8640p.mov	Video record (side view) of the experiment process of a continuous (15 minute) flow with 6% clay mixture.
V2	V2C63x5MinsSideViewacc8640p.mov	Video record (side view) of the experiment process of three successive (5 minute) flow with 6% clay mixture.
V3	V3C415minsSideViewacc8640p.mov	Video record (side view) of the experiment process of a continuous (15 minute) flow with 4% clay mixture.
V4	V4C43x5minsSideViewacc8640p.mov	Video record (side view) of the experiment process of three successive (5 minute) flow with 4% clay mixture.
V5	V5C815minsSideViewacc8640p.mov	Video record (side view) of the experiment process of a continuous (15 minute) flow with 8% clay mixture.
V6	V6C83x5minsSideViewacc8640p.mov	Video record (side view) of the experiment process of three successive (5 minute) flow with 8% clay mixture.
V7	V7C43x5minsFrontViewacc8640p.mov	Video record (front view) of the experiment process of three successive (5 minute) flow with 4% clay mixture.
V8	V8C83x5minsFrontViewacc8640p.mov	Video record (front view) of the experiment process of three successive (5 minute) flow with 8% clay mixture.

Table 4.8: Supplementary video contents.

Video legend	Clay content (w%)	Water+ Flocculant content (w%)	Sand content (w%)	Sand discharge (g/s)	Fluid discharge (g/s)	Flow event time scale (min)	View direction
V1	6	42	52	100	92	1 x 15	side view
V2	6	42	52	100	92	3 x 5	side view
V3	4	46	50	100	100	1 x 15	side view
V4	4	46	50	100	100	3 x 5	side view
V5	8	44	48	100	108	1 x 15	side view
V6	8	44	48	100	108	3 x 5	side view
V7	4	46	50	100	100	3 x 5	front view
V8	8	44	48	100	108	3 x 5	front view

1:54, back fill at 1:01-1:08, and gradual avulsion at 0:43, 1:10, 1:18, 1:29, and 1:53. From the Supplementary Video V2, we can see clear channelization at 1:12 and 1:42, deposition of lobes at 1:27 and 1:44, and gradual avulsion at 1:16. From the Supplementary Video V3, we can see clear channelization at 0:12, 0:15, 0:25, 0:27, 0:33, 0:55, 1:21 and 1:38, deposition of lobes at 0.55, 1:01, and 1:37, and gradual avulsion at 0:14, 0:17, 0:35, 0:56, 1:05, 1:34, and 1:44. From the Supplementary Video V4, we can see clear channelization at 0:20, 0:28, 0:35, 0:39, 0:56, 1:14, 1:39, and 1:48, deposition of lobes at 0.35 and 1:10, and gradual avulsion at 0:23, 0:32, 1:02, 1:21, 1:42, 1:56 and 2:04.

doi:10.6342/NTU202204140

4.2.3 Analysis techniques

For the analysis of the field and experimental data, we require high resolution digital elevation models (DEM) for each. We use published field data (Lifton, 2013) that provides data within a resolution of 1m x 1m, with uncertainty in z-direction from 5cm to 35 cm. To reconstruct the topography of the experimental fans, we first took ∼600 images of the surface and of the 40 control points (Fig. 4.4**a**) from multiple viewpoints. Then, we used a commercial software (Agisoft Metashape) which uses a stereo analysis photogrammetry method to build a digital elevation model (DEM) and an orthophoto. By using the large number of control points and photographs for the scale of the fan we obtain a particularly high-precision DEM (2mm x 2mm grid size with uncertainty in z-direction of 1.2mm) (provided as open access data D1-D9).

After obtaining high-accuracy DEMs for the experiments and field fans, we performed additional calculations to build slope maps and slope histograms to eliminate misleading data associated with individual grains. To do so, we first considered all the coordinates at which the 2mm x 2mm grid lines (for the experiments) or 1m x 1m (for the field) intersected with equal height contour spaced at 5mm height intervals (experiments) or 1m height intervals (for the field). Then for each such intersection point on a particular contour, we find the nearest intersection point on the neighboring contour and use the positions to calculate a local slope and temporarily assign it to the downstream neighbor. We do this for every point on every contour. Then we linear-interpolated the slopes onto the original 2mm x 2mm Cartesian grids (experiments) or 1m x 1m Cartesian grids (for the field) and obtained the slope maps as shown in Fig. 4.5 (all experiments and field cases) and in supplemental data file D11-D20 for all experiments and field data (we provide data in open access https://doi.org/10.5281/zenodo.5721569). Since we are only concerned with the slope data on the fan, as indicated above, we used the orthophoto to define the

doi:10.6342/NTU202204140

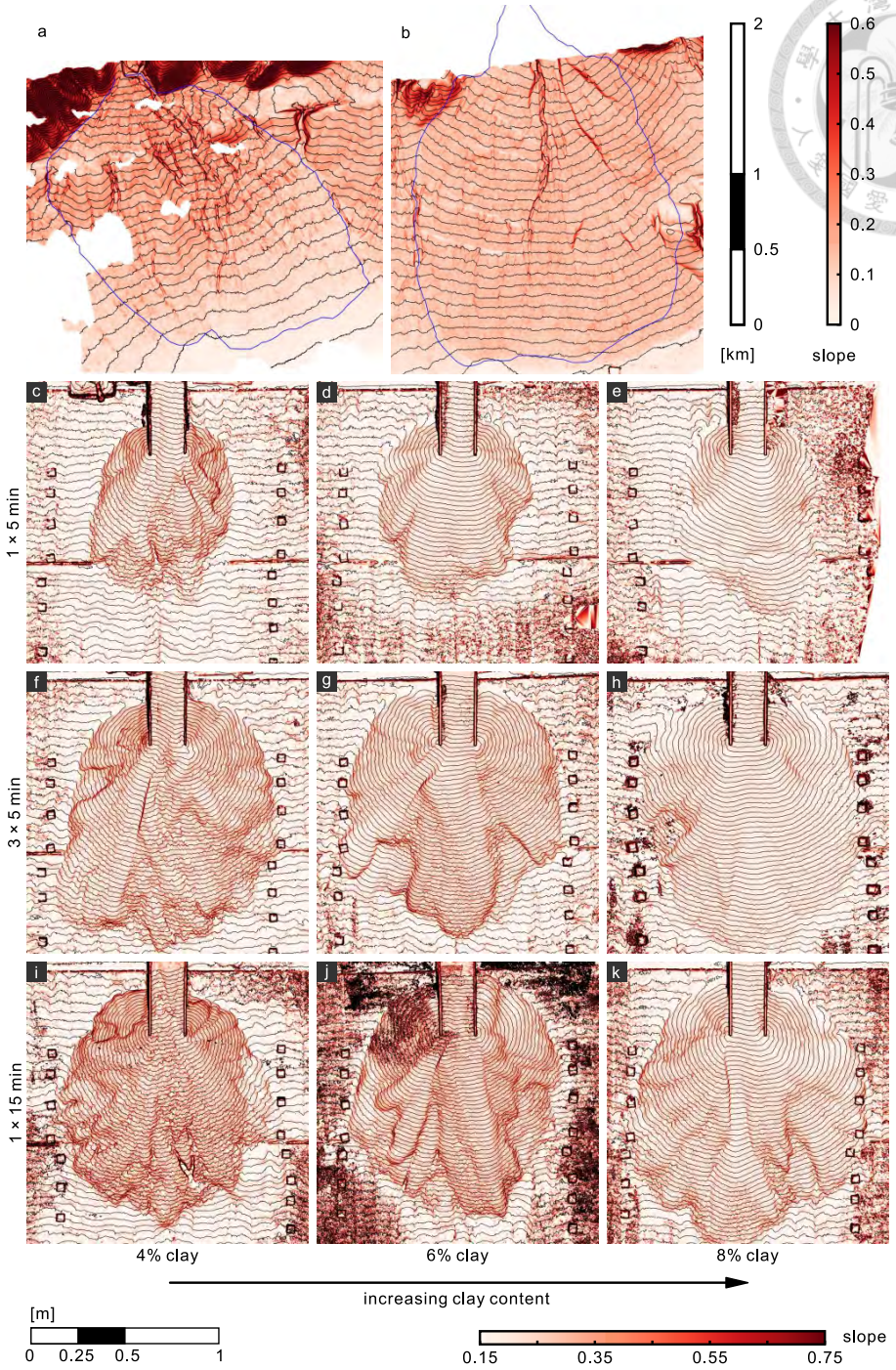

Figure 4.5: Elevation contours and slope map of the fans in the field and experiments (Fig. 3 from the text extended to include all fans we discussed in this paper). **a**, Straight Fan. **b**, Piute Fan. **c-e**, 1 x 5 min run. **f-h**, 3 x 5 min runs. **i-k**, 1 x 15 min run. **c,f,i**, 4% clay. **d,g,j**, 6% clay. **e,h,k**, 8% clay.

fan boundary and cropped the slope data outside of the boundary. Finally, based on the cropped slope data, we calculated the distribution of the slope on the fan (see Fig. 4.6 and Table 4.9, present as boxplots in Fig. 4.8**f**), which provides one

doi:10.6342/NTU202204140

quantitative representation of all slope data.

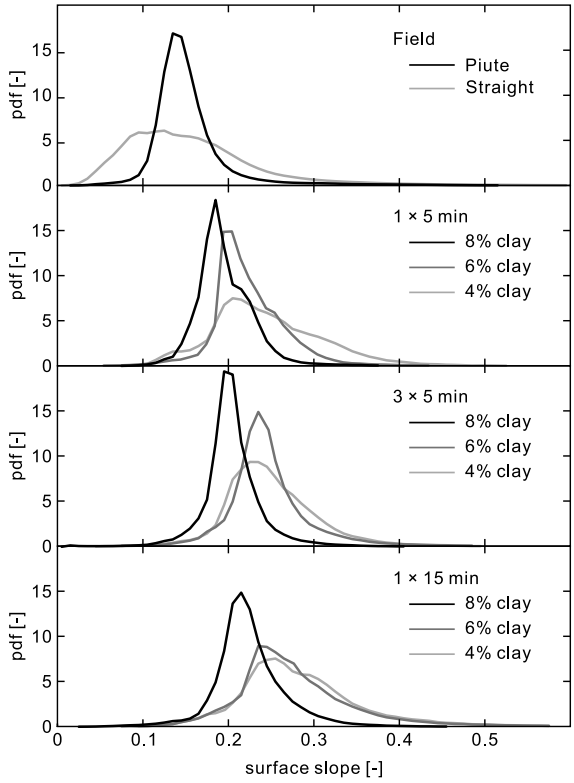

Figure 4.6: Slope distribution from surface of all fans in the field and experiments.

Table 4.9: Slope distribution data from surface of all fans in the experiments. S_i refers to the slope for which i% of the slopes are smaller.

Run #	R1	R5	R9	R3	R7	R11	R4	R8	R12
Duration	1 x 5 min			3 x 5 min			1 x 15 min		
Clay content [%]	4	6	8	4	6	8	4	6	8
S_1	0.1186	0.1268	0.1270	0.1281	0.1431	0.1032	0.1458	0.1468	0.1104
S_5	0.1465	0.1728	0.1508	0.1785	0.1831	0.1537	0.1857	0.1858	0.1675
S_{25}	0.2013	0.1994	0.1764	0.2163	0.2221	0.1892	0.2384	0.2354	0.2027
S_{50}	0.2366	0.2176	0.1904	0.2432	0.2398	0.2020	0.2729	0.2647	0.2198
S_{75}	0.2864	0.2466	0.2140	0.2784	0.2632	0.2186	0.3186	0.3073	0.2431
S_{95}	0.3724	0.2979	0.2516	0.3508	0.3343	0.2690	0.4263	0.4108	0.3013
S_{99}	0.4955	0.3686	0.3294	0.4456	0.4361	0.3844	0.5834	0.5802	0.3778

To quantitatively assess local surface irregularities (for example, associated with channels and lobes), we draw from what many call the *granular physics* literature Hill et al. (1999, 2004) and calculate what is called a measure *complexity* (N_b). We turn back to individual contour lines from the slope plots detailed in Fig. 4.5. As a representation of the morphology of the fan, we choose several equally spaced

doi:10.6342/NTU202204140

contour lines that span the majority of each fan. Then, we define a dimensionless number to examine the shape and bumpiness of each elevation contour of the fans. We define $(\theta_{\max}, \theta_{\min})$ as the maximum and minimum angles for which the contour that is continuous from one edge of the fan to the next (Figs. 4.7**a**,**b**). We divide each contour into 6 overlapping sections which bounded by $(\theta_{L,k}, \theta_{R,k})$, where $\theta_{L,k} = \theta_{\min}+(k-1)(\theta_{\max}-\theta_{\min})/10$ and $\theta_{R,k} = \theta_{\max}-(6-k)(\theta_{\max}-\theta_{\min})/10$ for $k = 1, 2, ..., 6$. For each section, we calculate a complexity number as

$$N_b = \frac{P^2}{2A\Delta\theta}: \quad P = \int_{\theta_L}^{\theta_R} r\, d\theta, \quad A = \int_{\theta_L}^{\theta_R} \frac{1}{2} r^2\, d\theta, \quad \Delta\theta = \int_{\theta_L}^{\theta_R} d\theta, \tag{4.1}$$

In these equations, r references the polar coordinate of each vertex of a contour with the origin located at the apex of the fan. We note that in some cases, the contour is segmented because of missing data in the field (e.g., Fig. 4.5**a**), the value of the contour length P, the area A, and the opening angle $\Delta\theta$ are the summation of the integrations in each segment.

$$N_b = \frac{(\sum P_i)^2}{2\sum A_i \sum \Delta\theta_i}; \quad P_i = \int_{\theta_{L,i}}^{\theta_{R,i}} r\, d\theta, \quad A_i = \int_{\theta_{L,i}}^{\theta_{R,i}} \frac{1}{2} r^2\, d\theta, \quad \Delta\theta_i = \int_{\theta_{L,i}}^{\theta_{R,i}} d\theta \tag{4.2}$$

For each fan, we define the apex slope $\tan\alpha$ by the average deposit surface gradient from where 20 cm upstream the channel end to the channel end. Next, we compute a fan-specific $z = 0$ where the plane of the bottom (permeable) boundary (slope $\tan\beta = 0.118$) and an inclined plane defined by the fan apex height (z_{Apex}) and apex slope $\tan\alpha$ (see Fig. 4.7**a**, right column) intersect with each other. Then, we calculate N_b for several contours whose elevation $z_c = 0.2H, 0.3H, ..., 0.8H$, where fan height $H = z_{Apex}$ based on the fan-specific $z = 0$. For interpretation of the values of N_b, we note that for a circle segment, $N_b = 1$, and both bumpiness and the distortion of curve shape will increase N_b. However, we also note that the shape of contours will be influenced by the inflow channel while closing to it. To separate the

doi:10.6342/NTU202204140

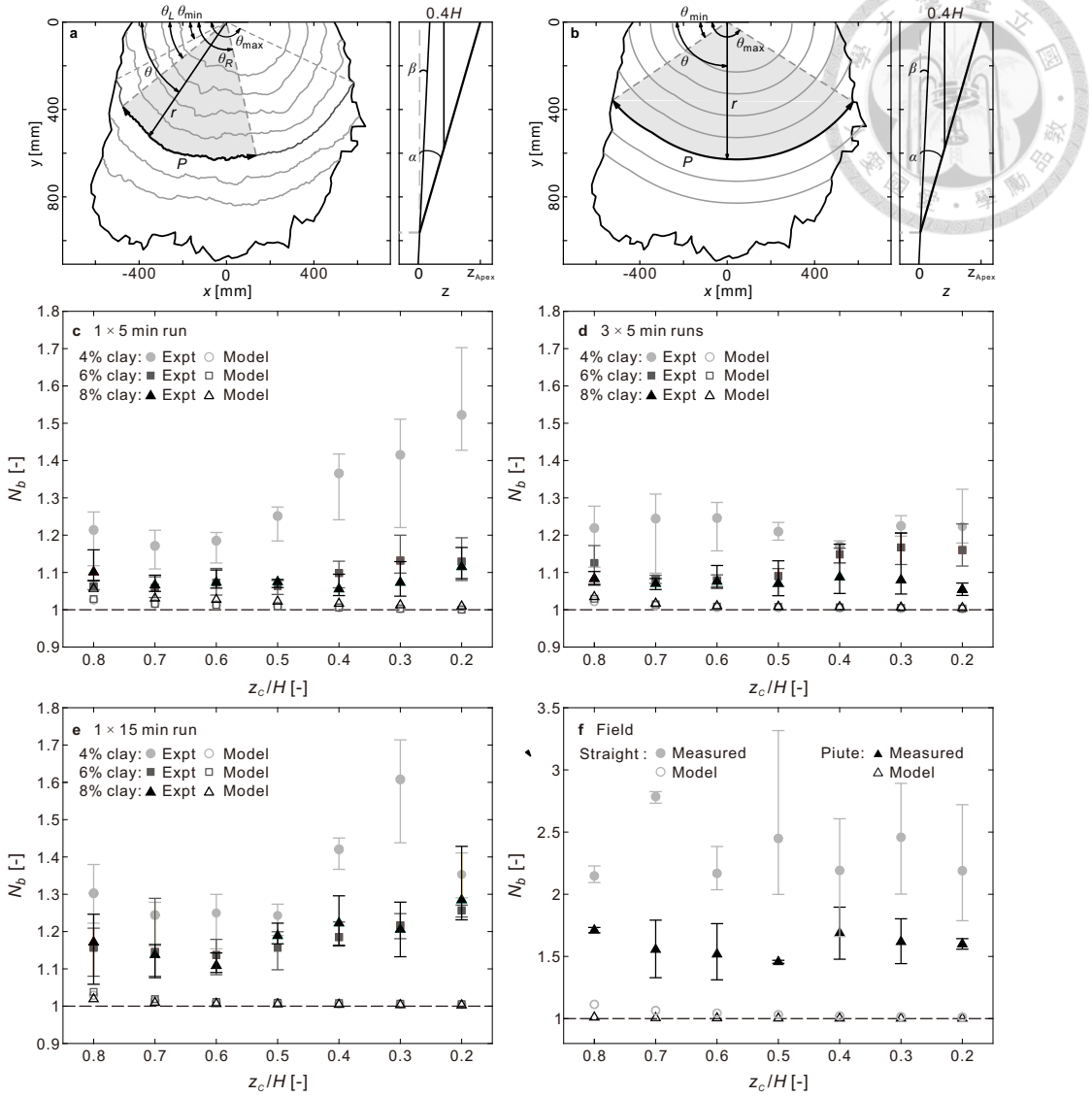

Figure 4.7: Complexity measurements. **a,b**, illustrative contours and complexity-related variables from **a** the experimental fan with 4% clay and 3 x 5 minutes runs. **b**, a constant-slope modelled fan using the same fan apex position and median slope. **a-b**, Left panels: top view showing each fan boundary (black outer line); contours of elevation for z_c from $0.2H$, to $0.8H$, where $H = z_{apex}$ (gray lines).**a-b**, right panels: center vertical cross-section (with distorted z scale). Black lines: bed plane of slope $\tan\beta$ and approximate fan surface of slope $\tan\alpha$; dashed line: horizontal plane of $z = 0$; bold line: contour plane z_c =$0.4H$. **c-f**, complexity measurements from the experimental and field alluvial fans, modeled and measured, as noted in the upper left corners. open symbols: modelled fans; closed symbols: mean N_b of the measured fans. Error bars represent range of N_b values for 6 smaller sections of each contour of the measured fans and 2 smaller sections for each field fan.

effects of the inflow channel from the real surface roughness, we propose a model fan that contains only a smooth and constant-slope surface for each actual fan. With the

doi:10.6342/NTU202204140

constant slope, an arbitrary contour of a modelled fan will always consist of three segments: a straight line segment of the length equal to the inflow channel width and two circular arcs (e.g. Fig. 4.7**b**). We calculate N_b for corresponding contours on both actual fans and modelled fans (closed and open symbols respectively in Figs. 4.7**c-f**). Apart from the influence of the inflow channel, if the length of a curve segment has irregularities such as occurs on our fans for larger channel/lobe variations or greater numbers of channels or lobes, then N_b increases (as P increases for relatively little change in A).

4.3 Field-scale Studies: Particle Properties and Channel Avulsion Signatures

In this section, we discuss the similarities and differences of Straight and Piute Fans on the west side of the White Mountains (California, USA) (Figs. 4.1**b-d**). Evidence of a predominance of debris flows in these fans include: large boulders that litter both surfaces, toe-deposits and levees, and stream cuts that reveal poorly sorted thickly layered deposits (Figs. 4.1c-d). Additionally, their relatively high slopes and catchment area roughness numbers suggest that these fans were primarily built by debris flows (Table 4.1). Their proximity to one another suggests they developed under similar climatic conditions.

Yet even with these similarities and their proximity, the two fans exhibit substantial differences. From a distance, even their coloration differs, likely due to different mineralogical constituents (Crowder and Sheridan, 1972) (Fig. 4.2). Upon closer investigation, these fans differ in what we might call their *channelization complexity*. Straight fan is riddled with intersecting overlaid channels up to 2 to 4 meters deep, while Piute Fan has relatively few surface channels, and they are considerably deeper (Figs. 4.1**c-d**). Several samples (Fig. 4.1**b**, Fig. 4.3, and Tables 4.2,4.3) from the active channel levees on Straight Fan indicate that recent flows down Straight

doi:10.6342/NTU202204140

fan deposited, roughly, an even distribution of sand, silt, and clay with insignificant variation down-channel. In contrast, the sample we collected from near Piute's fan apex and observations of qualitatively similar deposit size distributions downslope indicates a much higher concentration of silt than that of clay or sand.

Though Piute sample is limited, we were inspired by the marked differences with all samples from Straight Fan as well as distinctions in the lithologies of the two fans (Crowder and Sheridan, 1972). The minerology of the catchments are associated with differences in particle strength and, subsequently, mechanical weathering rates. Based on these observations and measurements, we hypothesize that apparent differences in both the fine particle content and lithology could indeed drive differences in fine content, thereby influencing system-wide behaviors similar to that found by Man and Hill (2021); Man et al. (2022). In this case, we suspect the fine particles may affect both the rheology of the flows as well as erosion rates, thereby affecting the balance between down-fan avulsions and in-channel persistence. These considerations motivated more systematic investigations made possible by laboratory basin-scale physical experiments.

4.4 Laboratory Experiments

In this section, we discuss our observations in the laboratory experiments. We note several commonalities from one run to the next, independent of mixture content, basal conditions, and depositional time (apparent in Supplementary Videos, Tables 4.7-4.8). In all cases we observed the dynamics evolve over time from an initial, roughly radially-symmetric depositional stage that established a relatively uniform erodible bed to a break from symmetric to discrete self-channelizing flows that frequently avulsed primarily by one of two processes. In one process, a more frequently-referenced down-channel blockage (Densmore et al., 2019; de Haas et al., 2015a; Herbert, 2021), led to sudden channel abandonment (e.g. Supplementary Video V1, 1:07-1:13). In the other process, an apparent up-channel dominated pro-

doi:10.6342/NTU202204140

cess, erosional stresses on one channel bank gradually moved the channel sideways resembling channel-bank migration (e.g. Supplementary Video V1, 1:13-1:20 and 1:29-1:35). During the latter phase we observed deposition of the flow into discrete lobes near the edge and farther upslope. Other typical debris flows features we observed included segregation of the "larger particles" (sand) outward onto levees and to the edges of depositional lobes. After deposition was complete, natural coloration helped distinguish levees from in-channel deposit, more difficult to observe during flows, perhaps because of the small experimental scales.

There were also notable differences based on: boundary conditions, flow mixtures, and what might be called "timescales". For the flows initiated over the cleaned permeable bed, the flow deposited in relatively radially symmetric layers over the base (and independently of the timescale of the well-known "roll waves" (Zanuttigh and Lamberti, 2007), ongoing in the channel). In contrast, the shorter runs we initiated over previously-deposited 5-minute flows (Runs 2,3, 6, 7, and 10, 11) appeared at first to follow the partially drained channels, i.e., asymmetrically. Shortly after this initial stage, the flow reset the channels before proceeding to re-channelization stage, avulsion, and channel migration. Increasing clay content changed the apparent time scales of channelization and avulsions (e.g., Supplementary Video V1, V3, V5 and Figs. 4.8**c**-**e**). Our high clay-content flows avulsed more slowly, giving rise to relatively few channels and lobes compared to their low-clay counterparts. Our low clay-content flows more frequently avulsed prior to reaching the fan edge and did so quickly, giving rise to more channels and a bumpier final deposition morphology. Also, the higher-clay flows created wider channels than the lower-clay flows. The difference between a 15 minute deposition formed from continuous flows from that formed from flows was also evident in fan morphology, relatively independent of mixture. A fan built over a continuous (15 minute) flow event produced a more continuous channelization evolution than one built from the same material over three successive (5 minute) flow events. For the latter, each time we terminated the flow,

doi:10.6342/NTU202204140

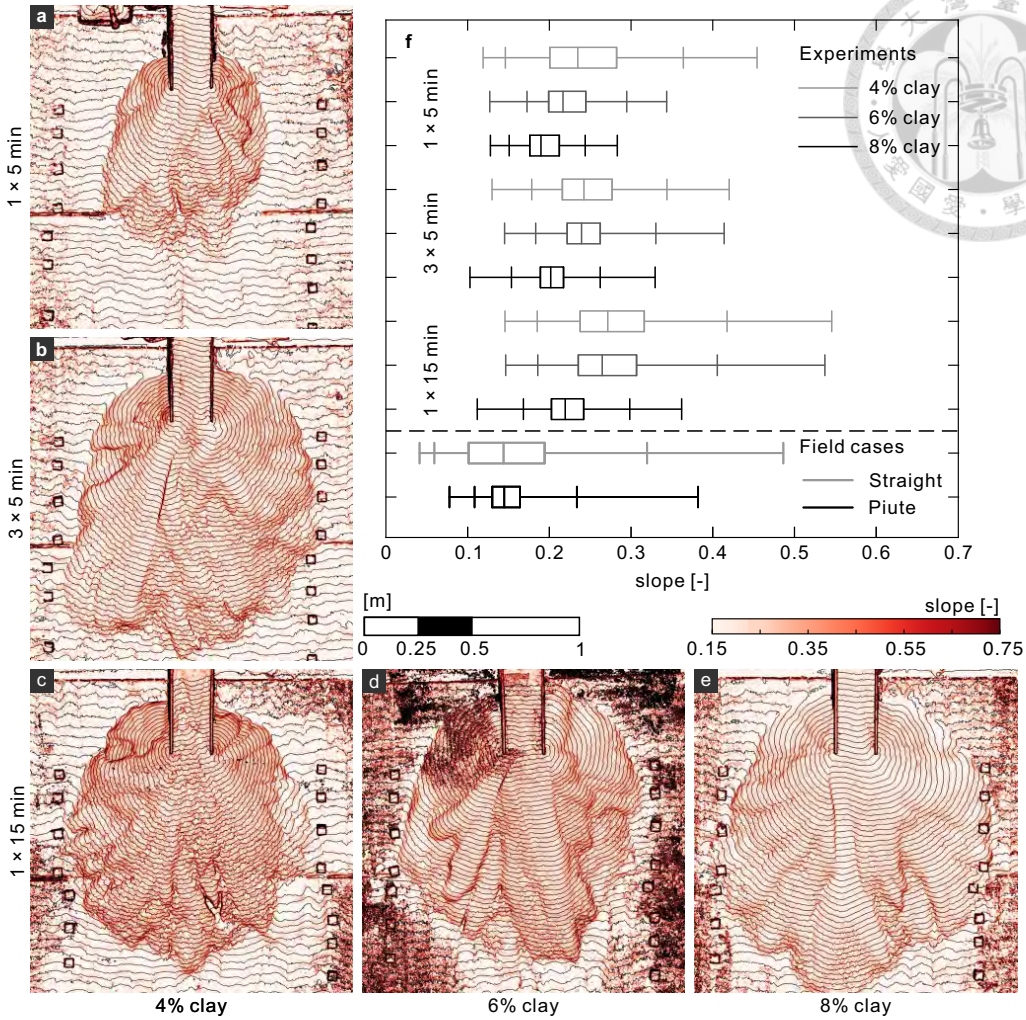

Figure 4.8: **a-e**, Elevation contours and slope maps of experimental fans. Contour line spacing represents 5 mm elevation changes. **a-c**, shows results for runs of constant clay content performed for different discharge timescales: **a** one 5-minute flow **b** three successive 5-minute flows **a** one 15-minute continuous flow. **c-e**, results for runs of one 15-minute flow and clay contents of **c** 4%, **d** 6%, and **e** 8%. (More in Figs. 4.5-4.6). **f**, Boxplot for the slope distribution of the fan surface in 9 representative experiments and the 2 field cases we studied. The boxplot displays the dataset based on the 1st, 5th, 25th, 50th, 75th, 95th, and 99th percentiles (Table 4.9).

fluid drained from the fan so that restarting the flow first served to re-wet the fan surface, partially resetting the channels (Compare Supplementary Videos V1,V2), giving rise to a final fan surface with fewer lobes and channels (compare Figs. 4.8**b** and **c**), apparently less relief over the fan surface.

doi:10.6342/NTU202204140

4.5 Quantitative analyses

To evaluate effects of boundary conditions, clay content, and intermittency on fan deposit surfaces and quantitatively evasive measures of channel numbers, we consider certain slope statistics (Figs. 4.6 and 4.8**f**) and the measure of *topographic complexity* (Fig. 4.7).

We consider three idealized fan morphologies to build our intuition of slope statistics: (1) Single-slope morphologies represent alluvial fans to first order approximation (Staley et al., 2006; Lin et al., 2009; de Haas et al., 2015b) which yields a single delta function for their slope distributions. (2) Near-single-slope morphologies with topographic depressions (de Haas et al., 2018) (e.g., slope variations) yield finite, narrow slope distributions. (3) Deposit morphologies edged by steep slopes, such as Bingham or Herschel-Bulkley fluids (historically used to approximate debris flows (Kaitna et al., 2007)) would (Coussot et al., 1996), give rise to a positively skewed slope distribution. All of our experimental fans exhibited some of each of these characteristics (Fig. 4.8**f** with relatively narrow central (25% to 75%) boxes, skewed with a long positive tail.

We found that the experimental fans built with higher clay contents had lower median slopes and less skewness (representing smoother surfaces, fewer channels, and/or fewer lobes). For any particular clay content we found the fans built continuously (for 15 minutes) exhibited the larger median slope, wider slope distributions and larger skewness, (representing bumpier surfaces, more channels and/or more lobes). Similarly, we found Straight Fan has a wider slope distribution than Piute Fan, and a similar median slope and skewness. Since Piute has significantly more silt than Straight but a similar clay contents, this is relatively consistent with our experimental results. To quantitatively assess local surface irregularities (for example, associated with channels and lobes), we calculate the *complexity* (N_b) as described above in section 4.2.3. We plot these results with corresponding contours

doi:10.6342/NTU202204140

for single-sloped model fans based on each experimental apex and apex slope in Fig. 4.7. For the model fans, $N_b \sim 1$ and approaches 1 down-fan. For the experiments, N_b increases with apparent surficial bumpiness (Figs. 4.8**a-e**). In this regard, we find complete consistency between N_b and slope variability (Fig. 4.8**f**). That is, for lower clay content and longer continuous flow time, we obtain both the largest N_b values and the widest slope distributions. N_b also provides dependence on distance downslope. For the continuous 5 min. and 15 min. runs *only* using 4% clay (Figs. 4.7**c,e**) the relative complexity increase up-fan is statistically significant. For incrementally-deposited fans (Figs. 4.7**d,f**) there is no such identifiable downslope trend. The field fans also do not appear to exhibit this consistent upstream complexity dependence, consistent with several flows built over time. As with our experimental fans, the field fan with the higher fine particle content (straight) has a higher N_b value.

4.6 Conclusion

To summarize and more fully contextualize our findings, we first refer back to our remarks in the introduction regarding distinctions among fans built under different climatic and other boundary conditions. We noted in some cases debris flows explored the entire fan in a single event, and, in others, debris flows were restricted to a single channel or region of the fan. Our experimental fans – both incremental and continuous – developed from experimental debris flows that built and explored their alluvial surface in each event, not unlike those reported in Taiwan Laonong River Valley, Fig. 4.1**a**) (Hsieh and Capart, 2013; Lo, 2017; Lo et al., 2018). We hypothesize, then, that analysis of the Pu-tan-pu-nas fan, the Yu-Shui fan, and other fans that are relatively young or whose deposit is periodically washed away (e.g., as in the Taiwanese debris flow deposits) would reveal more interesting downslope complexity than the White Mountain Fans from our preliminary field work.

Perhaps surprisingly, our preliminary measurements and analysis from the White

doi:10.6342/NTU202204140

Mountain fans are consistent with our measures of fine-particle-dependence of slope statistics and topographic complexity. That is, in these field cases, the Straight fan, with its relatively small percentage of fine particles, exhibited a wider slope distribution and a higher topographic complexity than Piute Fan. We find this similarity with our experimental results surprising for two reasons. First, records indicate that their flow scale compared to that of the fan development is much shorter than those of our experiments, i.e., single flow events are restricted to relatively small regions of their fans. Second, the higher fines content on Piute (compared to Straight) pertains to silt rather than clay. Silt and clay particles are differently in their settling velocities and relative interparticle interactions and thus we suspect that they would affect the larger-scale flows in which they travel distinctly. These results bring to mind questions about scaling effects of the small particles in the overall size distribution along with their larger counterparts that we have begun to investigate using experiments of different sizes as well as alluvial fans that developed under a wider variety of climatic conditions and the limited range of lithologies as those described in this paper.

To wrap up, we suggest that the data and analyses we present in this paper provide a more complete foundation onto which we as a community can build a better framework for how fine particle content can influence debris-flow driven morphology on alluvial fans as well as their associated hazards. In addition to quantitative links between grain-size, intermittency, and channelizations, these results provide insights to design experiments more in-line with particular field-scale fan development. Additional tools will likely arise from investigations into micro-scale dynamics interparticle dynamics including the physical processes by which fine particles such as silt and clay affect larger-particle interactions and, cumulatively, influence macro-scale fan morphologies. New computational methodologies and other inspiring insights are becoming increasingly applicable from what we might consider the sibling field "granular physics" i.e., the study of how particle scale properties and interactions

doi:10.6342/NTU202204140

influence macroscopic behaviors in particle-flows and in particle-fluid-flows (Man et al., 2022; Yohannes and Hill, 2010; Tripathi and Khakhar, 2011; Trulsson et al., 2012). These and other advancements in particle-rich geomorphology and granular physics (Johnson et al., 2012; Deshpande et al., 2021) show exciting promise for a richer understanding, necessary for tackling complex problems in our natural and human infrastructure in this time of dramatically changing climates.

doi:10.6342/NTU202204140

Chapter 5

Conclusion

5.1 Summary

This thesis aimed to combine computations with observations to improve understanding of the aggradation behavior of alluvial fans and associated risks. Three specific aims included:

1. To reconstruct past alluvial fan morphology and predict alluvial fan morphology and assess associated hazards on a long time scale.

2. To predict the quasi-static evolution of fan morphology including local snout-like features.

3. To investigate the influences of flow composition and time scale on the fan morphology and channelization.

In this thesis, I developed two computational models and conducted field and experiment studies to address these aims. Here, I first summarize the main conclusions. Then I discuss the common alluvial fan morphology and morphodynamics features and their influencing factors of them. Next, I discuss the contribution, application, and limitations of the methods proposed in this thesis. Finally, I propose future works for alluvial fan morphology and morphodynamics and other geomorphic systems where we may extend the models and study methods in this thesis.

5.2 Main conclusions

The major findings of the thesis include:

doi:10.6342/NTU202204140

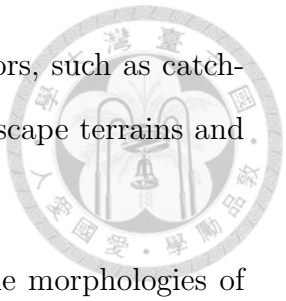

- Alluvial fan morphologies are influenced by numerous factors, such as catchment lithology, flow discharges and compositions, and landscape terrains and forcing from the surroundings **(Chapters 2-4)**.
- Alluvial fan morphologies in longer time scales, such as the morphologies of ancient fans, the morphologies formed over a sustained event or multiple incremental events can be approximated described by surfaces of revolution **(Chapter 2)**.
- Morphodynamics of alluvial fans in short time scales may include channelization and avulsion processes **(Chapter 4)** and snout-shaped deposit **(Chapter 3)**.
- Regardless of the channel patterns, quasi-static morphology of aggrading fans can be simulated by a slope-constraint diffusion process **(Chapter 3)**.
- Critical slopes of fan aggradation depend on the constitutive laws and fan morphology itself **(Chapter 3)**.
- Considering channelization and avulsion processes, fan morphology possesses a range of surface complexity, which is influenced by flow compositions and event time scales **(Chapter 4)**.

5.3 Alluvial fan morphology and morphodynamics features and influencing factors

Alluvial fan morphology can be considered in different perspectives. Looking at the broad scale regardless of the local structures, an alluvial fan tends to possess a similar surface slope over the fan surface (Chapter 2). Looking at contour maps, each elevation contour of alluvial fans tends to have similar space to adjacent contours at different locations. The average space between contours may maintain a similar value or increase downfan, especially for large-scale fans. The average fan slope are

doi:10.6342/NTU202204140

affected by the area and effective slope of upstream catchments (Melton, 1965; Lin et al., 2009), flow discharges and compositions (Takahashi, 1991; Whipple et al., 1998; Armanini et al., 2005), and the interactions with the trunk river (Leenman and Tunnicliffe, 2020; Zubrycky et al., 2021). The decreasing slope downfan is rather affected by the reduced sediment load (Drew, 1873; Parker et al., 1998) and grain size fining (Blissenbach, 1952; Hooke, 1968; Parker et al., 1998; Stock et al., 2008). These fan morphologies on a broad scale can be modelled using surfaces of revolution. The surfaces may be as simple as a truncated cone, but may also exhibit complex shapes when interacting with other fans or surrounding terrains. For example, when building along with spurs, terraces, and islands, the fan deposits would bend around the terrains, leading to elevation contours with higher curvatures. When intersecting with other fan surfaces, clear weld lines would form with regional lows.

When looking at a closer scale, alluvial fan surfaces may exhibit kinds of local structures, such as channels due to debris flows or stream flows (Chapter 4), margin deposition from side gullies (Chapter 2), snout-like lobes or fan toes (Chapter 3, 4), and cliffs along truncated toes due to trunk river incision (Chapter 2). Among them, the formation of the snout-like margins of lobes or toes may be due to the cohesion of the materials (Coussot et al., 1996). We can use the corresponding constitutive laws to decide the critical slope of the deposits and to model the formation of the fans with these snout-like structures by a slope-constraint diffusion process.

When the alluvial fans develop, the flows may self-channelize and the channels may avulse (gradually or suddenly change directions). The size, slope, and avulsion frequency of the channels are influenced by flow compositions, such as the fine fraction (Chapter 4), the presence of boulders (Beaty, 1963; D'Arcy et al., 2017), the grain size distribution of the coarse particles (Tsunetaka et al., 2021), and flow event time scales (Chapter 4) or the flow event magnitudes and sequences de Haas et al. (2018). The channelization and avulsion processes increase the surface complexity of the fans. They may also lead to variations between different azimuthal

doi:10.6342/NTU202204140

directions in the short-term, but in the long-term, the avulsion processes would tend to compensate for the variations (de Haas et al., 2018; Densmore et al., 2019). In addition to the self-channelization and avulsion of debris flows on the fan surface, the reworking of stream flows and the incision of trunk river can also lead to great impacts on fan morphology and morphodynamics that are beyond the scope of this thesis (Zubrycky et al., 2021).

In sum, many factors may cause variations in the morphology and morphodynamics of alluvial fans; it is important to first identify the key scale for a question, such as interpretation of topography data and hazard assessment for villages or infrastructure. For example, for the reconstruction of ancient fans and predictions of long-term fan morphology and hazards, local variations on the fan surface and the dynamic process are less important. In these scales, detailed hydrology conditions are also rarely available. Therefore, adopting the simplified model for constant-slope and concave fans may be more appropriate. On the other hand, to assess short-term hazards, the evolution of the channel/lobe structures on the fan surfaces becomes relevant. More detailed investigation and assessment of the morphodynamics over finer scales are required. Then, it becomes necessary to identify the impact factors, such as lithology, the grain size distribution of source materials, hydrology conditions, and forces from the surrounding landscape.

5.4 Contribution, application, and limitations of the methods

This thesis proposed two computational models, one focusing on static global fan morphology and the other one focusing on quasi-static fan surface evolution including local features. Both models exploit tools developed previously but use them in novel ways and on new problems. Both models were validated with exact solutions in idealized cases. The performance of the models then depends on the reasonability

doi:10.6342/NTU202204140

of the model assumptions and the efficiency of model computations.

The first model (Chapter 2) adopts global slope assumptions, either constant or decreasing slope along elevation, and, based on the assumption, transforms three-dimensional morphology problems into a sequence of two-dimensional visibility polygon problems. The resulting model has high efficiency for simulating static fan morphologies. It may not suitable to describe the details of the fans with high variations in local regions or along different azimuthal directions, but it still has broad applications in topography data interpretation, ancient fans reconstructions, fan evolution predictions, and associated hazard assessments. The efficiency and accuracy of this model mainly depend on the contouring algorithm adopted in the model. Therefore, adopting or developing a faster and/or more accurate contouring algorithm would be a good target to improve the performance of this model.

The second model (Chapter 3) simulates fan aggrading morphodynamics with the restrictive local slope control assumption using the Control Volume Finite Element Method (CVFEM). The model can incorporate the rheology model applicable to cohesive and/or frictional materials and reproduce the snout-shaped toes, the trailing slope observed away from the toes, and other local features like cusped margins and weld lines, and saddle points on the weld lines. Nevertheless, the model is based on isotropic diffusion and is not applicable to simulate phenomena with dominating directions, like channelization and formation of levees of lobes. Many other effects that can cause or contribute to the formation of steep snouts in field or experiments, such as pore particles sorting and pressure loss at the front or along the margins of debris flows (e.g. Iverson, 1997; Iverson and Vallance, 2001; Savage and Iverson, 2003; Iverson et al., 2010; Gray, 2018) and the frictional hysteresis of the angular sand particles (e.g. Félix and Thomas, 2004; Mangeney et al., 2007; Edwards et al., 2017; Rocha et al., 2019; Edwards et al., 2019), are not included in the model. The model performance mainly depends on the computation meshes. Increasing mesh resolution not only increases the total mesh number but also reduces the maximum

doi:10.6342/NTU202204140

stable time step, causing a substantial increase in computational cost. Currently, the model is running with matrix calculation in Matlab environment. Rewriting the model to for loop calculation with parallel computation in other environments like Python may be a good strategy to improve the model.

These two proposed models are designed to simulate fan morphology with known aggrading volumes. However, when applying to hazard mitigation problems, the event volume is also a variable needed estimation. The event volume estimation is beyond the content of the thesis. Nevertheless, the models in the thesis can help to collect historical data by reconstructing ancient fans. Future works can be committed to developing a stochastic model for fan volume evolution and estimation based on the historical data.

In addition to the computational models, this thesis also used laboratory experiments and field data to investigate the alluvial fan morphology and morphodynamics (Chapter 4). The experiment system is novel and can provide sustained debris flows that can produce alluvial fans with continuous channelization and avulsion dynamics. As a result, many common features observed in field, such as erosional and depositional channels, lobes with steep margins, and avulsion processes, were reproduced in the laboratory and investigated in detail with various operational variables. Nevertheless, currently, the operational variables of the experiments were limited to the clay content of the flows and the flow time scales. Many other factors that may influence the formation and evolution of the fan morphology, such as upstream chute slope, basal boundary condition, and the presents of silt and large particles, were not considered. Besides, the evolution of the fan morphology and morphodynamics were only recorded by videos. Topography data were limited to the terminal fan topographies. Therefore, there was no quantitative data for the dynamic channelization and avulsion process.

For the field study, this thesis collected published Digital Elevation Model data (Lifton, 2013) and previous grain size analysis data (Mullenbach, 2018) of two fans

doi:10.6342/NTU202204140

in Owens Valley, California, USA. This thesis proposed a new method to quantify the surface complexity of the topography data and linked the analysis results to fine particle size distribution. Nevertheless, the data collected in this thesis were limited. The completed data set only covered two alluvial fans, and the number of sampling sites and the size range (¡2mm) for the grain size analysis were also limited. The analysis results are informative; however, for validation, more data are needed.

When comparing experimental and field fans, we find effects of different fine content (clay in experiments and silt in field) have similar trends. However, clay and silt have significantly different properties. The comparison and connections between the field observations and experiment results are therefore not straight forward. More detailed investigation including scale effects are required.

5.5 Future works

The above results show that studies on alluvial fans can continue through various avenues. For field studies, increasing the number of study sites, sampling locations, and ranges of analyzed grain size will provide more reliable information. Including study sites under various climates can help to explore and validate the influences of different factors. For example, collecting and comparing data from fans on ice formation, which is impermeable, will help the study of the effects of basal and drainage conditions. Collecting other types of data, such as stratigraphic records, can also help to understand the fan formation history and channelization/avulsion processes.

For laboratory experiments, developing techniques to acquire real-time measurements of dynamic topography is important for quantitatively analyzing the morphodynamic processes through the evolution of alluvial fans. Using multiple cameras to photograph the fans from distinct view angles and applying three-dimensional photogrammetry techniques may be a way to achieve this aim. Developing measurements for real-time surface velocity fields can help to quantify the flow conditions

doi:10.6342/NTU202204140

on the other hand. Adopting the particle image velocimetry or particle tracking velocimetry methods may be a way to do this. After building the new measurement techniques, the experiments can also be conducted with various operational factors, such as systematically adding and changing ratios of silt and boulders (coarse sand) in the flows, adjusting the shape and slope of the upstream chute, and changing basal permeability conditions.

For the computational works, the models proposed in this thesis cannot simulate the channelization and avulsion processes. The second model based on the control volume finite element method (CVFEM) has the potential to be extended to achieve this need. Incorporating the anisotropy diffusion process and stochastic process into the CVFEM model may help to simulate the depositional channels. Incorporating different critical slope and flow depth control assumptions in the CVFEM model may realize the simulation of debris flow entrainment/incision and sidewall erosion. The combination of the methods may greatly improve the model's ability in the simulations of fan morphodynamics.

The CVFEM model could possibly be extended to more general processes or other morphodynamic systems, such as the propagation of deltas and dunes, the evolution of canyon-fan systems, and the dam failure process. Similarly, the first model that based on the visibility polygon method could also be extended to other geomorphic systems. For example, turning the model upside down may be a way to simulate mountain sidewall erosional morphology and predict/assess sediment sources in upstream catchments. Besides, extending the model by considering not only point apex(sink) but also linear or curved apex(sink) may help to improve the performance and scope of the model.

doi:10.6342/NTU202204140

Bibliography

Ahmed, S. A., Buckingham, R., Gremaud, P. A., Hauck, C. D., Kuster, C. M., Prodanovic, M., Royal, T. A., and Silantyev, V. (2004). Volume determination for bulk materials in bunkers. *International Journal for Numerical Methods in Engineering*, 61:2239–2249.

Al-Farraj, A. and Harvey, A. M. (2005). Morphometry and depositional style of Late Pleistocene alluvial fans: Wadi Al-Bih, northern UAE and Oman. *Geological Society, London, Special Publications*, 251(1):85–94.

Armanini, A., Capart, H., Fraccarollo, L., and Larcher, M. (2005). Rheological stratification in experimental free-surface flows of granular–liquid mixtures. *Journal of Fluid Mechanics*, 532:269–319.

Armanini, A., Fraccarollo, L., and Rosatti, G. (2009). Two-dimensional simulation of debris flows in erodible channels. *Computers & Geosciences*, 35(5):993–1006.

Asano, T. (1985). An efficient algorithm for finding the visibility polygon for a polygonal region with holes. *IEICE TRANSACTIONS (1976-1990)*, 68(9):557–559.

Asano, T., Asano, T., Guibas, L., Hershberger, J., and Imai, H. (1986). Visibility of disjoint polygons. *Algorithmica*, 1:49–63.

ASTM D7928-17 (2016). Standard Test Method For Particle-Size Distribution (Gradation) Of Fine-Grained Soils Using The Sedimentation (Hydrometer) Analysis. Standard, ASTM International.

Baliga, B. and Patankar, S. (1980). A new finite-element formulation for convection-diffusion problems. *Numerical Heat Transfer*, 3(4):393–409.

doi:10.6342/NTU202204140

Baliga, B. and Patankar, S. (1983). A control volume finite-element method for two-dimensional fluid flow and heat transfer. *Numerical Heat Transfer*, 6(3):245–261.

Bartelt, P., Bieler, C., Bühler, Y., Christen, M., Deubelbeiss, Y., Graf, C., McArdell, B., Salz, M., and Schneider, M. (2017). *RAMMS – Rapid mass movement simulation, A numerical model for debris flows in research and practice, User Manual v1.7.0, Debris Flow*. WSL Institute for Snow and Avalanche Research SLF.

Beaty, C. B. (1963). Origin of alluvial fans, White Mountains, California and Nevada. *Annals of the Association of American Geographers*, 53(4):516–535.

Berger, C., McArdell, B. W., and Schlunegger, F. (2011). Sediment transfer patterns at the Illgraben catchment, Switzerland: Implications for the time scales of debris flow activities. *Geomorphology*, 125(3):421–432.

Blair, T. C. (1999). Cause of dominance by sheetflood vs. debris-flow processes on two adjoining alluvial fans, Death Valley, California. *Sedimentology*, 46(6):1015–1028.

Blissenbach, E. (1952). Relation of surface angle distribution to particle size distribution on alluvial fans [Arizona]. *Journal of Sedimentary Research*, 22(1):25–28.

Brown, H. E. (2016). *Spatial and temporal analysis of compensational stacking and gradual migration of an experimental debris-flow fan*. MSc thesis, Colorado School of Mines.

Capart, H., Hsu, J. P.-C., Lai, S. Y.-J., and Hsieh, M.-L. (2010). Formation and decay of a tributary-dammed lake, Laonong River, Taiwan. *Water Resources Research*, 46(11):1–23.

Chang, J.-C., Shih, T.-T., Yang, S.-C., Lin, Y.-F., Chen, H.-L., and Tung, T.-H. (1995). A geomorphological study of alluvial fan in Kaopoing Valley and Chaochou Fault Scarp. *Geographical Research*, 24:39–86. (In Chinese).

doi:10.6342/NTU202204140

Chau, K. T., Chan, L., Luk, S., and Wai, W. H. O. (2000). Shape of deposition fan and runout distance of debris flow: Effects of granular and water contents. In *International Conference on Debris Flow Hazards Mitigation*, 387–395.

Chen, T.-Y. K., Hung, C.-Y., Chiang, Y.-C., Hsieh, M.-L., and Capart, H. (2022). A stochastic model of geomorphic risk due to episodic river aggradation and degradation. *Engineering Geology*, 309:106845.

Chen, T.-Y. K., Wu, Y.-C., Hung, C.-Y., Capart, H., and Voller, V. R. (2021). Model codes and data for "A control volume finite element model for predicting the morphology of cohesive-frictional debris flow deposits". Zenodo `https://doi.org/10.5281/zenodo.5933841`.

Coussot, P., Proust, S., and Ancey, C. (1996). Rheological interpretation of deposits of yield stress fluids. *Journal of Non-Newtonian Fluid Mechanics*, 66(1):55–70.

Crowder, D. F. and Sheridan, M. F. (1972). Geologic map of the White Mountain Peak quadrangle, Mono County, California. Geol. Quad. Map GQ-1012, U.S. Geol. Survey.

D'Arcy, M., Roda-Boluda, D. C., and Whittaker, A. C. (2017). Glacial-interglacial climate changes recorded by debris flow fan deposits, Owens Valley, California. *Quaternary Science Reviews*, 169:288–311.

de Haas, T. (2016). *Life, death and revival of debris-flow fans on Earth and Mars: fan dynamics and climatic inferences*. PhD thesis, Utrecht University.

de Haas, T., Braat, L., Leuven, J. R., Lokhorst, I. R., and Kleinhans, M. G. (2015a). Effects of debris flow composition on runout, depositional mechanisms, and deposit morphology in laboratory experiments. *Journal of Geophysical Research: Earth Surface*, 120(9):1949–1972.

doi:10.6342/NTU202204140

de Haas, T., Densmore, A. L., Stoffel, M., Suwa, H., Imaizumi, F., Ballesteros-Cánovas, J., and Wasklewicz, T. (2018). Avulsions and the spatio-temporal evolution of debris-flow fans. *Earth-Science Reviews*, 177:53–75.

de Haas, T., Kleinhans, M. G., Carbonneau, P. E., Rubensdotter, L., and Hauber, E. (2015b). Surface morphology of fans in the high-Arctic periglacial environment of Svalbard: Controls and processes. *Earth-Science Reviews*, 146:163–182.

de Haas, T., van den Berg, W., Braat, L., and Kleinhans, M. G. (2016). Autogenic avulsion, channelization and backfilling dynamics of debris-flow fans. *Sedimentology*, 63(6):1596–1619.

DeGraff, J. V. and Ochiai, H. (2009). Rainfall, debris flows and wildfires. In *Landslides–Disaster Risk Reduction*, 451–471. Springer.

Delorme, P., Devauchelle, O., Barrier, L., and Métivier, F. (2018). Growth and shape of a laboratory alluvial fan. *Physical Review E*, 98:012907.

Denny, C. S. (1965). Alluvial fans in the Death Valley region, California and Nevada. *Geological Survey Professional Paper*, 466:1–62.

Densmore, A. L., de Haas, T., McArdell, B. W., and Schuerch, P. (2019). Making sense of avulsions on debris-flow fans. In *7th International Conference on Debris-Flow Hazards Mitigation: Mechanics, Monitoring, Modeling, and Assessment*.

Deshpande, N. S., Furbish, D. J., Arratia, P. E., and Jerolmack, D. J. (2021). The perpetual fragility of creeping hillslopes. *Nature Communications*, 12(1):1–7.

Detrixhe, M., Gibou, F., and Min, C. (2013). A parallel fast sweeping method for the eikonal equation. *Journal of Computational Physics*, 237:46–55.

Drew, F. (1873). Alluvial and lacustrine deposits and glacial records of the Upper-Indus Basin. *Quarterly Journal of the Geological Society*, 29(1-2):441–471.

doi:10.6342/NTU202204140

Dühnforth, M., Densmore, A. L., Ivy-Ochs, S., Allen, P. A., and Kubik, P. W. (2007). Timing and patterns of debris flow deposition on Shepherd and Symmes creek fans, Owens Valley, California, deduced from cosmogenic 10Be. *Journal of Geophysical Research: Earth Surface*, 112:F03S15.

Edwards, A. N., Russell, A. S., Johnson, C. G., and Gray, J. M. N. T. (2019). Frictional hysteresis and particle deposition in granular free-surface flows. *Journal of Fluid Mechanics*, 875:1058–1095.

Edwards, A. N., Viroulet, S., Kokelaar, B. P., and Gray, J. M. N. T. (2017). Formation of levees, troughs and elevated channels by avalanches on erodible slopes. *Journal of Fluid Mechanics*, 823:278–315.

Engwirda, D. (2014). *Locally optimal Delaunay-refinement and optimisation-based mesh generation*. PhD thesis, University of Sydney.

Engwirda, D. (2020). Inpoly: A fast points-in-polygon test. GitHub, https://github.com/dengwirda/inpoly.

Exner, F. M. (1920). Zur physik der dunen. *Akad. Wiss. Wien Math. Naturwiss. Klasse*, 129(2a):929–952.

Exner, F. M. (1925). Uber die wechselwirkung zwischen wasser und geschiebe in flussen. *Akad. Wiss. Wien Math. Naturwiss. Klasse*, 134(2a):165–204.

Félix, G. and Thomas, N. (2004). Relation between dry granular flow regimes and morphology of deposits: formation of levées in pyroclastic deposits. *Earth and Planetary Science Letters*, 221(1):197–213.

Ghosh, S. K. (2007). *Visibility algorithms in the plane*. Cambridge University Press.

Gilbert, G. K. (1882). *Contributions to the history of Lake Bonneville*. Department of the Interior, US Geological Survey.

doi:10.6342/NTU202204140

Giles, P. T., Whitehouse, B. M., and Karymbalis, E. (2018). Interactions between alluvial fans and axial rivers in Yukon, Canada and Alaska, USA. *Geological Society, London, Special Publications*, 440(1):23–43.

Giudice, H. A., Giammanco, G., Fransos, D., and Preziosi, L. (2019). Modeling sand slides by a mechanics-based degenerate parabolic equation. *Mathematics and Mechanics of Solids*, 24(8):2558–2575.

Gray, J. M. N. T. (2018). Particle segregation in dense granular flows. *Annual review of fluid mechanics*, 50:407–433.

Gregoretti, C., Degetto, M., and Boreggio, M. (2016). Gis-based cell model for simulating debris flow runout on a fan. *Journal of Hydrology*, 534:326–340.

Gómez-Villar, A., Álvarez Martínez, J., and García-Ruiz, J. M. (2006). Factors influencing the presence or absence of tributary-junction fans in the Iberian Range, Spain. *Geomorphology*, 81(3-4):252–264.

Hanselman, D. (2021a). Contour plot for scattered data (https://www.mathworks.com/matlabcentral/fileexchange/38858-contour-plot-for-scattered-data). Retrieved November 30, 2021.

Hanselman, D. (2021b). Linearly interpolate triangulation (https://www.mathworks.com/matlabcentral/fileexchange/38925-linearly-interpolate-triangulation). Retrieved November 30, 2021.

Harvey, A. (2002). The role of base-level change in the dissection of alluvial fans: case studies from southeast Spain and Nevada. *Geomorphology*, 45(1-2):67–87.

Hasbargen, L. E. and Paola, C. (2000). Landscape instability in an experimental drainage basin. *Geology*, 28(12):1067–1070.

Heffernan, P. J. and Mitchell, J. S. (1995). An optimal algorithm for computing visibility in the plane. *SIAM Journal on Computing*, 24(1):184–201.

doi:10.6342/NTU202204140

Herbert, L. (2021). *Controls on Debris Flow Avulsions: White Mountains of California and Nevada*. PhD thesis, Colorado School of Mines.

Hill, K., Khakhar, D., Gilchrist, J., McCarthy, J., and Ottino, J. (1999). Segregation-driven organization in chaotic granular flows. *Proceedings of the National Academy of Sciences*, 96(21):11701–11706.

Hill, K. M., Gioia, G., and Amaravadi, D. (2004). Radial segregation patterns in rotating granular mixtures: waviness selection. *Physical review letters*, 93(22):224301.

Hooke, R. L. (1967). Processes on arid-region alluvial fans. *The Journal of Geology*, 75(4):438–460.

Hooke, R. L. (1968). Steady-state relationships on arid-region alluvial fans in closed basins. *American Journal of Science*, 266(8):609–629.

Hooke, R. L. and Rohrer, W. L. (1977). Relative erodibility of source-area rock types, as determined from second-order variations in alluvial-fan size. *Geological Society of America Bulletin*, 88(8):1177–1182.

Hsieh, M.-L. and Capart, H. (2013). Late Holocene episodic river aggradation along the Lao-nong River (southwestern Taiwan): An application to the Tseng-wen Reservoir Transbasin Diversion Project. *Engineering Geology*, 159:83–97.

Hsieh, M.-L. and Chyi, S.-J. (2010). Late Quaternary mass-wasting records and formation of fan terraces in the Chen-yeo-lan and Lao-nung catchments, central-southern Taiwan. *Quaternary Science Reviews*, 29(11-12):1399–1418.

Hsu, J. P. C. and Capart, H. (2008). Onset and growth of tributary-dammed lakes. *Water Resources Research*, 44:W11201.

Hubert, J. F. and Filipov, A. J. (1989). Debris-flow deposits in alluvial fans on the

doi:10.6342/NTU202204140

west flank of the White Mountains, Owens Valley, California, USA. *Sedimentary Geology*, 61(3-4):177–205.

Iverson, R. M. (1997). The physics of debris flows. *Reviews of geophysics*, 35(3):245–296.

Iverson, R. M. (2015). Scaling and design of landslide and debris-flow experiments. *Geomorphology*, 244:9–20.

Iverson, R. M., Logan, M., LaHusen, R. G., and Berti, M. (2010). The perfect debris flow? aggregated results from 28 large-scale experiments. *Journal of Geophysical Research: Earth Surface*, 115:F03005.

Iverson, R. M., Reid, M. E., Logan, M., LaHusen, R. G., Godt, J. W., and Griswold, J. P. (2011). Positive feedback and momentum growth during debris-flow entrainment of wet bed sediment. *Nature Geoscience*, 4(2):116–121.

Iverson, R. M. and Vallance, J. W. (2001). New views of granular mass flows. *Geology*, 29(2):115–118.

Jackson, L., Kostaschuk, R., and MacDonald, G. M. (1987). Identification of debris flow hazard on alluvial fans in the Canadian Rocky Mountains. *Reviews in Engineering Geology*, 7:115–124.

Jiang, C., Mundilova, K., Rist, F., Wallner, J., and Pottmann, H. (2019). Curve-pleated structures. *ACM Transactions on Graphics*, 38(6):169.

Joe, B. and Simpson, R. B. (1987). Corrections to Lee's visibility polygon algorithm. *BIT Numerical Mathematics*, 27(4):458–473.

Johnson, A. M. (1970). *Physical processes in geology: A method for interpretation of natural phenomena; intrusions in igneous rocks, fractures, and folds, flow of debris and ice*. Freeman, Cooper.

doi:10.6342/NTU202204140

Johnson, C., Kokelaar, B., Iverson, R. M., Logan, M., LaHusen, R., and Gray, J. (2012). Grain-size segregation and levee formation in geophysical mass flows. *Journal of Geophysical Research: Earth Surface*, 117:F01032.

Kaitna, R., Dietrich, W., and Hsu, L. (2014). Surface slopes, velocity profiles and fluid pressure in coarse-grained debris flows saturated with water and mud. *Journal of Fluid Mechanics*, 741:377–403.

Kaitna, R., Palucis, M. C., Yohannes, B., Hill, K. M., and Dietrich, W. E. (2016). Effects of coarse grain size distribution and fine particle content on pore fluid pressure and shear behavior in experimental debris flows. *Journal of Geophysical Research: Earth Surface*, 121(2):415–441.

Kaitna, R., Rickenmann, D., and Schatzmann, M. (2007). Experimental study on rheologic behaviour of debris flow material. *Acta Geotechnica*, 2(2):71–85.

Ke, W.-T. and Capart, H. (2015). Theory for the curvature dependence of delta front progradation. *Geophysical Research Letters*, 42(24):10–680.

Keiler, M., Knight, J., and Harrison, S. (2010). Climate change and geomorphological hazards in the eastern European Alps. *Philosophical Transactions of the Royal Society A: Mathematical, Physical and Engineering Sciences*, 368(1919):2461–2479.

Kepner, J., Kipf, A., Engwirda, D., Vembar, N., Jones, M., Milechin, L., Gadepally, V., Hill, C., Kraska, T., Arcand, W., et al. (2020). Fast mapping onto census blocks. In *2020 IEEE High Performance Extreme Computing Conference (HPEC)*, 1–8. IEEE.

Kevorkian, J. (1990). *Partial Differential Equations: Analytical Solution Techniques*. Brooks/Cole, London.

doi:10.6342/NTU202204140

Kochel, R. C. and Johnson, R. A. (1984). Geomorphology and sedimentology of humid-temperate alluvial fans, central Virginia. *Sedimentology of Gravels and Conglomerates*, 109–122.

Kowalski, J. and McElwaine, J. N. (2013). Shallow two-component gravity-driven flows with vertical variation. *Journal of Fluid Mechanics*, 714:434–462.

Kraal, E. R., Asphaug, E., Moore, J. M., Howard, A., and Bredt, A. (2008). Catalogue of large alluvial fans in martian impact craters. *Icarus*, 194(1):101–110.

Krivoshapko, S. N. and Ivanov, V. N. (2015). *Encyclopedia of Analytical Surfaces*. Springer, Berlin.

Kuster, C. M. and Gremaud, P. A. (2006). Accurately computing the shape of sandpiles. In *Multiscale Optimization Methods and Applications*, 305–312. Springer.

Lai, S. Y. J. and Capart, H. (2007). Two-diffusion description of hyperpycnal deltas. *Journal of Geophysical Research: Earth Surface*, 112:F03005.

Lai, S. Y. J. and Capart, H. (2009). Reservoir infill by hyperpycnal deltas over bedrock. *Geophysical Research Letters*, 36(8):L08402.

Lai, S. Y. J., Gerber, T. P., and Amblas, D. (2016). An experimental approach to submarine canyon evolution. *Geophysical Research Letters*, 43:2741–2747.

Le Hooke, R. B. and Rohrer, W. L. (1979). Geometry of alluvial fans: Effect of discharge and sediment size. *Earth Surface Processes and Landforms*, 4(2):147–166.

Lee, D.-T. (1983). Visibility of a simple polygon. *Computer Vision, Graphics, and Image Processing*, 22(2):207–221.

Lee, D.-T. and Preparata, F. (1984). Euclidean shortest paths in the presence of rectilinear barriers. *Networks*, 14:393–410.

doi:10.6342/NTU202204140

Leenman, A. and Eaton, B. (2021). Mechanisms for avulsion on alluvial fans: Insights from high-frequency topographic data. *Earth Surface Processes and Landforms*, 46(6):1111–1127.

Leenman, A. and Tunnicliffe, J. (2020). Tributary-junction fans as buffers in the sediment cascade: a multi-decadal study. *Earth Surface Processes and Landforms*, 45(2):265–279.

Li, A. L. (2015). Tailings subaerial and subaqueous deposition and beach slope modeling. *Journal of Geotechnical and Geoenvironmental Engineering*, 141(1):04014089.

Lifton, Z. (2013). Owens Valley, CA: Late Pleistocene Slip Rates on the White Mountain Fault. Distributed by OpenTopography. https://doi.org/10.5069/G9FF3Q99.

Lin, Z., Oguchi, T., Chen, Y.-G., and Saito, K. (2009). Constant-slope alluvial fans and source basins in Taiwan. *Geology*, 37(9):787–790.

Liu, K.-F. and Huang, M. C. (2006). Numerical simulation of debris flow with application on hazard area mapping. *Computational Geosciences*, 10(2):221–240.

Liu, K. F. and Mei, C. C. (1989). Slow spreading of a sheet of Bingham fluid on an inclined plane. *Journal of Fluid Mechanics*, 207:505–529.

Lo, C.-M. (2017). Evolution of deep-seated landslide at Putanpunas stream, Taiwan. *Geomatics, Natural Hazards and Risk*, 8(2):1204–1224.

Lo, C.-M., Weng, M.-C., Lin, M.-L., Lee, S.-M., and Lee, K.-C. (2018). Landscape evolution characteristics of large-scale erosion and landslides at the Putanpunas stream, Taiwan. *Geomatics, Natural Hazards and Risk*, 9(1):175–195.

Lobkovsky, A. E., Smith, B. E., Kudrolli, A., Mohrig, D. C., and Rothman, D. H. (2007). Erosive dynamics of channels incised by subsurface water flow. *Journal of Geophysical Research: Earth Surface*, 112:F03S12.

doi:10.6342/NTU202204140

Lorenzo-Trueba, J. and Voller, V. R. (2010). Analytical and numerical solution of a generalized Stefan problem exhibiting two moving boundaries with application to ocean delta formation. *Journal of Mathematical Analysis and Applications*, 366(2):538–549.

Lorenzo-Trueba, J., Voller, V. R., and Paola, C. (2013). A geometric model for the dynamics of a fluvially dominated deltaic system under base-level change. *Computers & Geosciences*, 53:39–47.

Man, T. and Hill, K. (2021). Granular-slurry rheology and asphalt compaction. In *EPJ Web of Conferences*, 249:09010. EDP Sciences.

Man, T., Le, J.-L., Marasteanu, M., and Hill, K. M. (2022). Two-scale discrete element modeling of gyratory compaction of hot asphalt. *Journal of Engineering Mechanics*, 148(2):04021140.

Mangeney, A., Bouchut, F., Thomas, N., Vilotte, J.-P., and Bristeau, M.-O. (2007). Numerical modeling of self-channeling granular flows and of their levee-channel deposits. *Journal of Geophysical Research: Earth Surface*, 112:F02017.

Mangeney, A., Roche, O., Hungr, O., Mangold, N., Faccanoni, G., and Lucas, A. (2010). Erosion and mobility in granular collapse over sloping beds. *J. Geophys. Res.*, 115:F03040.

Marchi, B., PAsuTo, A., and Tecca, P. R. (1993). Flow processes on alluvial fans in the Eastern Italian Alps. *Zeitschrift fur Geomorphologie*, 37:447–458.

Marchi, L. and Tecca, P. (1995). Alluvial fans of the Eastern Italian Alps: morphometry and depositional processes. *Geodinamica Acta*, 8(1):20–27.

McKee, E. H. and Gangloff, R. A. (1969). Stratigraphic distribution of archaeocyathids in the Silver Peak Range and the White and Inyo Mountains, western Nevada and eastern California. *Journal of Paleontology*, 716–726.

doi:10.6342/NTU202204140

Melton, M. A. (1965). Debris-covered hillslopes of the southern Arizona desert: consideration of their stability and sediment contribution. *The Journal of Geology*, 73(5):715–729.

Meng, X. and Wang, Y. (2016). Modelling and numerical simulation of two-phase debris flows. *Acta Geotechnica*, 11(5):1027–1045.

Mitchell, N. C. (2006). Morphologies of knickpoints in submarine canyons. *Geological Society of America Bulletin*, 118(5-6):589–605.

Moore, J. M. and Howard, A. D. (2005). Large alluvial fans on Mars. *Journal of Geophysical Research*, 110(E4):E04005.

Morgan, A. M., Wilson, S. A., and Howard, A. D. (2022). The global distribution and morphologic characteristics of fan-shaped sedimentary landforms on Mars. *Icarus*, 385:115137.

Mullenbach, J. (2018). *Experimental Studies of the Influence of the Properties of the Matrix of a Debris Flow on Its Erosional Behavior*. PhD thesis, University of Minnesota.

Murata, J. (1984). Flow and deformation of fresh concrete. *Matériaux et Constructions*, 17(98):117–129.

Murillo, J. and García-Navarro, P. (2012). Wave Riemann description of friction terms in unsteady shallow flows: Application to water and mud/debris floods. *Journal of Computational Physics*, 231(4):1963–2001.

Ni, W. J. and Capart, H. (2006). Groundwater drainage and recharge by networks of irregular channels. *Journal of Geophysical Research: Earth Surface*, 111(F2):F02014.

O'Brien, J. S. (2006). *2-Dimensional Flood Routine Model Manual, Version 2006.01*. FLO-2D Inc., Nutrioso, AZ, USA.

doi:10.6342/NTU202204140

O'Brien, J. S., Julien, P. Y., and Fullerton, W. (1993). Two-dimensional water flood and mudflow simulation. *Journal of hydraulic engineering*, 119(2):244–261.

Parker, G., Paola, C., Whipple, K. X., and Mohrig, D. (1998). Alluvial fans formed by channelized fluvial and sheet flow. I: Theory. *Journal of Hydraulic Engineering*, 124(10):985–995.

Pauli, N. S. and Gioia, G. (2007). The topography of steady sandpiles on arbitrary domains. *Proceedings of the Royal Society A: Mathematical, Physical and Engineering Sciences*, 463(2081):1247–1258.

Pederson, C. A., Santi, P. M., and Pyles, D. R. (2015). Relating the compensational stacking of debris-flow fans to characteristics of their underlying stratigraphy: Implications for geologic hazard assessment and mitigation. *Geomorphology*, 248:47–56.

Pottmann, H. and Wallner, J. (2001). *Computational Line Geometry*. Springer.

Pudasaini, S. P. (2012). A general two-phase debris flow model. *Journal of Geophysical Research: Earth Surface*, 117:002186.

Pudasaini, S. P. and Fischer, J.-T. (2020). A mechanical model for phase separation in debris flow. *International Journal of Multiphase Flow*, 129:103292.

Pudasaini, S. P. and Hutter, K. (2007). *Avalanche dynamics: dynamics of rapid flows of dense granular avalanches*. Springer.

Rocha, F., Johnson, C., and Gray, J. (2019). Self-channelisation and levee formation in monodisperse granular flows. *Journal of Fluid Mechanics*, 876:591–641.

Roussel, N. (2006). A thixotropy model for fresh fluid concretes: Theory, validation and applications. *Cement and Concrete Research*, 36:1797–1806.

Saito, K. and Oguchi, T. (2005). Slope of alluvial fans in humid regions of Japan, Taiwan and the Philippines. *Geomorphology*, 70(1-2):147–162.

doi:10.6342/NTU202204140

Savage, S. and Iverson, R. (2003). Surge dynamics coupled to pore-pressure evolution in debris flows. In *Proc. 3rd Int. Conf. on Debris-Flow Hazards Mitigation: Mechanics, Prediction, and Assessment*, edited by Rickenmann, D. and Chen, C., 503–514, Millpress, Rotterdam, Netherlands. Citeseer.

Savi, S., Tofelde, S., Wickert, A. D., Bufe, A., Schildgen, T. F., and Strecker, M. R. (2020). Interactions between main channels and tributary alluvial fans: channel adjustments and sediment-signal propagation. *Earth Surface Dynamics*, 8:303––322.

Scheidl, C. and Rickenmann, D. (2010). Empirical prediction of debris-flow mobility and deposition on fans. *Earth Surface Processes and Landforms*, 35(2):157–173.

Scheidl, C., Rickenmann, D., and Chiari, M. (2008). The use of airborne LiDAR data for the analysis of debris flow events in Switzerland. *Natural Hazards and Earth System Sciences*, 8(5):1113–1127.

Staley, D. M., Wasklewicz, T. A., and Blaszczynski, J. S. (2006). Surficial patterns of debris flow deposition on alluvial fans in Death Valley, CA using airborne laser swath mapping data. *Geomorphology*, 74:152–163.

Stock, J. D., Schmidt, K. M., and Miller, D. M. (2008). Controls on alluvial fan long-profiles. *GSA Bulletin*, 120(5-6):619–640.

Stokes, M. and Mather, A. E. (2015). Controls on modern tributary-junction alluvial fan occurrence and morphology: High Atlas Mountains, Morocco. *Geomorphology*, 248:344–362.

Suri, S. and O'Rourke, J. (1986). Worst-case optimal algorithms for constructing visibility polygons with holes. In *Proceedings of the second annual symposium on Computational geometry*, 14–23, ACM Press, New York, USA.

doi:10.6342/NTU202204140

Tai, Y., Heß, J., and Wang, Y. (2019). Modeling two-phase debris flows with grain-fluid separation over rugged topography: Application to the 2009 Hsiaolin event, Taiwan. *Journal of Geophysical Research: Earth Surface*, 124(2):305–333.

Takahashi, T. (1991). *Debris Flow*. IAHR Monograph, Balkema.

Tombarevic, E., Voller, V., and Vušanovic, I. (2013). Detailed CVFEM algorithm for three dimensional advection-diffusion problems. *CMES-Computer Modeling in Engineering & Sciences*, 96(1):1–29.

Tomczyk, A. M. (2021). Morphometry and morphology of fan-shaped landforms in the high-Arctic settings of central Spitsbergen, Svalbard. *Geomorphology*, 392:107899.

Tripathi, A. and Khakhar, D. (2011). Rheology of binary granular mixtures in the dense flow regime. *Physics of Fluids*, 23(11):113302.

Trulsson, M., Andreotti, B., and Claudin, P. (2012). Transition from the viscous to inertial regime in dense suspensions. *Physical review letters*, 109(11):118305.

Tsai, Y.-F. (2006). Three-dimensional topography of debris-flow fan. *Journal of Hydraulic Engineering*, 132(3):307–318.

Tsunetaka, H., Hotta, N., Sakai, Y., and Wasklewicz, T. (2021). The effect of debris-flow sediment grain size distribution on fan forming processes. *Earth Surface Dynamics Discussions*, 1–20.

Tu, Y.-C. (2019). *Trunk river incision of a tributary fan margin: theory, experiment and field observation*. MSc thesis, National Taiwan University.

Valero-Gomez, A., Gomez, J. V., Garrido, S., and Moreno, L. (2013). The path to efficiency: Fast marching method for safer, more efficient mobile robot trajectories. *IEEE Robotics & Automation Magazine*, 20(4):111–120.

doi:10.6342/NTU202204140

van Gerner, H. J., van der Weele, K., van der Meer, D., and van der Hoef, M. A. (2015). Scaling behavior of coarsening Faraday heaps. *Physical Review E*, 92:042203.

Voller, V. (2009). *Basic control volume finite element methods for fluids and solids*, volume 1. World Scientific.

Voller, V. and Paola, C. (2010). Can anomalous diffusion describe depositional fluvial profiles? *Journal of Geophysical Research: Earth Surface*, 115:F00A13.

Whipple, K., Parker, G., Paola, C., and Mohrig, D. (1998). Channel dynamics, sediment transport, and the slope of alluvial fans: Experimental study. *Journal of Geology*, 106:677–693.

Whipple, K. X. and Dunne, T. (1992). The influence of debris-flow rheology on fan morphology, Owens Valley, California. *Geological Society of America Bulletin*, 104(7):887–900.

Williams, R. M., Zimbelman, J. R., and Johnston, A. K. (2006). Aspects of alluvial fan shape indicative of formation process: A case study in southwestern California with application to Mojave Crater fans on Mars. *Geophysical Research Letters*, 33(10):L10201.

Winslow, A. M. (1966). Numerical solution of the quasilinear Poisson equation in a nonuniform triangle mesh. *Journal of Computational Physics*, 1(2):149–172.

Wu, Y.-C. (2020). *Route optimization subject to debris fan risk: field, experiment and modeling study.* MSc thesis, National Taiwan University.

Yang, C.-M., Chao, W.-A., Weng, M.-C., Fu, Y.-Y., Chang, J.-M., and Huang, W.-K. (2022). Outburst debris flow of Yusui stream caused by a large-scale Silabaku landslide, Southern Taiwan. *Landslides*, 19:1807–1811.

doi:10.6342/NTU202204140

Yohannes, B. and Hill, K. M. (2010). Rheology of dense granular mixtures: Particle-size distributions, boundary conditions, and collisional time scales. *Physical Review E*, 82(6):061301.

Yohannes, B., Hsu, L., Dietrich, W., and Hill, K. (2012). Boundary stresses due to impacts from dry granular flows. *Journal of Geophysical Research: Earth Surface*, 117:F02027.

Yuhi, M. and Mei, C. C. (2004). Slow spreading of fluid mud over a conical surface. *Journal of Fluid Mechanics*, 519:337–358.

Zanuttigh, B. and Lamberti, A. (2007). Instability and surge development in debris flows. *Reviews of Geophysics*, 45(3).

Zhao, H. (2007). Parallel implementations of the fast sweeping method. *Journal of Computational Mathematics*, 421–429.

Zhao, M., Salter, G., Voller, V. R., and Li, S. (2019). Can the growth of deltaic shorelines be unstable? *Earth Surface Dynamics*, 7:505–513.

Zubrycky, S., Mitchell, A., McDougall, S., Strouth, A., Clague, J. J., and Menounos, B. (2021). Exploring new methods to analyse spatial impact distributions on debris-flow fans using data from south-western British Columbia. *Earth Surface Processes and Landforms*, 46(12):2395–2413.

doi:10.6342/NTU202204140

Tzu-Yin Kasha Chen

PhD candidate

Dept. of Civil Engineering, National Taiwan University,

Taipei 106, Taiwan

Email: d06521004@ntu.edu.tw

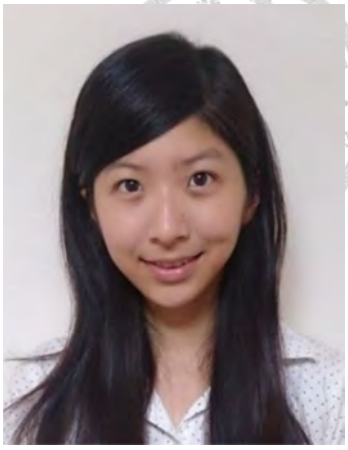

Research interests

Experimental, computational, and field morphology/morphodynamics;

Debris flows, channels, and fans;

Granular flows;

Dam breach hydraulics and flood routing;

Hazards mitigation;

Stochastic modeling;

Infrastructure design policy making.

Education

2021-2022 Visiting Ph.D. candidate, St. Anthony Falls Laboratory, University of Minnesota.

2019-2020 Visiting Ph.D. candidate, St. Anthony Falls Laboratory, University of Minnesota, supported by the Dragon Gate Program of Taiwan's Ministry of Science and Technology.

2017-2022 Ph.D. candidate, Civil Engineering, National Taiwan University, expected graduation in the Spring Semester 2022.

2015-2017 MS student, Civil Engineering, National Taiwan University.

2015-2016 Exchange student, Civil Engineering, Université Catholique de Louvain.

2011-2015 BS student, Civil Engineering, National Taiwan University.

doi:10.6342/NTU202204140